# Ascending neurons convey behavioral state to integrative sensory and action selection centers in the brain

Chin-Lin Chen<sup>1</sup>, Florian Aymanns<sup>1</sup>, Ryo Minegishi<sup>2</sup>, Victor D. V. Matsuda<sup>1</sup>, Nicolas Talabot<sup>1,3</sup>, Semih Günel<sup>1,3</sup>, Barry J. Dickson<sup>2</sup>, and Pavan Ramdya<sup>\*1</sup>

<sup>1</sup>Neuroengineering Laboratory, Brain Mind Institute & Interfaculty Institute of Bioengineering, EPFL, Lausanne, Switzerland

<sup>2</sup>Janelia Research Campus, Howard Hughes Medical Institute, Ashburn, VA, USA <sup>3</sup>Computer Vision Laboratory, EPFL, Lausanne, Switzerland

#### Abstract

Knowledge of one's own behavioral state—whether one is walking, grooming, or resting—is critical for contextualizing sensory cues including interpreting visual motion and tracking odor sources. Additionally, awareness of one's own posture is important to avoid initiating destabilizing or physically impossible actions. Ascending neurons (ANs), interneurons in the vertebrate spinal 5 cord or insect ventral nerve cord (VNC) that project to the brain, may provide such high-fidelity 6 behavioral state signals. However, little is known about what ANs encode and where they convey 7 signals in any brain. To address this gap, we performed a large-scale functional screen of AN 8 movement encoding, brain targeting, and motor system patterning in the adult fly, Drosophila melanogaster. Using a new library of AN sparse driver lines, we measured the functional properties of 247 genetically-identifiable ANs by performing two-photon microscopy recordings of neural activity in tethered, behaving flies. Quantitative, deep network-based neural and behavioral analyses revealed that ANs nearly exclusively encode high-level behaviors—primarily walking as well as resting and grooming—rather than low-level joint or limb movements. ANs that convey selfmotion—resting, walking, and responses to gust-like puff stimuli—project to the brain's anterior ventrolateral protocerebrum (AVLP), a multimodal, integrative sensory hub, while those that encode discrete actions—eye grooming, turning, and proboscis extension—project to the brain's gnathal ganglion (GNG), a locus for action selection. The structure and polarity of AN projections within the VNC are predictive of their functional encoding and imply that ANs participate in motor computations while also relaying state signals to the brain. Illustrative of this are ANs that temporally integrate proboscis extensions over tens-of-seconds, likely through recurrent interconnectivity. Thus, in line with long-held theoretical predictions, ascending populations convey high-level behavioral state signals almost exclusively to brain regions implicated in sensory feature contextualization and action selection.

#### 1 Introduction 25

2

3

9

10

11

12

13

14

15

16

17

18

19

20

21

22

23

24

To generate adaptive behaviors, animals [1] and robots [2] must not only sense their environment but 26 also be aware of their own behavioral state including low-level movements of their limbs and high-27 level behaviors such as walking and resting. This self-awareness has long been theorized to overcome 28 at least two major challenges for robust, autonomous control. First, knowing if one is at rest or in 29 motion permits the accurate interpretation of whether sensory cues, like visual motion during feature 30 tracking or odor intensity fluctuations during plume following, result from exafference (the movement 31 of objects in the world), or reafference (self-motion with respect to stationary objects) [1]. Second, 32 being aware of one's current posture enables the selection of appropriate future actions that are not 33 destabilizing, or physically impossible. 34

In line with these theoretical predictions, neural representations of behaviors have been observed 35 widely across the brains of mice [3-5], and in the fly, *Drosophila melanogaster* [6-9]. Furthermore, 36

<sup>\*</sup>corresponding author: pavan.ramdya@epfl.ch

<sup>37</sup> studies in *Drosophila* have supported roles for behavioral state signals in sensory contextualization <sup>38</sup> (flight [6] and walking [7] modulate neurons in the visual system [8, 10]), and action selection (an <sup>39</sup> animal's walking speed regulates its decision to run or freeze in response to a fear-inducing stimu-<sup>40</sup> lus [11]).

Despite these advances, the cellular origins of behavioral state signals in the brain remain largely 41 unknown. On one hand, they might arise from efference copies generated by descending neurons 42 (DNs) in the brain that project to and drive downstream motor systems [1]. However, these efference 43 copies would not be expected to provide the most precise readout of one's own behavioral state: the 44 brain's descending commands will be sculpted by musculoskeletal interactions with the environment. 45 Instead, a more categorically and temporally precise readout of ongoing behaviors might be obtained 46 from ascending neurons in the motor system that process proprioceptive and tactile signals and then 47 convey a holistic representation of behavioral states to the brain. Although these behavioral signals 48 may come from a subset of primary mechanosensory neurons in the limbs [12], they are more likely 49 to be computed and conveyed by second- and higher-order ascending neurons (ANs) residing in the 50 spinal cord of vertebrates [13–16], or insect ventral nerve cord (VNC) [17, 18]. In Drosophila, ANs 51 have been shown to process limb proprioceptive and tactile signals, likely sculpting a more complex 52 and ethologically-salient readout of ongoing movements [12, 19, 20]. 53

To date only a few genetically-identifiable AN cell types have been studied in behaving animals— 54 primarily in the fly, Drosophila melanogaster, which has a relatively small number of neurons that 55 can also be genetically targeted for repeated investigation. These studies support the hypothesis that 56 ANs are a prominent source of behavioral state signals in the brain. First, microscopy recordings of 57 AN terminals in the brain have shown that Lco2N1 and Les2N1D ANs are active during walking [21], 58 and that LAL-PS-ANs convey walking signals to the visual system [22]. Second, artificial activation 59 of pairs of PER<sub>in</sub> ANs [23], and Moonwalker ANs [24] regulates action selection and behavioral 60 persistence, respectively. 61

These first insights urgently motivate the investigation of three fundamental questions via a more 62 comprehensive and quantitative analysis of large AN populations. First, what information do ANs 63 convey to the brain (Figure S1A)? They might encode low-level movements of the joints or limbs, or 64 high-level behavioral states like whether an animal is walking, or grooming (Figure 1A-i). Second, 65 where do ANs convey this information to in the brain (Figure S1B)? They might project widely 66 across brain regions, or narrowly target circuit hubs with specific functions (Figure 1A-ii). Third, 67 what can an AN's patterning within the VNC tell us about its encoding and computational role (Fig-68 **ure 1A-iii**)? Answering these three questions would open the door to a cellular-level understanding 69 of how neurons encode behavioral states by integrating proprioceptive, tactile, and other sensory 70 feedback signals. It would also enable the study of how behavioral state signals are incorporated by 71 brain circuits to intelligently contextualize multimodal cues and to select appropriate future actions. 72 To address these questions, we developed and used a number of advanced experimental and 73 analytical tools. First, we screened a library of split-Gal4 Drosophila driver lines (R.M. and B.J.D., 74 unpublished). These, along with the published MAN-spGal4 [24] and 12 sparsely expressing Gal4 75 lines [25], collectively allowed us to gain repeated genetic access to 247 ANs (Figure 1B; Table 1). 76 Using these driver lines and a multi-color flip-out (MCFO) approach [26], we then quantified the 77 projections of ANs within the brain and VNC (Figure 1C). Second, we screened the encoding 78 of these ANs through two-photon microscopy functional recordings of neural activity within the 79 VNC of tethered, behaving flies [27]. To overcome noise and movement-related deformations in 80 imaging data, we developed and used 'AxoID', a deep learning-based software to semi-automatically 81 identify and track axonal Regions-of-Interest (ROIs)(see Methods). Third, to precisely quantify joint 82 angles and limb kinematics, we used a multicamera array to record behavior during two-photon 83 imaging. We processed resulting videos using DeepFly3D, a deep learning-based 3D pose estimation 84 software [28]. By combining these 3D joint positions with measured spherical treadmill rotations, 85 a proxy for locomotor velocities [29], we could then segment and classify behavioral time-series and 86 study the relationship between behavioral states and ongoing neural activity using linear models. 87

These analyses uncovered a number of fundamental characteristics of ANs. First, as a population, ANs do not project broadly across the brain but principally target two hubs: (i) the anterior ventrolateral protocerebrum (AVLP), a site for higher-order multimodal convergence—vision [30], olfaction [31], audition [32–34], and taste [35]—, and (ii) the gnathal ganglion (GNG), a region important for action selection [23, 36, 37]. Second, ANs encode high-level behavioral states, primarily walking, rather than low-level joint or limb movements. Third, distinct behavioral state signals are system-

atically conveyed to different brain targets. The AVLP is informed of self-motion states like resting,

<sup>95</sup> walking, and the presence of gust-like stimuli, likely to contextualize sensory cues. By contrast, the

<sup>96</sup> GNG receives precise signals about actions—turning, eye grooming, and proboscis extension—likely
 <sup>97</sup> to guide action selection.

To understand the relationship between AN behavioral state encoding and brain projection pat-98 terns, we then performed a more in-depth investigation of seven AN classes. We observed a correspon-99 dence between the morphology of ANs in the VNC and their behavioral state encoding: ANs with 100 neurites targeting all three VNC neuromeres (T1-T3) encode global locomotor states (e.g., resting 101 and walking) while those with projections only to the T1 prothoracic neuromere encoded foreleg-102 dependent behaviors (e.g., eve grooming). Notably, AN axons were also present within the VNC. 103 This suggests that ANs are not simply passive relays of behavioral state signals to the brain but 104 that they may also help to orchestrate motor actions and/or compute state encodings. This latter 105 possibility is illustrated by a class of 'PE-ANs' that seems to encode the number of proboscis exten-106 sions generated over tens of seconds, possibly through recurrent interconnectivity within the VNC. 107 In summary, these data provide a first comprehensive view of ascending signals to the brain, opening 108 the door for a cellular-level understanding of how behavioral states are computed, and how ascending 109 motor signals enable the brain to contextualize sensory signals and select appropriate future actions. 110

# **111 2 Results**

# <sup>112</sup> 2.1 A large-scale screen of ascending neuron movement encoding, brain <sup>113</sup> targeting, and motor system patterning

We performed a functional screen of 108 driver lines that target small sets of ANs (Figure 1B) 114 to address to what extent they encode low-level joint and limb movements, or high-level behavioral 115 states. To quantify limb movements, we recorded each fly using six synchronized cameras (a sev-116 enth camera was used to position the fly on the ball) (Figure 1D). We processed these videos 117 using DeepFly3D [28], a markerless 3D pose estimation software that outputs joint positions and 118 angles (Figure 1E). We also measured spherical treadmill rotations using two optic flow sensors [29] 119 and converted these into three fly-centric velocities: forward (mm/s), sideways (mm/s), and yaw 120 (degree/s) (Figure 1F) that correspond to forward/backward walking, side-slip, and turning, re-121 spectively. A separate DeepLabCut [38] deep neural network was used to track proboscis extensions 122 (PEs) from one camera view (Figure S2). We used a puff of  $CO_2$  to elicit behavior in sedentary 123 animals. 124

Synchronized with movement quantification, we recorded the activity of ANs by performing two-125 photon imaging of the cervical connective within the thoracic ventral nerve cord (VNC) [27]. The 126 VNC houses motor circuits that are functionally equivalent to those in the vertebrate spinal cord (Fig-127 ure 1G, left). Neural activity was read-out as changes in the fluorescence of a genetically-encoded 128 calcium indicator, OpGCaMP6f, expressed in a small number of ANs. Simultaneously, we recorded 129 tdTomato fluorescence as an anatomical fiduciary. Imaging coronal (x-z) sections of the cervical con-130 nective allowed us to keep AN axons within the imaging field-of-view despite behaviorally-induced 131 motion artifacts that would disrupt conventional horizontal (x-y) section imaging [27]. Sparse sp-132 Gal4 and Gal4 fluorescent reporter expression facilitated axonal region-of-interest (ROI) detection. 133 To semi-automatically segment and track AN ROIs across thousands of imaging frames, we devel-134 oped and used AxoID, a deep network-based software (Figure 1G, right) (see Methods). AxoID 135 also helped perform ROI detection despite significant movement-related ROI translations and defor-136 mations as well as, for some driver lines, relatively low transgene expression levels and suboptimal 137 imaging signal-to-noise ratios (SNR). 138

To relate AN neural activity with ongoing limb movements, we trained classifiers using 3D joint angles and spherical treadmill rotational velocities to accurately and automatically detect nine behaviors—forward and backward walking, spherical treadmill pushing, resting, eye and antennal grooming, foreleg and hindleg rubbing, and abdominal grooming (Figure 1H). Additionally, we classified non-orthogonal, co-occurring behaviors like proboscis extensions (PEs) and recorded the timing of CO<sub>2</sub> puff stimuli (Video 1).

Our final dataset consisted of neural activity recordings from 247 ANs targeted using 70 sparselylabelled driver lines (more than 32 h of data). These data included (i) anatomical projection patterns,

and temporally synchronized (ii) neural activity, (iii) joint angles, and (iv) spherical treadmill rotations. Here we focus on the results for 157 of the most active ANs taken from 50 driver lines (more than 23 h of data) (Video 2). The remainder were excluded due to redundancy with other driver lines, a lack of neural activity, or a low SNR (as determined by smFP confocal imaging, or two-photon imaging of tdTomato and OpGCaMP6f). Representative data from each of these selected driver lines illustrate the richness of our dataset (Videos 3-52).

#### <sup>153</sup> 2.2 Ascending neurons encode high-level behaviors

With these data, we first asked to what extent AN activity encode low-level joint angles and leg 154 movements, or high-level behaviors like walking, resting, and grooming (Figure S1A). We expected 155 that, unlike primary limb mechanosensory neurons, second- and higher-order ANs would more likely 156 integrate and process proprioceptive and tactile sensory signals to encode high-level behavioral states. 157 This remained unknown because previous studies of AN encoding [21-23] did not quantify movements 158 at high enough resolution, or study more than a few ANs in total. To address this gap, with the 159 data from our large-scale functional screen, we performed a linear regression analysis to quantify 160 the degree to which the movements of individual joints, legs, pairs of legs, or epochs of high-level 161 behaviors could explain the time-course of AN activity. Specifically, we quantified the unique ex-162 plained variance (UEV, or  $\Delta R^2$ ) for each movement, or behavioral regressor via cross-validation by 163 subtracting a reduced model  $R^2$  from the full model  $R^2$ . In the reduced model, a regressor of interest 164 was shuffled while keeping the other regressors intact (see Methods). To compensate for the temporal 165 mismatch between fast leg movements and slower calcium signal decay dynamics, every joint angle 166 and behavioral state regressor was convolved with a decay kernel chosen to maximize the explained 167 variance in neural activity. 168

First we examined to what extent individual joint angles could explain the activities of 157 ANs. 169 We confirmed that the vast majority of joint angles do not covary with others—with the exception 170 of the middle and hindleg CTr and FTi pitch angles which were highly correlated to one another 171 (Figure S3). This is important because if two regressors are highly correlated, one regressor can 172 compensate when shuffling the other, resulting in a false negative outcome. We did not find any 173 evidence of joint angles explaining AN activity (Figure 2A). Similarly, individual leg movements 174 (tested by shuffling all of the joint angle regressors for a given leg) could not explain the variance of 175 AN activity (Figure 2B). Additionally, with the exception of ANs from SS25469 whose activities 176 could be explained by movements of the forelegs (Figure 2C), AN activity largely could not be 177 explained by the movements of pairs of legs. By contrast, the activity of ANs could be explained 178 by high-level behavioral states (Figure 2D). Most ANs encoded self-motion—forward walking and 179 resting—but some also encoded specific actions like eye grooming, proboscis extensions, as well as 180 responses to puff stimuli. 181

<sup>182</sup> Our regression approach is conservative and avoids false positives. However, because is prone to <sup>183</sup> false negatives for infrequently occurring behaviors like abdominal grooming and hindleg rubbing, as <sup>184</sup> an additional alternative approach, we measured the mean normalized  $\Delta F/F$  for each AN for each <sup>185</sup> high-level behavioral state. Using this complementary approach, we could confirm and extend our <sup>186</sup> results (Figure S4). We considered results from both our linear regression and mean normalized <sup>187</sup>  $\Delta F/F$  analyses when selecting neurons for further in-depth analyses.

# Ascending neurons target integrative sensory, or action selection brain regions as a function of their encoding

Having identified high-level behavioral state encoding for a large population of ANs, we next won-190 dered to what extent these distinct state signals are routed to specific and distinct brain targets 191 (Figure S1B). On one hand, individual ANs might project diffusely to multiple brain regions. Al-192 ternatively, they might target one, or only a few regions. For instance, locomotor signals carried by 193 walking and resting encoding ANs might be conveyed to brain regions to contextualize time-varying 194 visual and olfactory cues with respect to an animal's own self-motion. On the other hand, ANs that 195 signal when an animal is grooming might target action selection brain regions to prohibit future ac-196 tions that might result in unstable postures. To address these possibilities, we quantified the brain 197 projections of all 157 ANs by staining and imaging the expression of spFP and MCFO reporters in 198 these neurons (Figure 1C). 199

Strikingly, we found that AN projections to the brain were largely restricted to two regions: the 200 AVLP, a site known for multimodal, integrative sensory processing [30–35] and the GNG, a hub for 201 action selection [23,36,37] (Figure 3A). ANs encoding resting and puff-responses almost exclusively 202 target the AVLP (Figure S5A,B) providing a robust means for interpreting whether sensory cues 203 arise from self-motion or the movement of objects in the external environment: while resting, an 204 animal can perceive visual motion due to moving objects, and odor fluctuations due to gust-like puffs 205 of air. By contrast, the GNG is targeted by ANs encoding a wide variety of behavioral states including 206 walking, eye grooming, and proboscis extensions (Figure S5A,B). These signals may ensure that 201 future actions are compatible with ongoing ones. 208

Because AN dendrites and axons within the VNC might help to compute behavioral state signals, 209 we next asked to what extent their projection patterns within the VNC are predictive of an AN's 210 encoding. For example, ANs encoding resting might require sampling each VNC leg neuromere (T1, 211 T2, and T3) to confirm that all legs are inactive. By quantifying AN projections within the VNC 212 (Figure 3B), we found that, indeed, an AN's VNC projection pattern can be predictive of behavioral 213 state encoding. As hypothesized, ANs encoding resting (e.g., SS27485) all project to every VNC leg 214 neuromere (Figure S5A,C). By contrast, ANs encoding foreleg-dependent eye grooming (SS25469) 215 only project within T1, the VNC neuromere that houses motor circuits that control the front legs 216 (Figure S5A,C). Next, to more precisely investigate how the morphological features of ANs relate to 217 behavioral state encoding, we performed a more detailed study of a diverse subset of ANs that encode 218 resting, puff-responses, walking, turning, foreleg-dependent behaviors, eve grooming, and proboscis 219 extensions. 220

#### <sup>221</sup> 2.4 Distinct rest- and puff-encoding by morphologically similar ANs

AN classes that encode resting and puff responses had coarsely similar projection patterns: both almost exclusively target the brain's AVLP while also both sampling from all three VNC leg neuromeres (T1-T3) (Figure S5). We therefore next investigated which more detailed morphological features might be predictive of their very divergent encoding.

We addressed this question by closely examining the functional and morphological properties of 226 specific pairs of 'rest-ANs' (SS27485) and 'puff-ANs' (SS36112). Neural activity traces of rest-ANs 227 and puff-ANs could be reliably predicted by regressors for resting (Figure 4A), and puff-stimuli 228 (Figure 5A), respectively. This was statistically confirmed by comparing behavior-triggered averages 229 of AN responses at the onset of resting (Figure 4B), or puff stimulation (Figure 5B), respectively. 230 Importantly, although  $CO_2$  puffs frequently elicited brief periods of backward walking, close analysis 23 revealed that puff-ANs primarily respond to gust-like puffs and do not encode backward walking 232 (Figure S6). They also did not encode responses to  $CO_2$  specifically: the same neurons responded 233 equally well to air puffs (Figure S7). 234

As mentioned, rest- and puff-ANs, despite their very distinct encoding, exhibit similar innervation 235 patterns in the brain and VNC. However, MCFO-based single neuron analysis revealed a few subtle 236 but important differences. First, rest- and puff-AN cell bodies are located in the T2 (Figure 4C) 237 and T3 (Figure 5C) neuromeres, respectively. Second, although both AN classes project medially 238 into all three leg neuromeres (T1-T3), rest-ANs have a simpler morphology (Figure 4D) compared 239 with the more complex arborization of puff-ANs in the VNC (Figure 5D). In the brain, both AN 240 types project to nearly the same ventral region of the AVLP. There, they exhibit varicose terminals 241 (Figure 4E and Figure 5E). Using syt:GFP, a GFP tagged synaptotagmin (presynaptic) marker, 242 we confirmed that these varicosities house synaptic terminals (Figure 4F, top and Figure 5F, 243 top). Notably, in addition to smooth, likely dendritic arbors, both AN classes have axon terminals 244 within the VNC (Figure 4F, bottom and Figure 5F, bottom). 245

Taken together, these results demonstrate that even very subtle differences in VNC patterning can give rise to dramatically different AN tuning properties. In the case of rest- and puff-ANs, we speculate that this might be due to physically close, but distinct presynaptic partners—possibly leg proprioceptive afferents for rest-ANs, and leg tactile afferents for puff-ANs.

### <sup>250</sup> 2.5 Walk- or turn- encoding depends on the laterality of VNC projections

Among the ANs we analyzed, most encoded walking (Figure 2D). However, this broad category of locomotion includes more subtle dimensions including walking direction and turning. We reasoned

that an AN's patterning within the VNC may be predictive of whether it encodes locomotion broadly (e.g., walking) versus narrowly (e.g., turning).

Indeed, we observed that while the activity of one pair of ANs (SS29579, 'walk-ANs') was re-255 markably well explained by the timing and onset of walking epochs (Figure 6A-C), for other ANs 256 a broad walking regressor could account for much less variance in neural activity (Figure 2D). We 257 reasoned that these ANs might instead encode narrower locomotor features like turning. For ex-258 ample, for a bilateral pair of DNa01 descending neurons, their difference in activity correlates with 259 turn direction [27, 39]. To see if this might also be the case for some pairs of walk-encoding ANs, we 260 quantified the degree to which their difference in activity can be explained by spherical treadmill roll 261 and vaw velocities—a proxy for turning behaviors (Figure 7A). Indeed, we found one pair of ANs 262 (SS51046) for which turning explained a relatively large amount of variance. For this pair of 'turn-263 ANs', although a combination of forward and backward walking regressors poorly predicted neural 264 activity (Figure 7B), a regressor based on spherical treadmill roll velocities strongly predicted the 265 difference in activity between this bilateral pair of neurons (Figure 7C). When an animal turned 266 right, the right (ipsilateral) turn-AN was active. Conversely, the left turn-AN was active during left 267 turns (Figure 7D). During forward walking, both turn-ANs were active (Figure 7E). 268

We next asked how VNC patterning might predict this distinction between broad (walk-AN) 269 versus narrow (turn-AN) locomotor encoding. Both AN classes have cell bodies in the VNC's T2 270 neuromere (Figure 6D and Figure 7F). However, walk-ANs bilaterally innervate the T2 neuromere 271 (Figure 6E), whereas turn-ANs unilaterally innervate T1 and T2 (Figure 7G, black). Their 272 ipsilateral T2 projections are smooth and likely dendritic (Figure  $7H_1, I_1$ ), while their contralateral 273 T1 projections are varicose and exhibit syt:GFP puncta, suggesting that they harbor presynaptic 274 terminals (Figure 7H<sub>2</sub>,I<sub>2</sub>). Both walk-ANs (Figure 6D,E) and turn-ANs (Figure 7F,G) project 275 to the brain's GNG. However, only turn-ANs project to the WED (Figure 7H,I). Notably, walk-AN 276 terminals in the brain (Figure 6F) are not labelled by syt:GFP (Figure 6G), suggesting that they 277 may be neuromodulatory in nature and rely on another class of synaptic machinery [40]. 278

These data support the notion that broad versus narrow behavioral state encoding of ANs may arise from the laterality of VNC patterning. Additionally, we observed that pairs of broadly-tuned walk-ANs that bilaterally innervate the VNC are synchronously active. By contrast, pairs of narrowlytuned turn-ANs are asynchronously active. This correlation between the laterality of an AN pair's VNC projections and their synchrony seems to be a general principle (Figure S8).

## <sup>284</sup> 2.6 Foreleg-dependent actions are encoded by ANs in the anterior VNC

In addition to locomotion, flies use their forelegs to perform complex movements including reaching, boxing, courtship tapping, and several kinds of grooming—eye grooming, antennal grooming, and foreleg rubbing. An ongoing awareness of these behavioral states is critical to select appropriate future actions that do not lead to instability. For example, before deciding to groom its hindlegs, an animal must first confirm that its forelegs are stably on the ground and not also grooming.

We noted that some ANs project only to the VNC's anterior-most, T1 leg neuromere (Fig-290 **ure S5C**). This pattern implied a potential role in encoding actions that only depend on the forelegs. 291 Indeed, close examination revealed two classes of ANs that encode foreleg-related behaviors. We found 292 ANs (SS42740) that were broadly active during multiple foreleg-dependent behaviors including walk-293 ing, pushing, and grooming ('foreleg-ANs'; overlaps with R70H06) (Figure S4)(Figure 8A,B). By 294 contrast, another pair of ANs (SS25469) were narrowly and sometimes asynchronously active only 295 during eye grooming ('eye groom-ANs') (Figure S4) (Figure 9A,B). Similar to walking and turn-296 ing, we hypothesized that this broad (foreleg) versus narrow (eye groom) behavioral encoding might 297 be reflected by a difference in the promiscuity and laterality of AN innervations in the VNC. 298

To test this hypothesis, we compared the morphologies of foreleg- and eye groom-ANs. Both had 299 cell bodies in the T1 neuromere, although foreleg-ANs were posterior (Figure 8C) and eye groom-300 ANs were anterior (Figure 9C). Foreleg- and eye groom-ANs also both projected to the dorsal T1 301 neuromere with eye groom-AN neurites restricted to the tectulum (Figure 8D and Figure 9D). No-302 tably, foreleg-AN puncta (Figure 8E, bottom) and syt:GFP (Figure 8F, bottom) were bilateral 303 and diffuse while eve groom-AN puncta (Figure 9E, bottom) and syt:GFP (Figure 9F, bottom) 304 were largely restricted to the contralateral T1 neuromere. Projections to the brain paralleled this dif-305 ference in VNC projection promiscuity: foreleg-ANs terminated across multiple brain areas—GNG, 306 AVLP, SAD, VES, IPS, and SPS (Figure 8E,F top)— while eye groom-ANs narrowly targeted the 307

#### GNG (Figure 9E,F top).

These results further illustrate that AN encoding can be predicted by VNC patterning. Here, diffuse, bilateral projections are associated with encoding multiple behaviors that require foreleg movements whereas focal, unilateral projections give rise to a narrow encoding of eye grooming.

# <sup>312</sup> 2.7 Temporal integration of proboscis extensions by a cluster of ANs

Flies often generate spontaneous proboscis extensions (PEs) while resting (Figure 10A, yellow ticks). We observed that 'PE-ANs' (SS31232, overlap with SS30303) (Figure 2D) become active during PE trains—a sequence of PEs that occur within a short period of time (Figure 10A). Close examination revealed that PE-AN activity slowly ramped up over the course of PE trains. This made them difficult to model using a simple PE regressor: their activity levels were lower than predicted early in PE trains, and higher than predicted late in PE trains. On average, across many PE trains, PE-AN activity reached a plateau by the seventh PE (Figure 10B).

Thus, PE-AN activity seemed to convey the temporal integration or counting of discrete events [41, 42]. Therefore, we next asked if PE-AN activity might be better predicted using a PE regressor that integrates the number of PEs within a given time window. Remarkably, by testing a variety of window sizes, we determined that the most accurate prediction of PE-AN dynamics could be obtained with an integration window of more than 10 s (Figure 10C, red circles). This additional integration window made it possible to predict both the undershoot and overshoot of PE-AN activity at the start and end of PE trains, respectively (Figure 10D).

Temporal integration can be implemented using a line attractor model [43, 44] based on recurrently 327 connected circuits. To explore the degree to which PE-AN might support an integration of PE events 328 through recurrent interconnectivity, we examined PE-AN morphologies more closely. PE-AN cell 329 bodies were located in the anterior T1 neuromere (Figure 10E). From there they projected dense 330 neurites into the midline of the T1 neuromere (Figure 10F). Among these neurites, we observed 331 puncta and syt:GFP expression consistent with presynaptic terminals (Figure 10G,H, bottom). 332 Their dense and highly overlapping arbors would be consistent with a mutual interconnectivity be-333 tween PE-ANs. These putatively recurrent connections might enable the integration of PE events 334 over tens-of-seconds. This integration might filter out sparse PE events associated with feeding and 335 allow PE-ANs to only signal long PE trains that might be observed during deep rest-states [45]. 336 These signals are conveyed to the brain's GNG (Figure 10G, H, top). 337

# 338 3 Discussion

Animals must be aware of their own behavioral states to accurately interpret sensory cues and select 339 appropriate future actions. Here, we examined how this self-awareness might be conveyed to the brain 340 by studying the activity and targeting of ascending neurons within the *Drosophila* motor system. 341 Specifically, we addressed a number of fundamental questions (Figure 1A). First, to what extent do 342 ANs encode the low-level movements of joint and legs, or high-level behavioral states like walking and 343 grooming? Second, are individual AN encodings narrow (conveying one movement or behavior), or 344 broad (conveying multiple movements or behaviors)? Third, to what extent do ANs target multiple or 345 single brain regions? Fourth, do ANs that convey distinct signals also target distinct brain regions? 346 Fifth, which characteristics of an AN's patterning in the VNC are predictive of their encoding? 347 Sixth, are ANs a simple feedforward relay of signals to the brain, or might they also contribute to 348 computations within the VNC? To address these questions, we performed a large-scale functional and 349 anatomical screen by leveraging a library of *Drosophila* sparsely expressing driver lines that target 350 small sets of ANs as well as new experimental and computational tools for recording and quantifying 351 neural activity in behaving animals. 352

#### 353 3.1 Encoding of high-level behavioral states

We discovered that ANs functionally encode high-level behavioral states (Figure 11A), predominantly those related to self-motion like walking and resting. These encodings could be further distinguished as either broad (e.g., walk-ANs and foreleg-ANs), or narrow (e.g., turn-ANs and eye groom-ANs). Similarly, neurons in the vertebrate dorsal spinocerebellar tract have been shown to be

more responsive to whole limb versus individual joint movements [46]. To compensate for the techni-358 cal hurdle of relating relatively rapid joint movements to slow calcium indicator kinetics, we convolved 359 joint angle time-series' with a decay kernel that would maximize the explanatory power of our re-360 gression analyses. Additionally, we confirmed that potential issues related to the non-orthogonality 361 of joint angles and leg movements would not obscure our ability to explain the variance of AN neural 362 activity (Figure S3). Our observation that eye groom-AN activity could be explained by movements 363 of the forelegs gave us further confidence that, in principle, leg movement encoding could be detected 364 (Figure 2C). Nevertheless, to further confirm the absence of low-level joint and leg movement en-365 coding, future work could directly manipulate the joints and legs of restricted animals while recording 366 AN activity [47]. Finally, we sometimes observed that the activity of putative walk-encoding ANs 367 was not fully explained by our walking regressor, nor our turn analysis, (e.g., SS44270, overlaps with 368 SS41605). This suggests that some ANs may encode other features of locomotion. 369

# <sup>370</sup> 3.2 Predominant projection to the brain's AVLP and GNG

We found that the vast majority of ANs do not project diffusely across the brain but rather specifically 371 target either the AVLP and GNG (Figure 11B). We hypothesize that this may reflect the roles of 372 behavioral state signals in two fundamental brain computations. First, the AVLP is a known site for 373 multimodal, integrative sensory convergence [30–35]. Thus, the projection of ANs encoding resting, 374 walking, and gust-like puffs to the AVLP (Figure 11C) may serve to contextualize time-varying 375 visual and olfactory signals to indicate if they arise from self-motion, or from objects and odors 376 moving in the world. A similar role of conveying self-motion has been proposed for neurons in the 377 vertebrate dorsal spinocerebellar tract [16]. Second, the GNG is thought to be an action selection 378 center [23, 36, 37]. Thus, the projection of ANs encoding diverse behaviors—walking, turning, foreleg 379 movements, eye-grooming, and proboscis extensions (Figure 11D,E)—to the GNG may serve to 380 indicate whether potential future actions are compatible with ongoing behaviors. This role would 381 be consistent with hierarchical control approaches proposed in robotics [2]. Notably, walk-ANs that 382 project to the ventral GNG may be neuromodulatory in nature. Thus, they may be well-poised to 383 rapidly shift an animal's internal state and the relative values of potential future actions. 384

Notably, the GNG is also heavily innervated by descending neurons (DNs). Because ANs and 385 DNs both contribute to action selection [23, 24, 37, 48], we speculate that they may connect within the 386 GNG to form a feedback loop between the brain and motor system. Specifically, ANs that encode 387 specific actions might excite DNs that drive the same actions, to generate behavioral persistence, 388 and also suppress DNs that drive conflicting actions. For example, turn-ANs may excite DNa01 and 389 DNa02 which control turning [27, 39, 49], and foreleg-ANs may excite aDN1 and aDN2 that control 390 grooming [50]. Of course the opposite might also be true: ANs might *inhibit* DNs that encode the 301 same action to ensure that motor actions are terminated once they have been performed. These 392 competing hypotheses may soon be tested using emerging connectomics datasets [51]. 393

# <sup>394</sup> 3.3 Patterning within the VNC is predictive of behavioral encoding

The morphology of an AN's neurites in the VNC are, to a remarkable degree, predictive of encoding 395 (Figure 11C-E). We illustrate this in a few ways. First, ANs innervating all three leg neuromeres 396 (T1, T2, and T3) encode global self-motion—walking, resting, and gust-like puffs. By contrast, those 397 with more restricted projections to one neuromere (T1 or T2) encode discrete actions—turning, eve 398 grooming, foreleg movements, and PEs. This might reflect the cost of neural wiring, a constraint that 399 may encourage a neuron to sample the minimal sensory and motor information required to compute 400 a particular behavioral state. Second, broadly tuned ANs (walking and foreleg-dependent behaviors) 401 exhibited bilateral projections in the VNC while narrowly tuned ANs (turning and eye grooming) 402 exhibited unilateral and smooth, putatively dendritic projections. This was correlated with the degree 403 404 of synchrony in the activity of pairs of ANs (Figure S8).

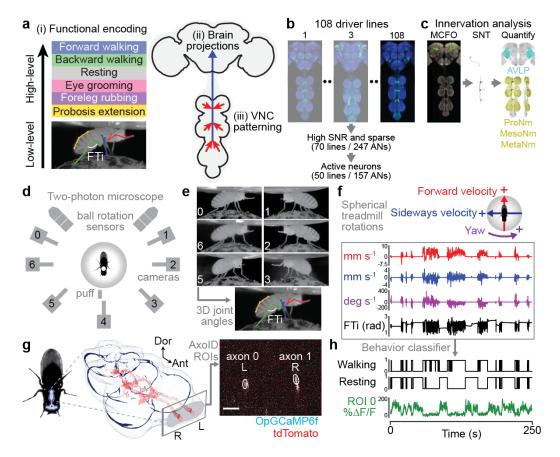
Strikingly, for all ANs that we examined in-depth, we found evidence of axon terminals within the VNC. Thus, ANs may not simply relay behavioral state signals to the brain but may also perform other roles. For example, they might contribute to motor control as components of central pattern generators (CPGs) that drive rhythmic movements [52], or rest-ANs might drive the muscle tone needed to maintain a natural resting posture. ANs might also participate in computing behavioral states. For example, we speculate that recurrent interconnectivity among PE-ANs might give rise

to their temporal integration and encoding of PE number in a manner that can be modeled by line attractors [43, 44]. Finally, ANs might contribute to action selection within the VNC. For example, eye groom-ANs might project to the contralateral T1 neuromere to suppress circuits driving other foreleg-dependent behaviors like walking and foreleg rubbing.

#### 415 3.4 Future work

Here we investigated animals that were generating spontaneous and puff-induced behaviors including 416 walking and grooming. However, ANs likely also encode other behavioral states, unmeasured internal 417 forces like posture-maintaining muscle stiffness, or even metabolic states. This is hinted at by the fact 418 that the neural activity of some ANs were not well explained by any of our behavioral regressors (e.g., 419 R87H02, R39G01, R69H10 and SS29633). Additionally, nearly one-third of the ANs we examined 420 were unresponsive, possibly due to the lack of relevant context. In line with this, we found that some 421 silent ANs could become very active during leg movements only when the spherical treadmill was 422 removed (e.g., SS38631 and SS51017) (Figure S9). Thus, future work should examine the encoding of 423 ANs in a variety of contexts including tethered flight. Finally, it would also be interesting to test the 424 degree to which AN encoding is genetically hardwired or capable of adapting following motor learning 425 or after injury [53, 54]. In summary, here we have shown that ANs encode high-level behaviors that 426 they convey to distinct integrative sensory and action selection centers in the brain. These findings 427 can accelerate our understanding of how ascending neurons in the mammalian spinal cord influence 428 decision-making in the brain [15, 16, 46, 55–57], and also inspire the development of more effective 429 430 algorithms for robotic sensory contextualization and action selection [2].

# 431 4 Figures



432

Figure 1: Large-scale functional and morphological screen of ascending neuron movement 433 encoding and nervous system targeting. (a) Schematic of the main questions addressed. (i) To 434 what extent do ascending neurons (ANs) encode high-level behaviors, or low-level movements? (ii) 435 Where in the brain do ANs convey behavioral states? (iii) To what extent is an AN's patterning within 436 the VNC predictive of its encoding? (b) Screening 108 driver lines. The projection patterns of sparse 437 lines with active ANs and high SNR (157 ANs) were examined in the brain and VNC. (c) These were 438 quantified using broad spFP and single-cell MCFO confocal imaging. (d) Overhead schematic of the 439 behavior measurement system used during two-photon microscopy. A camera array captures six views 440 of the animal. Two optic flow sensors measure ball rotations. A puff of  $CO_2$  (or air) is used to elicit 441 behavior from sedentary animals. (e) 2D poses are estimated for six cameras views using DeepFly3D. 442 These data are triangulated to quantify 3D poses and joint angles for six legs and the abdomen 443 (color-coded). The Femur-Tibia (FTi) joint angle is indicated (white). (f) Two optic flow sensors 444 measure rotations of the spherical treadmill as a proxy for forward (red), sideways (blue), and yaw 445 (purple) walking velocities. Positive directions of rotation (+) are indicated. (g, left) A volumetric 446 representation of the ventral nerve cord (VNC) including a reconstruction of ANs targeted by the 447 SS27485-spGal4 driver (red). Indicated are the dorsal-ventral ('Dor') and anterior-posterior ('Ant') 448 axes, as well as the fly's left (L) and right (R) sides. (g, right) Sample two-photon cross-section 449 image of the thoracic neck connective showing ANs that express OpGCaMP6f (cyan) and tdTomato 450 (red). AxoID is used to semi-automatically identify two axonal regions-of-interest (ROIs, white) on 451 the left ('L') and right ('R') sides of the connective. (h) Spherical treadmill rotations and joint angles 452 are used to classify behaviors. Binary classifications are then compared with simultaneously recorded 453 neural activity for 250 s trials of spontaneous and puff-elicited behaviors. Shown is an activity trace 454 from ROI 0 (green) in panel  $\mathbf{g}$ . 45F

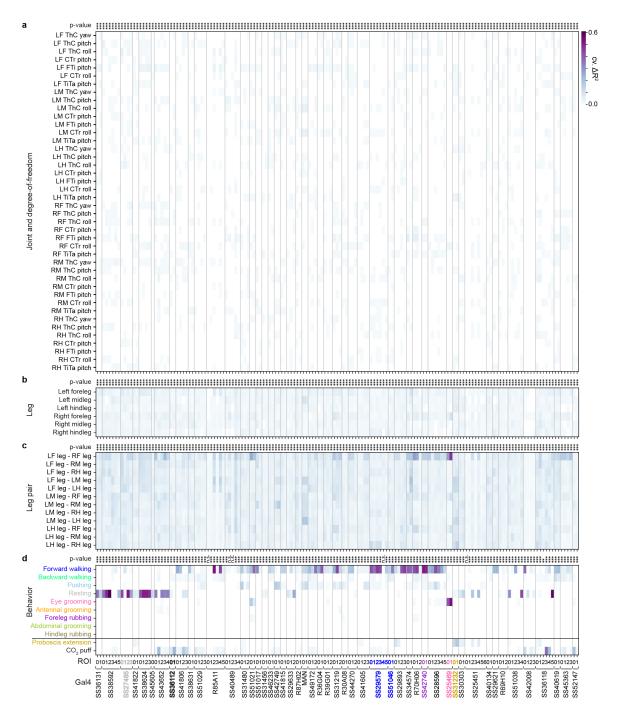


Figure 2: Ascending neurons encode high-level behaviors. Proportion of variance in AN activity that is uniquely explained by regressors (cross-validated  $\Delta R^2$ ) based on (a) joint movements, (b) the movements of individual legs, (c) the movements of pairs of legs, (d) high-level behaviors. Regression analyses were performed for 157 ANs recorded from 50 driver lines. Lines selected for more in-depth analysis are color-coded by the behavioral class best explaining their neural activity: SS27485 (resting), SS36112 (puff responses), SS29579 (walking), SS51046 (turning), SS42740 (foreleg movements), SS25469 (eye grooming), and SS31232 (proboscis extensions). Non-orthogonal regressors (PE and CO<sub>2</sub> puffs) are separated from the others. *P*-values report the F-statistic of overall significance of the complete regression model with none of the regressors shuffled (\*p<0.05, \*\*p<0.01, and \*\*\*p<0.001)

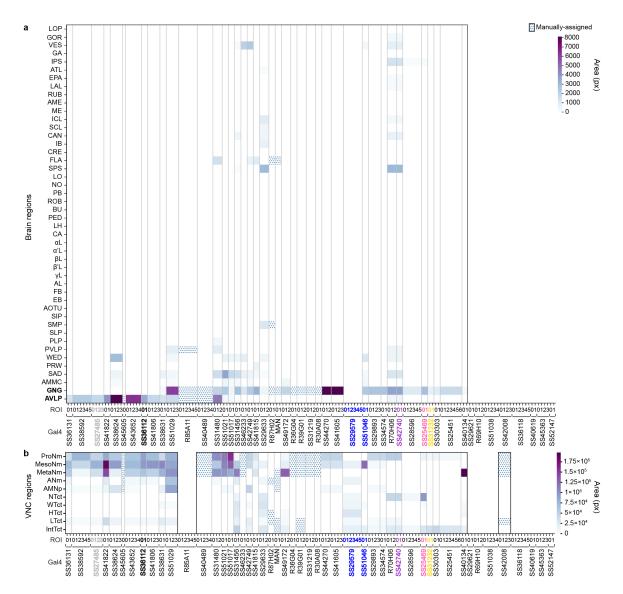


Figure 3: Ascending neurons principally project to the brain's AVLP and GNG and the VNC's leg neuromeres. Regional innervation of (a) the brain, or (b) the VNC. Data are for 157 ANs recorded from 50 driver lines and quantified through pixel-based analyses of MCFO labeled confocal images. Manually quantified driver lines are indicated (dotted). Lines for which projections could not be unambiguously identified are left blank. Lines selected for more in-depth evaluation are color-coded by the behavioral state that best explains their neural activity: SS27485 (resting), SS36112 (puff responses), SS29579 (walking), SS51046 (turning), SS42740 (foreleg-dependent behaviors), SS25469 (eye grooming), and SS31232 (proboscis extensions).

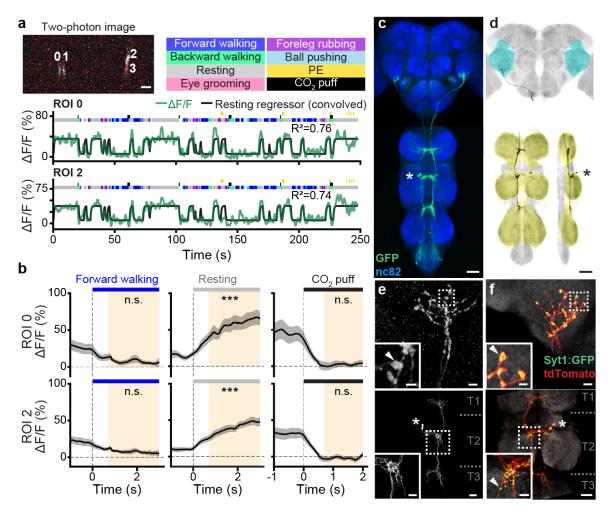


Figure 4: Functional and anatomical properties of ascending neurons encoding resting. (a) (top-left) Two-photon image of axons from an SS27485-Gal4 animal expressing OpGCaMP6f (cyan) and tdTomato (red). ROIs are numbered. Scale bar is 5 µm. (bottom) Behavioral epochs are color-coded. Representative  $\Delta F/F$  time-series from two ROIs (green) overlaid with a prediction (black) obtained by convolving resting epochs with a  $Ca^{2+}$  response function. Explained variance is indicated  $(R^2)$ . (b) Mean (solid line) and 95% confidence interval (gray shading) of  $\Delta F/F$  traces during epochs of forward walking (left), resting (middle), or CO<sub>2</sub> puffs (right). 0 s indicates the start of each epoch. Here and in Figures 5 - 9, data more than 0.7s after onset (yellow region) are compared with an otsu thresholded baseline (ANOVA and Tukey posthoc comparison, \*\*\*p < 0.001, \*\*p<0.01, \*p<0.05, n.s. not significant). (c) Standard deviation projection image of an SS27485-Gal4 nervous system expressing smFP and stained for GFP (green) and Nc82 (blue). Cell bodies are indicated (white asterisk). Scale bar is 40 µm. (d) Projection as in c but for one MCFOexpressing, traced neuron (black asterisk). The brain's AVLP (cyan) and VNC's leg neuromeres (yellow) are color-coded. Scale bar is 40 µm. (e, f) Higher magnification projections of (top) brains and (bottom) VNCs of SS27485-Gal4 animals expressing (e) the stochastic label MCFO, or (f) the synaptic marker, syt:GFP (green), and tdTomato (red). Insets magnify dashed boxes. Indicated are cell bodies (asterisks), bouton-like structures (white arrowheads), and VNC leg neuromeres ('T1, T2, T3'). Scale bars for brain images and insets are 5 µm and 2 µm, respectively. Scale bars for VNC images and insets are 20 µm and 10 µm, respectively.

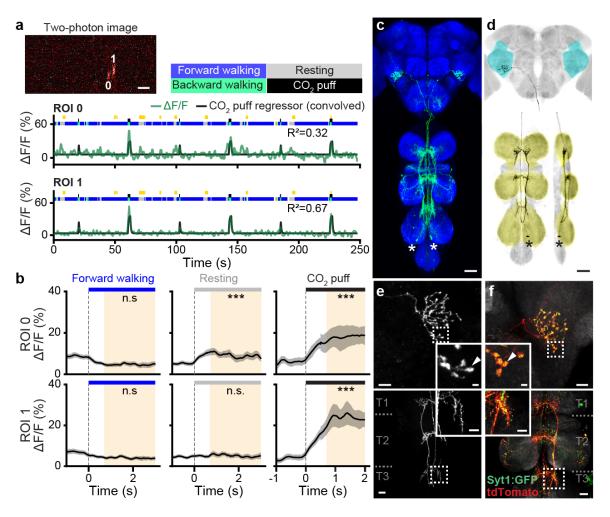


Figure 5: Functional and anatomical properties of ascending neurons responding to puffs. (a) (top-left) Two-photon image of axons from an SS36112-Gal4 animal expressing OpGCaMP6f (cyan) and tdTomato (red). ROIs are numbered. Scale bar is 5 µm. (bottom) Behavioral epochs are color-coded. Representative  $\Delta F/F$  time-series from two ROIs (green) overlaid with a prediction (black) obtained by convolving  $CO_2$  puff periods with a  $Ca^{2+}$  response function. Explained variance is indicated ( $R^2$ ). (b) Mean (solid line) and 95% confidence interval (gray shading) of  $\Delta F/F$  traces during epochs of forward walking (left), resting (middle), or CO<sub>2</sub> puffs (right). 0 s indicates the start of each epoch. (c) Standard deviation projection image for an SS36112-Gal4 nervous system expressing smFP and stained for GFP (green) and Nc82 (blue). Cell bodies are indicated (white asterisks). Scale bar is 40 µm. (d) Projection as in c but for one MCFO-expressing, traced neuron (black asterisks). The brain's AVLP (cyan) and VNC's leg neuromeres (vellow) are color-coded. Scale bar is 40 µm. (e, f) Higher magnification projections of (top) brains and (bottom) VNCs of SS36112-Gal4 animals expressing (e) the stochastic label MCFO, or (f) the synaptic marker, syt:GFP (green), and tdTomato (red). Insets magnify dashed boxes. Indicated are bouton-like structures (white arrowheads), and VNC leg neuromeres ('T1, T2, T3'). Scale bars for brain images and insets are 10 µm and 2 µm, respectively. Scale bars for VNC images and insets are 20 µm and 10 µm, respectively.

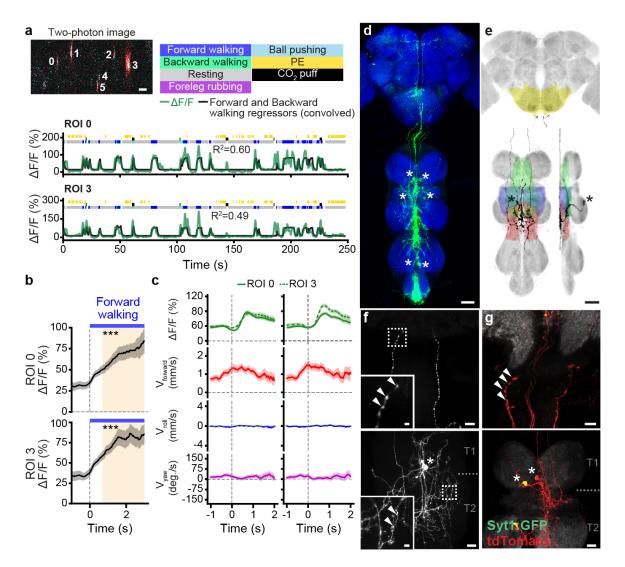


Figure 6: Functional and anatomical properties of ascending neurons encoding walking. (a) (top-left) Two-photon image of axons from an SS29579-Gal4 animal expressing OpGCaMP6f (cyan) and tdTomato (red). ROIs are numbered. Scale bar is 5 µm. (bottom) Behavioral epochs are color-coded. Representative  $\Delta F/F$  time-series from two ROIs (green) overlaid with a prediction (black) obtained by convolving forward walking epochs with a  $Ca^{2+}$  response function. Explained variance is indicated  $(R^2)$ . (b) Mean (solid line) and 95% confidence interval (gray shading) of  $\Delta F/F$ traces during epochs of forward walking. 0 s indicates the start of each epoch. (c) Fluorescence (OpGCaMP6f) event-based ball rotations for (left) ROI 3, or (right) ROI 0. Fluorescence events are time-locked to 0 s (green). Shown are mean and 95% confidence intervals for forward (red), roll (blue), and yaw (purple) ball rotational velocities. (d) Standard deviation projection image for a SS29579-Gal4 nervous system expressing smFP and stained for GFP (green) and Nc82 (blue). Cell bodies are indicated (white asterisks). Scale bar is 40 µm. (e) Projection as in d but for one MCFOexpressing, traced neuron (black asterisks). The brain's GNG (yellow) and VNC's intermediate (green), wing (blue), and haltere (red) tectulum are color-coded. Scale bar is 40 µm. (f, g) Higher magnification projections of (top) brains and (bottom) VNCs of SS29579-Gal4 animals expressing (f) the stochastic label MCFO, or (g) the synaptic marker, syt:GFP (green), and tdTomato (red). Insets magnify dashed boxes. Indicated are cell bodies (asterisks), bouton-like structures (white arrowheads), and VNC leg neuromeres ('T1, T2'). Scale bars for brain images and insets are 10 µm and 2 µm, respectively. Scale bars for VNC images and insets are 20 µm and 4 µm, respectively.

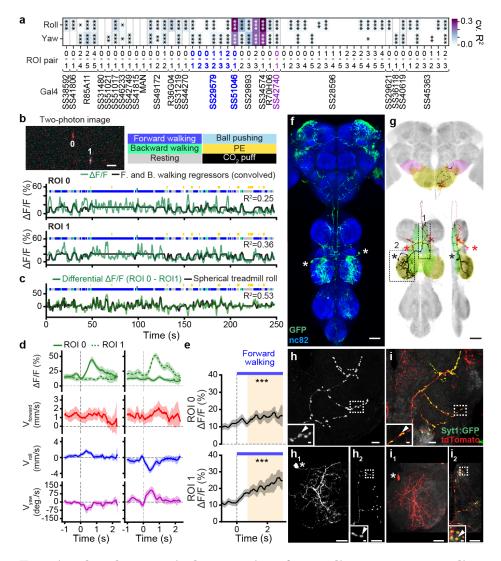


Figure 7: Functional and anatomical properties of ascending neurons encoding turning. (a) Variance explained by side-slip and turning for driver lines encoding forward walking. (b) (topleft) Two-photon image of axons from an SS51046-Gal4 animal expressing OpGCaMP6f (cyan) and tdTomato (red). ROIs are numbered. Scale bar is 5 µm. (bottom) Behavioral epochs are colorcoded. Representative  $\Delta F/F$  time-series from two ROIs (green) overlaid with a prediction (black) obtained by convolving forward walking epochs with a Ca<sup>2+</sup> response function. Explained variance is indicated ( $R^2$ ). (c) The differential  $\Delta F/F$  time-series obtained by subtracting the two ROIs (green) is overlaid with a prediction (black) from spherical treadmill roll rotations convolved with a  $Ca^{2+}$ response function. Explained variance is indicated  $(R^2)$ . (d) Fluorescence (OpGCaMP6f) eventbased ball rotations for (left) ROI 0, or (right) ROI 1. Fluorescence events are time-locked to 0 s (green). Shown are mean and 95% confidence intervals for forward (red), roll (blue), and yaw (purple) ball rotational velocities. (e) Mean (solid line) and 95% confidence interval (gray shading) of  $\Delta F/F$ traces during epochs of forward walking. 0 s indicates the start of each epoch. (f) Standard deviation projection image for a SS51046-Gal4 nervous system expressing smFP and stained for GFP (green) and Nc82 (blue). Cell bodies are indicated (white asterisks). Scale bar is 40 µm. (g) Projection as in **f** but for one MCFO-expressing, traced neuron (black asterisks). The brain's GNG (yellow), wedge (pink), and VNC's intermediate tectulum (green), and mesothoracic leg neuromere (yellow), are color-coded. Scale bar is 40 µm. (h, i) Higher magnification confocal z-projections of (top) brains and (bottom) VNCs of SS51046-Gal4 animals expressing (h) the stochastic label MCFO, or (i) the synaptic marker, syt:GFP (green), and tdTomato (red). Insets magnify dashed boxes. Indicated are cell bodies (asterisks), bouton-like structures (white arrowheads), and VNC leg neuromeres ('T1, T2'). Scale bars for brain images and insets are 10 µm and 2 µm, respectively. Scale bars for VNC images and insets are 20 µm and 2 µm, respectively.

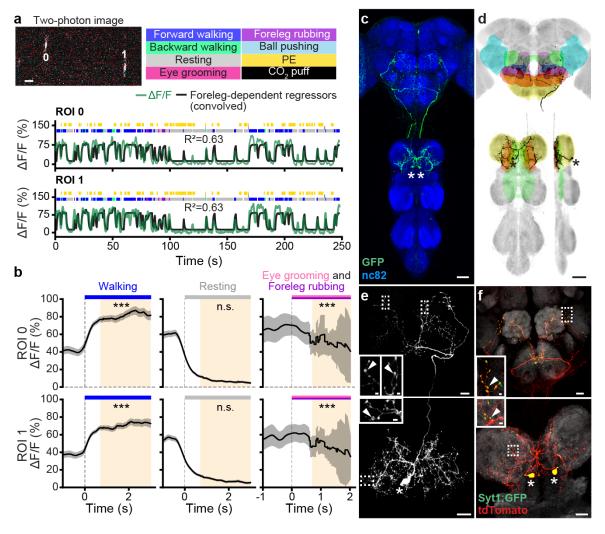


Figure 8: Functional and anatomical properties of ascending neurons encoding forelegdependent behaviors. (a) (top-left) Two-photon image of axons from an SS42740-Gal4 animal expressing OpGCaMP6f (cyan) and tdTomato (red). ROIs are numbered. Scale bar is 5 µm. (bottom) Behavioral epochs are color-coded. Representative  $\Delta F/F$  time-series from two ROIs (green) overlaid with a prediction (black) obtaind by convolving all foreleg-dependent behavioral (forward and backward walking as well as eye, antennal, and foreleg grooming) epochs with a  $Ca^{2+}$  response function. Explained variance is indicated  $(R^2)$ . (b) Mean (solid line) and 95% confidence interval (gray shading) of  $\Delta F/F$  traces during epochs of forward walking (left), resting (middle), or eye grooming and foreleg rubbing (right). 0 s indicates the start of each epoch. (c) Standard deviation projection image for an SS42740-Gal4 nervous system expressing smFP and stained for GFP (green) and Nc82 (blue). Cell bodies are indicated (white asterisks). Scale bar is 40 µm. (d) Projection as in c but for one MCFO-expressing, traced neuron (black asterisks). The brain's GNG (yellow), AVLP (cyan), SAD (green), VES (pink), IPS (blue), SPS (orange), and VNC's neck and intermediate tectulum (orange and green, respectively), and prothoracic leg neuromere (vellow) are color-coded. Scale bar is 40 µm. (e, f) Higher magnification confocal z-projections of (top) brains and (bottom) VNCs for SS42740-Gal4 animals expressing (e) the stochastic label MCFO, or (f) the synaptic marker, syt:GFP (green), and tdTomato (red). Insets magnify dashed boxes. Indicated are cell bodies (asterisks), and bouton-like structures (white arrowheads). Scale bars for brain images and insets are 20 µm and 2 µm, respectively. Scale bars for VNC images and insets are 20 µm and 2 µm, respectively.

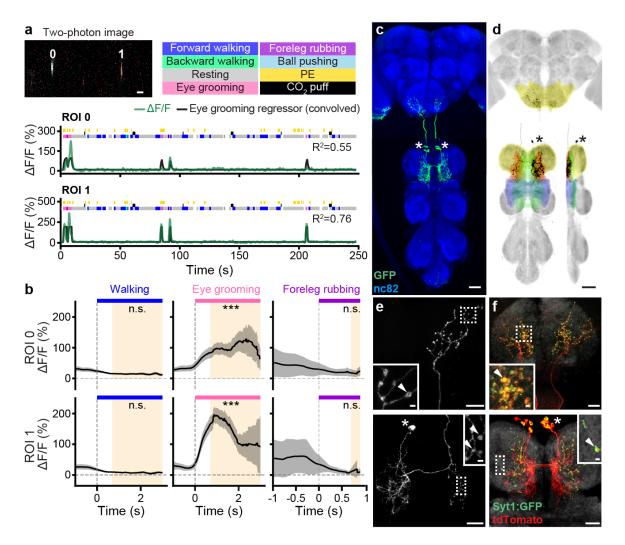


Figure 9: Functional and anatomical properties of ascending neurons encoding eve grooming. (a) (top-left) Two-photon image of axons from an SS25469-Gal4 animal expressing OpG-CaMP6f (cyan) and tdTomato (red). ROIs are numbered. Scale bar is 5 µm. (bottom) Behavioral epochs are color-coded. Representative  $\Delta F/F$  time-series from two ROIs (green) overlaid with a prediction (black) obtained by convolving eye grooming epochs with a  $Ca^{2+}$  response function. Explained variance is indicated  $(R^2)$ . (b) Mean (solid line) and 95% confidence interval (gray shading) of  $\Delta F/F$  traces during epochs of forward walking (left), eye grooming (middle), or foreleg rubbing (right). 0 s indicates the start of each epoch. (c) Standard deviation projection image for an SS25469-Gal4 nervous system expressing smFP and stained for GFP (green) and Nc82 (blue). Cell bodies are indicated (white asterisks). Scale bar is 40 µm. (d) Projection as in c but for one MCFO-expressing, traced neuron (black asterisks). The brain's GNG (vellow) and VNC's intermediate, neck and wing tectulum (green, red, and blue respectively), and prothoracic leg neuromere (yellow) are color-coded. Scale bar is 40 µm. (e, f) Higher magnification projections of (top) brains and (bottom) VNCs for SS25469-Gal4 animals expressing (e) the stochastic label MCFO, or (f) the synaptic marker, syt:GFP (green), and tdTomato (red). Insets magnify dashed boxes. Indicated are cell bodies (asterisks), and bouton-like structures (white arrowheads). Scale bars for brain images and insets are 20 µm and 2 µm, respectively. Scale bars for VNC images and insets are 20 µm and 2 µm, respectively.

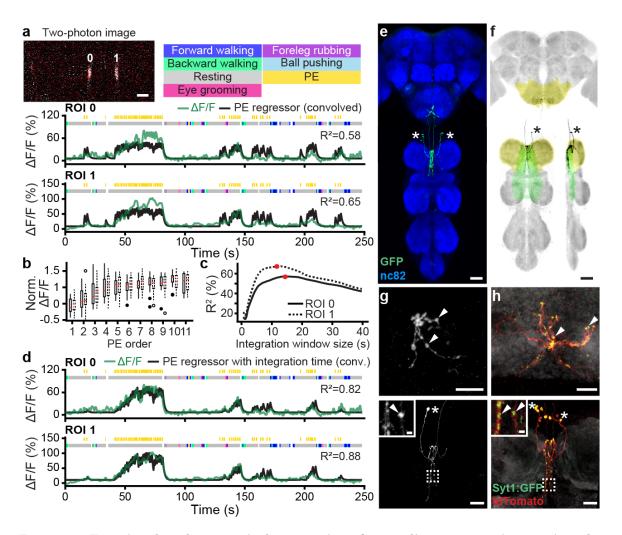


Figure 10: Functional and anatomical properties of ascending neurons integrating the number of proboscis extensions over time. (a) (top-left) Two-photon image of axons from an SS31232-Gal4 animal expressing OpGCaMP6f (cyan) and tdTomato (red). ROIs are numbered. Scale bar is 5 µm. (bottom) Behavioral epochs are color-coded. Representative  $\Delta F/F$  time-series from two ROIs (green) overlaid with a prediction (black) obtained by convolving proboscis extension epochs with a Ca<sup>2+</sup> response function. Explained variance is indicated ( $R^2$ ). (b)  $\Delta F/F$ , normalized with respect to the neuron's 90<sup>th</sup>%ile across the time-series, as a function of proboscis extension (PE) number within a PE train for ROIs 0 (solid boxes, filled circles) and 1 (dashed boxes, open circles). (c) Explained variance  $(R^2)$  between  $\Delta F/F$  time-series and a prediction from convolving proboscis extension epochs with a Ca<sup>2+</sup> response function and a time-window. Time-windows that maximize the correlation for ROIs 0 (solid line) and 1 (dashed line) are indicated (red circles). (d) Behavioral epochs are color-coded. Representative  $\Delta F/F$  time-series from two ROIs (green) are overlaid with a prediction (black) obtained by convolving proboscis extension epochs with a  $Ca^{2+}$  response function as well as a time window indicated in panel B (red circles). Explained variance is indicated  $(R^2)$ . (e) Standard deviation projection image for a SS31232-Gal4 nervous system expressing smFP and stained for GFP (green) and Nc82 (blue). Cell bodies are indicated (white asterisks). Scale bar is 40 µm. (f) Projection as in e but for one MCFO-expressing, traced neuron (black asterisks). The brain's GNG (yellow) and VNC's intermediate tectulum (green), and prothoracic leg neuromere (yellow) are color-coded. Scale bar is 40 µm. (g, h) Higher magnification projections of (top) brains and (bottom) VNCs for SS31232-Gal4 animals expressing (g) the stochastic label MCFO, or (h) the synaptic marker, syt:GFP (green), and tdTomato (red). Insets magnify dashed boxes. Indicated are cell bodies (asterisks), and bouton-like structures (white arrowheads). Scale bars for brain images are 10 µm. Scale bars for VNC images and insets are 20 µm and 2 µm, respectively.

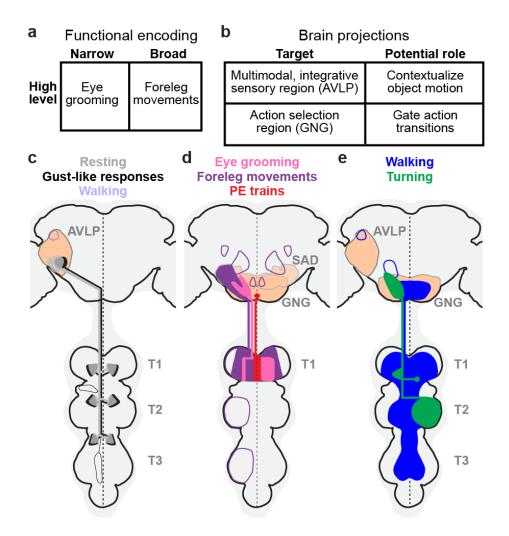


Figure 11: Summary of ascending neuron functional encoding, brain targeting, and VNC patterning. (a) Our functional screen shows that ANs encode high-level behaviors in a narrow (e.g., eye grooming), or broad (e.g., foreleg movements) manner. (b) Corresponding anatomical analysis shows that ANs primarily target the AVLP, a multimodal, integrative brain region, and the GNG, a region associated with action selection. (c, d) By comparing functional encoding with brain targeting and VNC patterning, we find that (c) signals critical for contextualizing object motion—walking, resting, and gust-like stimuli—are sent to the AVLP, while (d) signals indicating diverse ongoing behaviors are sent to the GNG, potentially to influence future action selection. (e) Broad (e.g., walking), or narrow (e.g., turning) behavioral encoding arises from diffuse and bilateral, or restricted and unilateral VNC innervations, respectively. (c-e) AN projections are color-coded by behavioral encoding. Axons and dendrites are not distinguished from one another. Brain and VNC regions are labelled. Frequently innervated brain regions—the GNG and AVLP—are highlighted (light orange). Less frequently innervated areas are outlined. The midline of the central nervous system is indicated (dashed line).

# 457 **5** Materials and Methods

# 458 5.1 Fly stocks

Split-Gal4 (spGal4) lines (SS\*\*\*\*\*) were generated by the Dickson laboratory and the FlyLight 459 project (Janelia Research Campus, Ashburn VA USA; see Table 1). GMR lines, MCFO-5 (R57C10-460 Flp2::PEST in su(Hw)attP8; ; HA-V5-FLAG), MCFO-7 (R57C10-Flp2::PEST in attP18;;HA-V5-461 FLAG-OLLAS) [26], and UAS-syt:GFP (Pw[+mC]=UAS-syt.eGFP1, w[\*];;) were obtained from the 462 Bloomington Stock Center. UAS-OpGCaM6f; UAS-tdTomato (; P20XUAS-IVS-Syn21-OpGCamp6F-463 p10 su(Hw)attp5; Pw[+mC]=UAS-tdTom.S3) was a gift from the Dickinson laboratory (Caltech, 464 Pasadena CA USA). UAS-smFP (; ; 10xUAS-IVS-myr::smGdP-FLAG (attP2)) was a gift from the 465 McCabe laboratory (EPFL, Lausanne CH). Experimental animals were kept at 25°C and 70% humidity on a 12-12 h day-light cycle. 467

# <sup>468</sup> 5.2 In vivo two-photon calcium imaging experiments

Two-photon imaging was performed on 3-6 days post-eclosion (dpe) female flies as described in [27] 469 with minor changes in the recording configuration. We imaged coronal sections of AN axons in the 470 cervical connective to avoid having neurons move outside the field of view due to behavior-related 471 tissue deformations. Imaging was performed using a Galvo-Galvo scanning system. Image dimensions 472 ranged from 256 x 192 pixels (4.3 fps) to 320 x 320 pixels (3.7 fps), depending on the location of axonal 473 regions-of-interest (ROIs) and the degree of displacement caused by animal behavior. During two-474 photon imaging, a 7-camera system was used to record fly behaviors as described in [28]. Rotations 475 of the spherical treadmill, and the timing of puff stimuli were also recorded. Air or  $CO_2$  puffs (0.08) 476 L/min) were controlled using either a custom Python script, or manually with an Arduino controller. 477 Puffs were delivered through a syringe needle positioned in front of the animal to stimulate behavior 478 in sedentary animals, or to interrupt ongoing behaviors. To synchronize signals acquired at different 479 sampling rates—optic flow sensors, two-photon images, puff stimuli, and videography—signals were 480 digitized using a BNC 2110 terminal block (National Instrument, USA) and saved using ThorSync 481 software (Thorlabs, USA). Sampling pulses were then used as references to align data based on the 482 onset of each pulse. Then signals were interpolated using custom Python scripts. 483

# <sup>484</sup> 5.3 Immunofluorescence tissue staining and confocal imaging

<sup>485</sup> Fly brains and VNCs from 3-6 dpe female flies were dissected and fixed as described in [27] with <sup>486</sup> small modifications in staining including antibodies and incubation conditions (see details below). <sup>487</sup> Both primary (rabbit anti-GFP at 1:500, Thermofisher RRID: AB\_2536526; mouse anti-Bruchpilot / <sup>488</sup> nc82 at 1:20, Developmental Studies Hybridoma Bank RRID: AB\_2314866) and secondary antibodies <sup>489</sup> (goat anti-rabbit secondary antibody conjugated with Alexa 488 at 1:500; Thermofisher, RRID: <sup>490</sup> AB\_143165; goat anti-mouse secondary antibody conjugated with Alexa 633 at 1:500; Thermofisher, <sup>491</sup> RRID: AB\_2535719) for smFP and nc82 staining were performed at room temperature for 24h.

To perform high-magnification imaging of MCFO samples, nervous tissues were incubated with pri-492 mary antibodies: rabbit anti-HA-tag at 1:300 dilution (Cell Signaling Technology, RRID:AB\_1549585). 493 rat anti-FLAG-tag at 1:150 dilution (DYKDDDDK; Novus, RRID:AB\_1625981), and mouse anti-494 Bruchpilot/nc82 at 1:20 dilution. These were diluted in 5% normal goat serum in PBS with 1%495 Triton-X (PBSTS) for 24 h at room temperature. The samples then were rinsed 2-3 times in PBS 49F with 1% Triton-X (PBST) for 15 min before incubation with secondary antibodies: donkey antirabbit secondary antibody conjugated with AlexaFluor 594 at 1:500 dilution (Jackson ImmunoRe-498 search Labs, RRID:AB\_2340621), donkey anti-rat secondary antibody conjugated with AlexaFluor 499 647 at 1:200 dilution (Jackson ImmunoResearch Labs, RRID:AB\_2340694), and donkey anti-mouse 500 secondary antibody conjugated with AlexaFluor 488 at 1:500 dilution (Jackson ImmunoResearch 501 Labs, RRID:AB\_2341099). These were diluted in PBSTS for 24 h at room temperature. Again, 502 samples were rinsed 2-3 times in PBS with 1% Triton-X (PBST) for 15 min before incubation with 503 the last diluted antibody: rabbit anti-V5-tag (GKPIPNPLLGLDST) conjugated with DyLight 550 504 at 1:300 dilution (Cayman Chemical, 11261) for another 24 h at room temperature. 505

To analyze single neuron morphological patterning, we crossed spGal4 lines with MCFO-7 [26]. Dissection and MCFO staining were performed by Janelia FlyLight according to the FlyLight 'IHC-

MCFO' protocol: https://www.janelia.org/project-team/flylight/protocols. Samples were 508 imaged on an LSM710 confocal microscope (Zeiss) with a Plan-Apochromat 20x /0.8 M27 objective. 509 To prepare samples expressing tdTomato and syt:GFP, we chose to only stain tdTomato to min-510 imize false positive signals for the synaptotagmin marker. Samples were incubated with a diluted 511 primary antibody: rabbit polyclonal anti-DsRed at 1:1000 dilution (Takara Biomedical Technology, 512 RRID: AB\_10013483) in PBSTS for 24 h at room temperature. After rinsing, samples were then 513 incubated with a secondary antibody: donkey anti-rabbit secondary antibody conjugated with Cy3 514 (Jackson ImmunoResearch Labs, RRID:AB\_2307443). Finally, all samples were rinsed 2–3 times for 515 10 min each in PBST after staining and then mounted onto glass slides with bridge coverslips in 516 Slowfade mounting-media (Thermofisher, S36936). 517

<sup>518</sup> Confocal imaging was performed as described in [27]. In addition, high-resolution images for <sup>519</sup> visualizing fine structures were captured using a 40x oil-immersion objective lens with an NA of <sup>520</sup> 1.3 (Plan-Apochromat 40x/1.3 DIC M27, Zeiss) on an LSM700 confocal microscope (Zeiss). The <sup>521</sup> zoom factor was adjusted based on the ROI size of each sample between 84.23×84.23  $\mu$ m<sup>2</sup> and <sup>522</sup> 266.74×266.74  $\mu$ m<sup>2</sup>. For high-resolution imaging, z-steps were fixed at 0.33  $\mu$ m. Images were de-<sup>523</sup> noised, their contrasts were tuned, and standard deviation z-projections were generated using Fiji <sup>524</sup> ([58]).

# 525 5.4 Two-photon image analysis

Raw two-photon imaging data were converted to gray-scale \*.tiff image stacks for both green and red 526 channels using custom Python scripts. RGB image stacks were then generated by combining both 527 image stacks in Fiji ([58]). We used AxoID to perform ROI segmentation and to quantify fluorescence 528 intensities. Briefly, AxoID was used to register images using cross-correlation and optic flow-based 529 warping [27]. Then, raw and registered image stacks underwent ROI segmentation, allowing  $\%\Delta F/F$ 530 values to be computed across time from absolute ROI pixel values. Simultaneously, segmented RGB 531 image stacks overlaid with ROI contours were generated. Each frame of these segmented image stacks 532 was visually examined to confirm AxoID segmentation, or to perform manual corrections using the 533 AxoID GUI. In these cases, manually corrected  $\Delta \Delta F/F$  and segmented image stacks were updated. 534

#### 535 5.5 Behavioral data analysis

To reduce computational and data storage requirements, we recorded behaviors at 30 fps. This is nearly the Nyquist frequency for rapid walking (up to 16 step cycles/s [59]).

3D joint positions were estimated using DeepFly3D [28]. Due to the amount of data collected, 538 manual curation was not practical. We therefore classified points as outliers when the absolute value 539 of any of their coordinates (x, y, z) was greater than 5 mm (much larger than the fly's body size). 540 Furthermore, we made the assumption that joint locations would only be incorrectly estimated for 541 one of the three cameras used for triangulation. The consistency of the location across cameras could be evaluated using the reprojection error. To identify a camera with a bad prediction, we calculated 543 the reprojection error only using two of the three cameras. The outlier was then replaced with the 544 triangulation result of the pair of cameras with the smallest reprojection error. The output was 545 further processed and converted to angles as described in [60]. 546

We classified behaviors based on a combination of 3D joint angle dynamics and rotations of the 547 spherical treadmill. First, to capture the temporal dynamics of joint angles, we calculated wavelet 548 coefficients for each angle using 15 frequencies between 1 Hz and 15 Hz [61, 62]. We then trained a 549 histogram gradient boosting classifier [63] using joint angles, wavelet coefficients, and ball rotations as 550 features. Because flies perform behaviors in an unbalanced way (some behaviors are more frequenty 551 than others), we balanced our annotations using SMOTE [64]. The model was validated using 5-fold, 552 three times repeated, stratified cross-validation. Fly speeds and heading directions were estimated 553 554 using optical flow sensors [27]. To further improve the accuracy of the onset of walking we applied empirically-determined thresholds (pitch: 0.0038; roll: 0.0038; yaw: 0.014) to the rotational veloci-555 ties of the spherical treadmill. The rotational velocities were smoothed and denoised using a moving 556 average filter (length 81). All frames that were not previously classified as grooming or pushing (and 557 for which the spherical treadmill was classified as moving) were labeled as 'walking'. These were 558 furthered subdivided into forward or backward walking depending on the sign of the pitch velocity. 559 Conversely, frames for which the spherical treadmill was not moving were labeled as 'resting'. To 560

reduce the effect of optical flow measurement jitter, walking and resting labels were processed using a hysteresis filter that only changes state if at least 15 consecutive frames are in a new state. Classification in this manner was generally effective but most challenging for kinematically similar behaviors like eye- and antennal-grooming, or hindleg rubbing and abdominal grooming (Figure S10).

Proboscis extension (PE) events were classified based on the length of the proboscis (Figure S2). 565 First, we trained a deep network [38] to identify the tip of the proboscis and a static landmark 566 (the ventral part of the eye) from side-view camera images. Then, the distance between the tip of 567 proboscis and this static landmark was calculated to obtain the PE length for each frame. A semi-568 automated PE event classifier was made by first denoising the traces of PE distances using a median 569 filter with a 0.3 s running average. Traces were then normalized to be between 0 (baseline values) 570 and 1 (maximum values). Next, PE speed was calculated using a data point interval of 0.1 s to 571 detect significant changes in PE length. This way, only peaks larger than a manually set threshold of 572  $0.03 \Delta \text{norm.length}/0.1$  s were considered. Because the peak speed usually occurred during the rising 573 phase of a PE, a kink in PE speed was identified by multiplying the peak speed with an empirically-574 determined factor ranging from 0.4 to 0.6, and finding that speed within 0.5 s prior to the peak speed. 575 The end of a PE was the time-point at which the same speed was observed within 2 s after the peak 576 PE speed. This filtered out occasions where the proboscis remained extended for long periods of time. 577 All quantified PE lengths and durations were then used to build a filter to remove false positives. 578

<sup>579</sup> PEs were then binarized to define PE epochs.

To quantify animal movements when the spherical treadmill was removed, we manually thresholded the variance of pixel values from a side view camera within a region of the image that included the fly. Pixel value changes were calculated using a running window of 0.2 s. Next, the standard deviation of pixel value changes was generated using a running window of 0.25 s. This trace was then smoothed and values lower than the empirically-determined threshold were called 'resting' epochs. The remainder were considered 'movement' periods.

# 556 Regression analysis of PE integration time

To investigate the integrative nature of the PE-AN responses, we convolved PE traces with uniform 587 time windows of varying sizes. This convolution was performed such that the fluorescence at each time 588 point would be the sum of fluorescence during the previous 'window\_size' frames (i.e., not a centered 589 sliding window but one that only uses previous time points), effectively integrating over the number 590 of previous PEs. This integrated signal was then masked such that all time points where the fly was 591 not engaged in PE were set to zero. Then, this trace was convolved with a calcium indicator decay 592 kernel, notably yielding non-zero values in the time intervals between PEs. We then determined the 593 explained variance as described elsewhere and finally chose a window size maximizing the explained 594 variance. 595

# 596 5.7 Linear modeling of neural fluorescence traces

Each regression matrix contains elements corresponding to the results of a ridge regression model for 597 predicting the time-varying fluorescence  $(\% \frac{\Delta F}{F})$  of ANs using specific regressors (e.g., low-level joint 598 angles, or high-level behaviors). To account for slow calcium indicator decay dynamics, each regressor 599 was convolved with a calcium response function. The half-life of the calcium response function 600 was chosen from a range of  $0.2 \,\mathrm{s}$  to  $0.95 \,\mathrm{s}$  [65] in  $0.05 \,\mathrm{s}$  steps, in order to maximize the variance in 601 fluorescence traces that convolved regressors could explain. The rise time was fixed at 0.1415 s [65]. 602 The ridge penalty parameter was chosen using nested 10-fold stratified cross-validation [66]. The 603 intercept and weights of all models were restricted to be positive, limiting our analysis to excitatory 604 neural activity. Values shown in the matrices are the mean of 10-fold stratified cross-validation. We 605 calculated Unique (UEV) and All-Explained Variance (AEV) by temporally shuffling the regressor 606 607 in question, or all other regressors, respectively [4]. We tested the overall significance of our models using an F-statistic to reject the null hypothesis that the model does not perform better than an 608 intercept-only model. The prediction of individual traces were performed using a single regressor 609 plus intercept. Therefore they were not regularized. 610

# <sup>611</sup> 5.8 Behavior-based neural activity analysis

For a given behavior,  $\Delta F/F$  traces were compiled, cropped, and aligned with respect to their onset times. Mean and 95% confidence intervals for each time point were then calculated from these data. Because the duration of each behavioral epoch was different, we only computed mean and confidence intervals for epochs that had at least 5 data points.

To test if each behavior-triggered average  $\Delta F/F$  was significantly different from the baseline, first, 616 we aligned and upsampled fluorescence data that were normalized between 0 (baseline mean) and 617 1 (maximum) for each trial. For each behavioral epoch, the first 0.7 s of data were removed. This 618 avoided contaminating signals with neural activity from preceding behaviors (due to the slow decay 619 dynamics of OpGCaMP6f). Next, to be conservative in judging whether data reflected noisy baseline 620 or real signals, we studied their distributions. Specifically, we tested the normality of twenty resampled 621 groups of 150 bootstrapped datapoints—a size that reportedly maximizes the power of the Shapiro-622 Wilk test [67]. If a majority of results did not reject the null hypothesis, the entire recording was 623 considered baseline noise and the  $\Delta F/F$  for a given behavioral class was not considered significantly 624 different from baseline. On the other hand, if the datapoints were not normally distributed, the 625 baseline was determined using an Otsu filter. For recordings that passed this test of normality, if 626 the majority of six ANOVA tests on the bootstrapped data rejected the null hypothesis and the 627 datapoints of a given behavior were significantly different (\*\*\*p < 0.001, \*\*p < 0.01, \*p < 0.05) from 628 baseline (as indicated by a posthoc Tukey test), these data were considered signal and not noise. 629

To analyze PE-AN responses to each PE during PE trains, putative trains of PEs were manually identified to exclude discrete PE events. PE trains included at least 3 consecutive PEs in which each PE lasted at least 1 s and there was less than 3 s between each PE. Then, the mean fluorescence of each PE was computed for 25 PE trains (n=11 animals). The median, IQR, and 1.5 IQR were then computed for PEs depending on their ordered position within their PE trains. We focused our analysis on the first 11 PEs because they had a sufficiently large amount of data.

# 5.9 Neural fluorescence-triggered averaging of spherical treadmill rotational velocities

A semi-automated neural fluorescence event classifier was constructed by first denoising  $\Delta F/F$  traces 638 by averaging them using a 0.6 s running window. Traces were then normalized to be between 0 639 (their baseline values) and 1 (their maximum values). To detect large deviations, the derivative of 640 the normalized  $\Delta F/F$  time-series was calculated at an interval of 0.1 s. Only peaks greater than an 641 empirically determined threshold of 0.03 dnorm  $\Delta F/F / 0.1$  s were considered events. Because peak 642 fluorescence derivatives occurred during the rising phase of neural fluorescence events, the onset of a 643 fluorescence event was identified as the time where the  $\Delta F/F$  derivative was 0.4-0.6x the peak within 644 the preceding 0.5 s time window. The end of the event was defined as the time that the  $\Delta F/F$  signal 645 returned to the amplitude at event onset before the next event. False positives were removed by 646 filtering out events with amplitudes and durations that were lower than the empirically determined 647 threshold. Neural activity event analysis for turn-ANs was performed by testing if the mean nor-648 malized fluorescence event for one ROI was larger than the other ROI by an empirically determined factor of 0.2x. Corresponding ball rotations for events that pass this criteria were then collected. 650 Fluorescence events onsets were then set to 0 s and aligned with spherical treadmill rotations. Using 651 these rotational velocity data, we calculated the mean and 95% confidence intervals for each time 652 point with at least five data points. A 1 s period before each fluorescence event was also analyzed as 653 a baseline for comparison. 654

# 555 5.10 Brain and VNC confocal image registration

<sup>656</sup> All confocal images, except for MCFO image stacks, were registered based on nc82 neuropil staining.
 <sup>657</sup> We built a template and registered images using the CMTK munger extension [68]. Code for this
 <sup>658</sup> registration process can be found at: https://github.com/NeLy-EPFL/MakeAverageBrain/tree/
 <sup>659</sup> workstation. Brain and VNC images were registered to JRC 2018 templates [69] using the Computational Morphometry Toolkit: https://www.nitrc.org/projects/cmtk. The template brain and
 <sup>661</sup> VNC can be downloaded here: https://www.janelia.org/open-science/jrc-2018-brain-templates.

# <sup>662</sup> 5.11 Analysis of individual AN innervation patterns

Single AN morphologies were traced by masking MCFO confocal images using either active tracing, 663 or manual background removal in Fiji [58]. Axons in the brain were manually traced using the Fiji 664 plugin 'SNT'. Most neurites in the VNC were isolated by (i) thresholding to remove background 665 noise and outliers, and (ii) manually masking debris in images. In the case of ANs from SS29579. 666 a band-pass color filter was applied to isolate an ROI that spanned across two color channels. The 667 boundary of the color filter was manually tuned to acquire the stack for a single neuron mask. 668 After segmentation, the masks of individual neurons were applied across frames to calculate the 669 intersectional pixel-wise sum with another mask containing either (i) neuropil regions of the brain and 670 VNC, (ii) VNC segments, or (iii) left and right halves of the VNC. Brain and VNC neuropil regions and 671 their corresponding abbreviations were according to established nomenclature [70]. Neuropil region 672 masks can be downloaded here: https://v2.virtualflybrain.org. These were also registered 673 to the JRC 2018 template. Masks for T1, T2, and T3 VNC segments were based on previously 674 delimited boundaries [37]. The laterality of a neuron's VNC innervation was calculated as the ratio 675 of the absolute difference between its left and right VNC innervations divided by its total innervation. 676 Masks for the left and right VNC were generated by dividing the VNC mask across its midline. 677

# <sup>678</sup> 5.12 AxoID: a deep learning-based software for tracking axons in imaging <sup>679</sup> data

AxoID aims to extract the GCaMP fluorescence values for axons present on coronal section two-photon
 microscopy imaging data. In this manuscript, it is used to record activity from ascending neurons
 (ANs) passing through the *Drosophila melanogaster* cervical connective. Fluorescence extraction
 works by performing the following three main steps (Figure S11A). First, during a *detection* stage,
 ROIs corresponding to axons are segmented from images. Second, during a *tracking* stage, these
 ROIs are tracked across frames. Third, *fluorescence* is computed for each axon over time.

To track axons, we used a two-stage approach: detection and then tracking. This allowed us to improve each problem separately without the added complexity of developing a detector that must also do tracking. Additionally, this allowed us to detect axons without having to know how many there are in advance. Lastly, significant movement artifacts between consecutive frames pose additional challenges for robustness in temporal approaches while, in our case, we can apply the detection on a frame-by-frame basis. However, we note that we do not leverage temporal information.

#### <sup>692</sup> 5.12.1 Detection

Axon detection consists of finding potential axons by segmenting the background and foreground of each image. An ROI or putative axon is defined as a group of connected pixels segmented as foreground. Pixels are considered connected if they are next to one another.

<sup>696</sup> By posing detection as a segmentation problem, we have the advantage of using standard computer <sup>697</sup> vision methods like thresholding, or artificial neural networks that have been developed for medical <sup>698</sup> image segmentation. Nevertheless, this simplicity has a drawback: if axons appear very close to one <sup>699</sup> another and their pixels are connected, they may be segmented as one ROI rather than two. We try <sup>700</sup> to address this issue using an ROI separation approach described later.

Image segmentation is performed using deep learning on a frame-by-frame basis, whereby a network generates a binary segmentation of a single image. As a post-processing step, all ROIs smaller than a minimum size are discarded. Here, we empirically chose 11 pixels as the minimum size as a trade-off between removing small spurious regions while still detecting small axons.

We chose to use a U-Net model [71] with slight modifications because of its, or its derivatives', 705 performance on recent biomedical image segmentation problems [72–74]. We add zero-padding to the 706 convolutions to ensure that the output segmentation has the same size as the input image, thus fully 707 segmenting it in a single pass, and modify the last convolution to output a single channel rather than 708 two. Batch normalization [75] is used after each convolution and its non-linearity function. Finally, 709 we reduce the width of the network by a factor of 4: each feature map has 4 times fewer channels 710 than the original U-Net, not counting the input or output. The input pixel values are normalized to 711 the range [-1, 1], and the images are sufficiently zero-padded to ensure that the size can be correctly 712 reduced by half at each max-pooling layer. 713

To train the deep learning network, we use the Adam optimizer [76] on the binary cross-entropy 714 loss with weighting. Each background pixel is weighted based on its distance to the closest ROI, given 715 by  $1 + exp(-\frac{d^2}{3})$  with d the Euclidean distance, plus a term that increases if the pixel is a border 716 between two axons, given by  $exp(-\frac{d_1+d_2}{6}^2)$  with  $d_1$  and  $d_2$  as the distances to the two closest ROIs, as in [71]. These weights aim to encourage the network to correctly segment the border of the ROI 717 718 and to keep a clear separation between two neighboring regions. At training time, the background and foreground weights are scaled by  $\frac{b+f}{2b}$  and  $\frac{b+f}{2f}$ , respectively, to take into account the imbalance 719 720 in the number of pixels, where b and f are the quantity of background and foreground (i.e., ROI) 721 pixels in the entire training dataset. To evaluate the resulting deep network, we use the Sørensen-Dice 722 coefficient [77,78] at the pixel level, which is equivalent to the F1-score. The training is stopped when 723 the validation performance does not increase anymore. 724

The network was trained on a mix of experimental and synthetic data. We also apply random 725 gamma corrections to the training input images, with  $\gamma$  sampled in [0.7, 1.3] to keep reasonable 726 values, and to encourage robustness against intensity variations between experiments. The target 727 segmentation of the axons on the experimental data was generated with conventional computer vision 728 methods. First, the images were denoised with the non-local means algorithm [79] using the Python 729 implementation of OpenCV [80]. We used a temporal window size of 5, and performed the denoising 730 separately for the red and green channels, with a filter strength h = 11. The grayscale result was 731 then taken as the per-pixel maximum over the channels. Following this, the images were smoothed 732 with a Gaussian kernel of standard deviation 2 pixels, and thresholded using Otsu's method [81]. A 733 final erosion was applied and small regions below 11 pixels were removed. All parameter values were 734 set empirically to generate good qualitative results. In the end, the results were manually filtered to 73 keep only data with satisfactory segmentation. 736

Because the experimental data have a fairly simply visual structure, we constructed a pipeline in 737 Python to generate synthetic images visually similar to real ones. This was achieved by first sampling 738 an image size for a given synthetic experiment, then by sampling 2D Gaussians over it to simulate 739 the position and shape of axon cross-sections. After this, synthetic tdTomato levels were uniformly 740 sampled and GCaMP dynamics were created for each axons by convolving a GCaMP response kernel 741 with Poisson noise to simulate spikes. Then, the image with the Gaussian axons was deformed 742 multiple times to make different frames with artificial movement artifacts. Eventually, we sampled 743 from the 2D Gaussians to make the axons appear pixelated, and added synthetic noise to the images. 744 In the end, we chose a deep learning-based approach because our computer vision pipeline alone 745 was not be robust enough. Our pipeline is used to generate a target segmentation dataset from which 746 we manually select a subset of acceptable results. These results are then used to train the deep 747 learning model. 748

Fine-tuning At the beginning of the detection stage, an optional fine-tuning of the network can be applied to try to improve the segmentation of axons. The goal is to have a temporary network adapted to the current data for better performance. To do this, we train the network on a subset of experimental frames using automatically generated target segmentations.

The subset of images is selected by finding a cluster of frames with high cross-correlation-based 753 similarity. For this, we only consider the tdTomato channel to avoid the effects of GCaMP dynamics. 754 Each image is first normalized by its own mean pixel intensity  $\mu$  and standard deviation  $\sigma$ :  $p(i, j) \leftarrow$ 755  $\frac{p(i,j)-\mu}{\sigma}$ , where p(i,j) is the pixel intensity p at the pixel location i, j. The cross-correlation is then 756 computed between each pair of normalized images  $p_m$  and  $p_n$  as  $\sum_{i,j} p_m(i,j) \cdot p_n(i,j)$ . Afterwards, 757 we take the opposite of the cross-correlation as a distance measure and use it to cluster the frames 758 with the OPTICS algorithm [82]. We set the minimal number of sample for a cluster to 20, in order 759 to maintain at least 20 frames for fine-tuning, and a maximum neighborhood distance of half the 760 largest distance between frames. Finally, we select the cluster of images with the highest average 761 cross-correlation (i.e., the smallest average distance between its elements). 762

Then, to generate a target segmentation image for these frames, we take their temporal average and optionally smooth it, if there are less than 50 images, to help remove the noise. The smoothing is done by filtering with a Gaussian kernel of standard deviation 1 pixel, then median filtering over each channel separately. The result is then thresholded through a local adaptive method, computed by taking the weighted mean of the local neighborhood of the pixel, subtracted by an offset. We apply Gaussian weighting over windows of  $25 \times 25$  pixels, with an offset of -0.05, determined empirically.

Finally, we remove regions smaller than 11 pixels. The result serves as a target segmentation image for all of the fine-tuning images.

The model is then trained on 60% of these frames with some data augmentation, while the other 40% are used for validation. The fine-tuning stops automatically if the performance on the validation frames drops. This avoids bad generalization for the rest of the images. The binary cross-entropy loss is used, with weights computed as discussed previously. For the data augmentation, we use random translation ( $\pm 20\%$ ), rotation ( $\pm 10^\circ$ ), scaling ( $\pm 10\%$ ), and shearing ( $\pm 5^\circ$ ).

776 5.12.2 Tracking

Once the regions of interest are segmented, the next step of the pipeline consists of tracking the axons through time. This means defining which axons exist, and then finding the ROI they correspond to in each frame.

Tracking template To accomplish this, the tracker records the number of axons, their locations with respect to one another, and their areas. It stores this information into what we call the 'tracker template'. Then, for each frame, the tracker matches its template axons to the ROIs to determine which regions correspond to which axons.

The tracker template is built iteratively. It is first initialized and then updated by matching 784 with all experimental data. The initialization depends on the optional fine-tuning in the detection 785 step. If there is fine-tuning, then the smoothed average of the similar frames and its generated 786 segmentation are used. Otherwise, one frame of the experiment is automatically selected. For this, 787 AxoID considers only the frames with a number of ROIs equal to the most frequent number of ROIs, 788 and then selects the image with the highest cross-correlation with the temporal average of these 789 frames. It is then smoothed and taken with the segmentation produced by the detection network as 790 initialization. The cross-correlation and smoothing are computed identically as in the fine-tuning. 791 Each ROI in the initialization segmentation defines an axon in the tracker template, with its area 792 and position recorded as initial properties. 793

Afterwards, we update them by matching each experimental frame to the tracker template. It consists of assigning the ROI to the tracker axons, and then using these regions' areas and positions to update the tracker. The images are matched sequentially, and the axons properties are taken as running averages of their matched regions. For example, considering the  $n^{th}$  match, the area of an axon is updated as:

$$area \leftarrow \frac{area * n + area_{ROI}}{n+1}$$

Because of this, the last frames are matched to a tracker template that is different from the one used for the first frames. Therefore, we fix the axons properties after the updates and match each frame again to obtain the final identities of the ROIs.

Matching To assign axon identities to the ROIs of a frame, we perform a matching between them as discussed above. To solve it, we define a cost function for matching a template axon to a region which represents how dissimilar they are. Then, using the Hungarian assignment algorithm [83], we find the optimal matching with the minimum total cost (Figure S11B).

Because some ROIs in the frame may be wrong detections, or some axons may not be correctly detected, the matching has to allow for the regions and axons to end up unmatched for some frames. Practically, we implement this by adding "dummy" axons to the matching problem with a flat cost. To guarantee at least one real match, the flat cost is set to the maximum between a fixed value and the minimum of the costs between regions and template axons with a margin of 10%:  $dummy = max(v, 1.1 \cdot min(\text{costs}))$  with v = 0.3 the fixed value. Then, we can use the Hungarian method to solve the assignment, and all ROIs linked to these dummy axons can be considered unmatched.

We define the cost of assigning a frame's ROI i to a tracker template axon k by their absolute difference in area plus the mean cost of an optimal inner matching of the other ROI to the other axons assuming i and k are already matched:

799

$$\operatorname{cost}(i,k) = w_{area}|area_i - area_k| + \frac{1}{N_{ROI} - 1} \sum_{i' \neq i} \operatorname{cost}'(i',k_{i'}^*)$$

where  $w_{area} = 0.1$  is a weight for balancing the importance of the area,  $N_{ROI}$  is the number of ROI in the frame, and  $\cot'(i', k_{i'}^*)$  is the inner cost of assigning region  $i' \neq i$  to axon  $k_{i'}^* \neq k$  selected in an "inner" assignment problem, see below. In other words, the cost is relative to how well the rest of the regions and axons match if we assume that i and k are already matched.

The optimal inner matching is computed through another Hungarian assignment, for which we define another cost function. For this "inner" assignment problem, the cost of matching an ROI  $i' \neq i$ and a template axon  $k' \neq k$  is defined by how far they are and their radial difference with respect to the matched *i* and *k*, plus their difference in area:

$$cost'(i',k') = \left(\frac{w_{dist}}{\eta_{dist}}||(x_{i'}-x_i) - (x_{k'}-x_k)|| + \frac{w_{\theta}}{\eta_{\theta}}|\theta_{i'} - \theta_{k'}|\right)\frac{H}{H + x_{k'}^y} + w_{area}|area_{i'} - area_{k'}|$$

with 
$$\eta_{\theta} = \arctan\left(\alpha_{\theta} \frac{\eta_{dist}}{||x_{k'} - x_k||}\right)$$

where  $w_{dist} = 1.0$ ,  $w_{\theta} = 0.1$ , and  $w_{area} = 0.1$  are weighting parameters,  $\eta_{dist} = \min(H, W)$  and  $\eta_{\theta}$ are normalization factors with H and W the height and width of the frame and  $\alpha_{\theta} = 0.1$  a secondary normalization factor. The  $\cdot^{y}$  operation returns the height component of a vector, and the  $\frac{H}{H+x_{k'}^{y}}$ term is useful to reduce the importance of the first terms if the axon k' is far from axon k in the height direction. This is needed as the scanning of the animal's cervical connective is done from top to bottom, thus we need to allow for some movement artifacts between the top and bottom of the image. Note that the dummy axons for unmatched regions are also added to this inner problem.

This inner assignment is solved for each possible pair of axon-ROI to get all final costs. The overall matching is then performed with them. Because we are embedding assignments, the computational cost of the tracker increases exponentially with the number of ROIs and axons. It stays tractable in our case as we generally deal with few axons at a time. All parameter values used in the matching were found empirically by trial and error.

Identities post-processing: ROI separation In the case of fine-tuning at the detection stage,
AxoID will also automatically try to divide ROIs that are potentially two or more separate axons.
We implement this to address the limitation introduced by detecting axons as a segmentation: close
or touching axons may get segmented together.

To do this, it first searches for potential ROIs to be separated by reusing the temporal average 845 of the similar frames used for the fine-tuning. This image is initially segmented as described before. 846 Then local intensity maxima are detected on a grayscale version of this image. To avoid small maxima 847 due to noise, we only keep those with an intensity  $\geq 0.05$ , assuming normalized grayscale values in 848 [0,1]. Following this, we use the watershed algorithm, with the scikit-image [84] implementation, to 849 segment the ROI based on the gray level and detected maxima. In the previous stages, we discarded 850 ROIs under 11 pixels to avoid small spurious detections. Similarly, here we fuse together adjacent 851 regions that are under 11 pixels to only output results after the watershedding above or equal to that 852 size. Finally, a border of 1 pixel width is inserted between regions created from the separation of an 853 ROI. 854

These borders are the divisions separating the ROI, referred to as "cuts". We parameterize each 855 of these as a line, defined as its normal vector  $\mathbf{n}$  and distance d to the origin of the image (top-left). 856 To report them on each frame, we first normalize this line to the current ROI, and then reverse that 857 process with respect to the corresponding regions on the other frames. To normalize the line to an ROI, 858 we fit an ellipse on the ROI contour in a least-square sense. Then the line parameters are transformed 859 into this ellipse's local coordinates following Algorithm 1. It is essentially like transforming the ellipse 860 into a unit circle, centered and axis-aligned, and applying a similar transformation to the cutting line 861 (Figure S11C, middle). The choice of fitting an ellipse is motivated by the visual aspect of the 862 axons in the experimental data as they are fairly similar to elongated ellipses. Considering this, a 863 separation between two close ellipses could be simplified to a linear border, motivating the linear 864 representation of the ROI separation. 865

Because this is done as a post-processing step following tracking, we can apply that division on all frames. To do this, we again fit an ellipse to their ROI contours in the least-squares sense. Then, we take the normalized cutting line and fit it back to each of them according to Algorithm 2. This is similar to transforming the normalized unit circle to the region ellipse and applying the same transform to the line (Figure S11C, right).

Algorithm 1: Normalize a line with an		Algorithm 2: Fit a line to an ellipse	
ellipse		Input: line, ellipse	
Input: line, ellipse		<b>Output:</b> fitted line <i>line</i> '	
<b>Output:</b> normalized line <i>line</i> '		<pre>/* Initialization</pre>	*/
<pre>/* Initialization</pre>	*/	$\mathbf{n} \leftarrow line.\mathbf{normal};$	
$\mathbf{n} \leftarrow line.\mathbf{normal};$		$d \leftarrow line.distance;$	
$d \leftarrow line.distance;$		$\mathbf{c} \leftarrow ellipse.\mathbf{center};$	
$\mathbf{c} \leftarrow ellipse.\mathbf{center};$		$w \leftarrow ellipse.width/2;$	
$w \leftarrow ellipse.width/2;$		$h \leftarrow ellipse.height/2;$	
$h \leftarrow ellipse.height/2;$		$\theta \leftarrow ellipse.rotation;$	
$\theta \leftarrow ellipse.rotation;$		$\mathbf{R}_{\theta} \coloneqq$ rotation matrix of angle $\theta$ ;	
$\mathbf{R}_{-\theta} \coloneqq$ rotation matrix of angle $-\theta$ ;		/* Fitting	*/
/* Normalization	*/	$\mathbf{n'} \leftarrow \mathbf{n};$	
$d' \leftarrow d - \mathbf{c} \cdot \mathbf{n};$		$\mathbf{n}'.x \leftarrow \mathbf{n}'.x * \mathbf{c}.y;$	
$\mathbf{n}' \leftarrow \mathbf{R}_{- heta}  \mathbf{n};$		$\mathbf{n}'.y \leftarrow \mathbf{n}'.y * \mathbf{c}.x;$	
$\mathbf{n}'.x \leftarrow \mathbf{n}'.x/\mathbf{c}.y;$		$d' \leftarrow d * (w * h);$	
$\mathbf{n}'.y \leftarrow \mathbf{n}'.y/\mathbf{c}.x;$		$d' \leftarrow d'/  \mathbf{n}'  ;$	
$d' \leftarrow d'/(w * h);$		$\mathbf{n'} \leftarrow \mathbf{n'}/  \mathbf{n'}  ;$	
$line'.distance \leftarrow d'/  \mathbf{n}'  ;$		$line'$ .normal $\leftarrow R_{\theta} \mathbf{n}';$	
$line'$ .normal $\leftarrow \mathbf{n'}/  \mathbf{n'}  ;$		$line'.distance \leftarrow d' + \mathbf{c} \cdot \mathbf{n}';$	

Finally, a new axon is defined for each cut. In each frame, the pixels of the divided region on the furthest side of the linear separation (with respect to the fitting ellipse center) are taken as the new ROI of that axon for that given frame.

In case there are multiple cuts of the same ROI (e.g., because three axons were close), the linear separations are ordered by distance to the center of the fitting ellipse and are then applied in succession. This is simple and efficient, but assumes there is little to no crossing between linear cuts.

#### 877 5.12.3 Fluorescence extraction

With the detection and tracking results, we know where each axon is in the experimental data. Therefore, to compute tdTomato and GCaMP fluorophore time-series we take the average of nonzero pixel intensities of the corresponding regions in each frame. We report the GCaMP fluorescence at time t as  $F_t$ , and the ratio of GCaMP to tdTomato fluorescence at time t as  $R_t$  to gain robustness against image intensity variations.

The final GCaMP fluorescence is reported as in [27]:

$$\Delta F/F = \frac{F_t - F}{F}$$

where F is a baseline fluorescence. Similarly, we report the ratio of GCaMP over tdTomato as in [27, 85]:

$$\Delta R/R = \frac{R_t - R}{R}$$

where R is the baseline. The baseline fluorescences F and R are computed as the minimal temporal average over windows of 10 s of the fluorophore time series  $F_t$  and  $R_t$ , respectively. Note that axons can be missing in some frames. For instance, if they were not detected or leave the image during movement artifacts. In this case, the fluorescence of that axon will have missing values at the time index t in which it was absent.

### <sup>893</sup> 5.13 Overall workflow

884

To improve the performance of AxoID, the fluorescence extraction pipeline is applied three times: once over the raw data, once over the data registered using cross-correlation, and once over the data registered using optic-flow warping. Note that the fine-tuning in the detection stage is not used with the raw experimental data as it is based on the cross-correlation between the frames and

would therefore lead to worse or redundant results with the data registered using cross-correlation. Eventually, the three fluorescence results can be visualized, chosen from, and corrected by a user through a GUI (Figure S11D).

### 901 5.13.1 Data registration

Registration of the experimental frames consists in transforming each image to make them similar to a reference image. The goal is to reduce the artifacts introduced by animal movements and to align axons across frames. This should help to improve the results of the detection and tracking.

Cross-correlation Cross-correlation registration consists of translating an image so that its correlation to a reference is maximized. Note that the translated image wraps-around (e.g., pixels disappearing to the left reappear on the right). This aims to align frames against translations, but is unable to counter rotations or local deformations. We used the single step Discrete Fourier Transform (DFT) algorithm [86] to find the optimal translation of the frame. It first transforms the images into the Fourier domain, computes an initial estimate of the optimal translation, and then refines this result using a DFT. We based our Python implementation on previous work [87].

For each experiment, the second frame is taken as the reference frame to avoid recording artifacts that sometimes appear on the first recorded image.

Optic-flow registration Optic flow-based registration was previously published [27]. Briefly, this approach computes an optic flow from the frame to a reference image, then deforms it by moving the pixels along that flow. The reference image is taken as the first frame of the experiment. This method has the advantage of being able to compute local deformations, but at a high computational cost.

# 919 5.13.2 AxoID GUI

Finally, AxoID contains a GUI where a user can visualize the results, select the best one, and manually correct it.

First, the user is presented with three outputs of the fluorescence extraction pipeline from the raw and registered data with the option of visualizing different information to select the one to keep and correct. Here, the detection and tracking outputs are shown, as well as other information like the fluorescence traces in  $\Delta F/F$  or  $\Delta R/R$ . One of the results is then selected and used throughout the rest of the pipeline.

Following this, the user can edit the tracker template, which will then automatically update the ROI identities across frames. The template and the identities for each frame are shown, with additional information like the image used to initialized the template. The user has access to different tools: axons can be fused, for example, if they actually correspond to a single real axon that was incorrectly detected as two, and, conversely, one axon can be manually separated in two if two close ones are detected together. Moreover, useless axons or wrong detections can be discarded.

Once the user is satisfied with the overall tracker, they can correct individual frames. At this stage, it is possible to edit the detection results by discarding, modifying, or adding ROIs onto the selected image. Then, the user may change the tracking results by manually correcting the identities of these ROIs. In the end, the final fluorescence traces are computed on the selected outputs including user corrections.

# 938 6 Supplementary Tables

No.	Gal4	Confocal SNR of smFP	2P SNR of OpGCaMP6f <sup>1</sup> and tdTomato	Number ROIs	ROI#	Encoding	Level synchronous activity (ROI# vs ROI#: Corr. coef.)	Redundan Gal4	t Supp. Video#
1	SS36131	strong	strong	2	0	rest	0 vs 1: 0.7	SS36132	3
		0			1 0	rest	0 vs 5: 0.4	SS36133	-
					1	rest rest	1 vs 5: 0.36		
9	SS38592	aturna		C	2	rest	2 vs 5: 0.49	SS38598	4
2	5536392	strong	strong	6	3	unclear		2220090	4
					4	unclear			
_					5	rest	0 vs 2: 0.85		
					1	unclear	0 VS 2. 0.85		
3	SS27485	strong	strong	4	2	rest		-	5
					3	rest			
4	SS41822	strong	strong	2	0	rest	0 vs 1: 0.71	SS41808 SS41809	6
					1 0	rest	0 vs 2: 0.84	5541809	
_					1	rest	0 vs 3: 0.79		_
5	SS38624	strong	strong	4	2	rest	1 vs 2: 0.9	-	7
					3	rest	1 vs 3: 0.87		
6	SS45605	strong	strong	1	0	unclear	-	-	8
					$     \begin{array}{c}       0 \\       1     \end{array} $	rest puff	0 vs 3: 0.91 0 vs 4: 0.84		
7	SS43652	strong	medium	5	2	rest	2  vs  3: 0.77	_	9
					3	rest	2 vs 4: 0.89		
					4	rest			
8	SS36112	strong	strong	2	0	puff	0 vs 1: 0.51	-	10
		-	-		1 0	puff unclear	2 vs 3: 0.67		
					1	unclear	2 13 5. 0.01		
9	SS41806	strong	strong	4	2	puff		-	11
					3	puff			
0	SS38631	strong	strong	2	0	off ball movement	0 vs 1: 0.88	-	12
_		0	0		1 0	off ball movement puff	0 vs 2: 0.32		
					1	puff	0 vs 2: 0.32 0 vs 3: 0.33		
11	SS51029	strong	medium	4	2	puff	1 vs 2: 0.37	SS51024	13
					3	puff	1 vs 3: 0.4		
					0	unresponsive	2 vs 4: 0.87		
					$\frac{1}{2}$	unresponsive walk			
$^{2}$	R85A11	strong	strong	6	3	unclear		-	15
					4	walk			
					5	unclear			
					0	unclear	0 vs 3: 0.38		
3	SS40489	_	strong	5	$\frac{1}{2}$	unclear unclear	0 vs 4: 0.43 1 vs 3: 0.53	_	16
.0	5540405		strong	0	3	unclear	1 vs 4: 0.53		10
					4	unclear			
					0	walk	0 vs 2: 0.61		
14	SS31480	strong	strong	3	$\frac{1}{2}$	unclear walk		-	17
					0	foreleg movement	0 vs 1: 0.69		
15	SS51021	strong	strong	2	1	foreleg movement	0 15 1. 0.00	-	18
6	SS51017	strong	strong	2	0	off ball movement	0 vs 1: 0.67	-	19
10	5551017	strong	strong	2	1	off ball movement		-	15
17	SS31456	strong	strong	2	0	off ball movement	0 vs 1: 0.20	-	20
			-		1 0	off ball movement walk	0 vs 1: 0.63		
18	SS46233	strong	medium	2	1	walk	0 15 1. 0.00	-	21
19	SS42749	strong	strong	2	0	push	0 vs 1: 0.89	-	22
10	5542145	Strong	strong	2	1	push	0 1 0 10	_	22
20	SS41815	strong	medium	2	$0 \\ 1$	unclear unclear	0 vs 1: 0.42	-	23
_					0	unclear	0 vs 1: 0.11		
21	SS29633	strong	strong	3	1	unclear	0 vs 2: 0.41	-	24
			, i i i i i i i i i i i i i i i i i i i		2	unclear	1 vs 2: 0.42		
22	R87H02	strong	strong	2	0	unclear	0 vs 1: 0.48	-	25
÷		0		2	1	unclear	0 10 10 0 22		
23	MAN	strong	strong	2	$     \begin{array}{c}       0 \\       1     \end{array} $	push push	0 vs 1: 0.82	-	26
					0	walk	0 vs 1: 0.54		
24	SS49172	strong	strong	3	1	walk	0 vs 2: 0.53	-	27
	_				2	walk	0 1		
25	R36G04	strong	strong	2	0	walk	0 vs 1: 0.55	-	28
		-			1	walk			

Table 1: Sparse AN driver lines and associated properties.

Jo Cald Confocal SNR OpGCaMP6f Number BOI# Encoding synchronous activity Redundant Supp				OD SND of			from previous pag	Level		
26       R.230.01       strong       strong       3       1       unclear       0       0       2       1.001       30         27       SS31219       strong       medium       2       1       1.001       0       31       30       30       30       30       30       30       30       31       1.001       1.022       .       31         28       R30A08       strong       strong       strong       strong       30       1.001       0       31       0.021       0.021       0.02       31       32         29       S841405       strong       strong       strong       strong       30       ss41105       0.021 <t< th=""><th>No.</th><th>Gal4</th><th></th><th>OpGCaMP6f</th><th>Number ROIs</th><th><sup>f</sup>ROI#</th><th>Encoding</th><th>(ROI# vs ROI#:</th><th></th><th>t Supp. Video#</th></t<>	No.	Gal4		OpGCaMP6f	Number ROIs	<sup>f</sup> ROI#	Encoding	(ROI# vs ROI#:		t Supp. Video#
$ \begin{array}{c c c c c c c c c c c c c c c c c c c $		Dec Ger								
$ \begin{array}{c ccccccccccccccccccccccccccccccccccc$	26	R39G01	strong	strong	3				-	29
27       SS1219       strong       strong       modium       2       walk       0 w 2: 0.74       .       30         28       R00.008       strong       modium       2       0       unclear       0 w 1: 0.32       .       31         29       SS44270       strong       strong       3       1       walk       0 w 1: 0.32       .       31         30       SS41005       strong       strong       strong       3       1       walk       0 w 2: 0.84       .       .       .31         31       SS20579       strong       strong       strong       2       0       turn       0 w 3: 0.87       . <td< td=""><td></td><td></td><td></td><td></td><td></td><td></td><td></td><td></td><td></td><td></td></td<>										
28       R30A08       strong       medium       2       0       unclear       0 vs 1: 0.22       .       31         29       S54427       strong       strong       3       walk       0 vs 1: 0.28       .       31         29       S541605       strong       strong       4       2       valk       0 vs 2: 0.34       .       33         31       S529579       strong       strong       2       1       unclear       2 vs 3: 0.04       .       .       31         31       S529579       strong       strong       2       1       unclear       2 vs 3: 0.04       . <td>27</td> <td>SS31219</td> <td>strong</td> <td>strong</td> <td>3</td> <td>1</td> <td>walk</td> <td></td> <td>-</td> <td>30</td>	27	SS31219	strong	strong	3	1	walk		-	30
$ \begin{array}{c c c c c c c c c c c c c c c c c c c $	20	D00400		1.	0			0 vs 1: 0.22		01
	28	R30A08	strong	medium	2				-	31
	20	9944970			2			0 vs 1: 0.98	5541605	20
30         SS 11605         strong         strong         4         1         unclear push strong         2 vs. 3: 0.94 push strong         SS 4270 a         33           31         SS 20570         strong         strong         6         a         a walk awalk         0 vs. 4: 0.84 awalk         0 vs. 4: 0.84 awalk         1 vs. 2: 0.78 awalk         a         a           32         SS 20503         strong         strong         2         0         turn         0 vs. 1: 0.48         .         35           33         SS 20803         strong         strong         2         0         turn         0 vs. 1: 0.48         .         35           34         SS 34574         strong         strong         3         1         forelog movement         0 vs. 1: 0.48         SS 20803         37           35         R70H06         strong         strong         2         0         forelog movement         0 vs. 1: 0.78         SS 42707         38           36         SS 42740         strong         strong         2         0         gr groom         0 vs. 1: 0.75         SS 23107         40           37         SS 23459         strong         strong         strong         strong         strong	29	5544270	strong	strong	5				5541005	32
30         551100         strong         strong         4         2         push sums (1)         554270         33           31         5529579         strong         strong         6         3         malk         0         vs.2         0.89           31         5529579         strong         strong         2         0         turn         0         vs.2         0.89           32         5551046         medium         strong         2         0         turn         0         vs.1         0.48         0.89         -         34           33         5529893         strong         strong         2         0         turn         0         vs.1         0.44         S524574         36           34         5854574         strong         strong         2         0         turn         0         vs.1         0.44         S529893         37           35         R70406         strong         strong         2         0         gregorm         0         vs.1         0.44         S524740         S52107         36           36         S542740         strong         strong         2         0         gregorom         0						0	unclear	2 vs 3: 0.94		
$ \begin{array}{c c c c c c c c c c c c c c c c c c c $	30	SS41605	strong	strong	4				SS44270	33
$ \begin{array}{c ccccccccccccccccccccccccccccccccccc$							· .			
31       S22579       strong       strong       6       2       walk uresponsive walk       1 w 2: 0.78 walk       -       34         22       S51046       medium       strong       2       0       turn       0 vs 1: 0.48       -       35         32       S529893       strong       strong       2       0       turn       0 vs 1: 0.44       S529893       37         34       S534574       strong       strong       2       0       turn       0 vs 1: 0.44       S529893       37         35       R70H06       strong       strong       2       0       forelog movement       0 vs 1: 0.47       S542707       38         36       S42740       strong       strong       2       0       forelog movement       0 vs 1: 0.47       S542707       39         37       S52469       strong       strong       2       0       forelog movement       0 vs 1: 0.48       S5342707       38         38       S53122       strong       strong       2       0       probosci sctension       0 vs 1: 0.37       S52106       40         39       S530303       strong       2       0       probosci sctension       0 vs 1: 0.34 <td></td> <td></td> <td></td> <td></td> <td></td> <td></td> <td></td> <td>0 vs 2: 0.84</td> <td></td> <td></td>								0 vs 2: 0.84		
11 S5295/9       strong       strong       0       3       walk       1 vs 3: 0.87       -       34         22 S551046       medium       strong       2       0       turn       0 vs 1: 0.48       -       35         33 S529893       strong       strong       2       0       turn       0 vs 1: 0.48       -       35         34 S529674       strong       strong       2       0       turn       0 vs 1: 0.44       S529893       37         35 R70106       strong       strong       2       0       forleg movement       0 vs 1: 0.98       S542707       38         36 S542740       strong       strong       2       0       forelg movement       0 vs 1: 0.97       R70400       39         37 S52469       strong       strong       strong       2       0       probosci sctension       0 vs 1: 0.81       S53207       40         38 S531232       strong       strong       2       0       probosci sctension       0 vs 1: 0.84       S531232       42         39 S53030       strong       strong       strong       1       probosci sctension       0 vs 1: 0.83       S531232       42         40 S52451       strong										
$ \begin{array}{c c c c c c c c c c c c c c c c c c c $	31	SS29579	strong	strong	6				-	34
								1 VS 5. 0.07		
22       Size 1046       medium       strong       2       1       turn										
$ \begin{array}{c c c c c c c c c c c c c c c c c c c $	32	SS51046	medium	strong	2			0 vs 1: 0.48	-	35
33       SS29893       strong       strong       4       1       unclear turn       SS34574       strong       36       SS4574       strong       37         34       SS34574       strong       strong       2       0       turn       0 vs 1: 0.44       SS29893       37         35       R70H06       strong       strong       3       1       foreleg movement foreleg movement       0 vs 1: 0.97       R70H06       SS2107       39         36       SS42740       strong       strong       2       0       foreleg movement foreleg movement       0 vs 1: 0.97       R70H06       SS2107       40         38       SS31232       strong       strong       2       0       proboscis extension 0 vs 1: 0.81       SS32030       41         39       SS30303       strong       2       0       proboscis extension 0 vs 2: 0.41       0.83       S321232       42         40       SS2451       strong       strong       7       3       proboscis extension 0 unresponsive       vs 1: 0.83       S331232       43         41       SS2566       strong       strong       6       0       unresponsive       vs 2: 0.41       vs 3: 0.65       1       vs 4: 0.61								2 vs 3. 0.62		
$ \begin{array}{c ccccccccccccccccccccccccccccccccccc$	~~							2 18 5. 0.02	GGOVEEN	0.0
$ \begin{array}{c ccccccccccccccccccccccccccccccccccc$	33	SS29893	strong	strong	4		turn		SS34574	36
34 S534914       strong       strong       2       1       turn       55 25983       37         35 R70H06       strong       strong       3       1       foreleg movement       0 vs.1: 0.98       S542740       38         36 S842740       strong       strong       2       0       foreleg movement       0 vs.1: 0.97       R70H06       39         37 S25469       strong       strong       2       0       eye groom       0 vs.1: 0.75       S552107       40         38 S31232       strong       strong       2       0       proboscia extension       0 vs.1: 0.81       S5825451       41         39 S33033       strong       2       0       proboscia extension       0 vs.1: 0.89       S531232       42         40 S525451       strong       strong       7       3       unresponsive       S531232       43         41 S528596       strong       strong       strong       7       3       unresponsive       S331232       43         41 S528596       strong       strong       strong       2       proboscia extension       0 vs.2: 0.4       1       1       1       1       1       1       1       1       1       1								0 1 0 11		
	34	SS34574	strong	strong	2			0 VS 1: 0.44	SS29893	37
								0 vs 1: 0.98	8849740	
$ \begin{array}{c ccccccccccccccccccccccccccccccccccc$	35	R70H06	strong	strong	3					38
30       SS1240       strong       strong       2       1       foreleg movement       SS2470       S9         37       SS25469       strong       strong       2       0       rever groom       0 vs 1: 0.75       SS2106       40         38       SS31232       strong       strong       2       0       proboscis extension       0 vs 1: 0.81       SS2303       41         30       SS30303       strong       2       0       proboscis extension       0 vs 1: 0.81       SS25451       41         30       SS25451       strong       strong       7       3       0       unresponsive       2 vs 4: 0.33       unresponsive       SS31232       42         40       SS25451       strong       strong       7       3       intersponsive       SS31232       43         41       SS28596       strong       strong       foreleg movement       0 vs 3: 0.65       foreleg movement       0 vs 3: 0.65       foreleg movement       0 vs 3: 0.4       intersponsive       44       intersponsive       intersponsive       45       56       foreleg movement       0 vs 3: 0.65       intersponsive       intersponsive       1 vs 4: 0.61       intersponsive       1 vs 4: 0.61       intersponsive </td <td></td> <td></td> <td></td> <td></td> <td></td> <td></td> <td></td> <td>0 = 1, 0.07</td> <td></td> <td></td>								0 = 1, 0.07		
37       SS25469       strong       strong       2       0       eve groom       0 vs 1: 0.75       SS52106       40         38       SS1232       strong       strong       2       0       proboscis extension       0 vs 1: 0.81       SS52037       41         39       SS30303       strong       2       0       proboscis extension       0 vs 1: 0.81       SS52142       42         40       SS25451       strong       2       ourresponsive       2 vs 4: 0.93       SS30303       43         40       SS25451       strong       strong       7       3       unresponsive       2 vs 4: 0.93       SS30303       43         41       SS25455       unresponsive       2 vs 4: 0.93       strong       SS31232       43         41       SS25456       strong       strong       7       3       unresponsive       0 vs 2: 0.4       SS30303       43         41       SS25456       strong       strong       et al.       1       foreleg movement       0 vs 2: 0.4       6       44       1       strong       1       strong       1 vs 3: 0.5       1 vs 4: 0.46       1 vs 5: 0.28	36	SS42740	strong	strong	2			0 VS 1. 0.97		39
1 $v_{ev}$ groom       SS22107         38       SS31232       strong       2       0       proboscis extension       0       vs 1: 0.81       SS2303       41         39       SS30303       strong       2       0       proboscis extension       0       vs 1: 0.89       SS23123       42         40       SS25451       strong       strong       7       3       proboscis extension       vs 1: 0.89       SS31232       43         41       SS25451       strong       strong       7       3       proboscis extension       vs 1: 0.89       SS31232       43         40       SS25451       strong       strong       7       3       proboscis extension       vs 2: 0.4       5331232       43         41       SS25596       strong       strong       6       4       foreleg movement       0 vs 2: 0.4       0 vs 1: 0.31       strong       44         41       SS25596       strong       strong       2       0       unclear       0 vs 1: 0.21       strong       -       45         42       SS40134       strong       medium       2       0       unclear       0 vs 1: 0.21       -       45         42	37	\$\$25460	strong	strong	2			0 vs 1: 0.75		40
38       SS31232       strong       2       1       proboscis extension       SS2131       41         39       SS30303       strong       2       0       proboscis extension       0 vs 1: 0.89       SS31232       42         40       SS25451       strong       strong       7       3       0       unresponsive       2 vs 4: 0.93       2       2 proboscis extension       SS31232       43         40       SS25451       strong       strong       7       3       0       unresponsive       2 vs 4: 0.93       3       33         41       SS25451       strong       strong       7       3       1       unresponsive       2 vs 4: 0.93       3       33         41       SS25451       strong       strong       7       3       1       unresponsive       3       30       33	57	5525405	strong	strong	2			0 1 0 01		40
$\begin{array}{c ccccccccccccccccccccccccccccccccccc$	38	SS31232	strong	strong	2			0 vs 1: 0.81		41
$ \begin{array}{c ccccccccccccccccccccccccccccccccccc$	00	000000		,	0			0 vs 1: 0.89		10
	39	5530303		strong	2		*		SS25451	42
$ \begin{array}{cccccccccccccccccccccccccccccccccccc$								2 vs 4: 0.93		
									6601000	
$4 \ \text{probacits extension} \\ 5 \ \text{unresponsive} \\ 6 \ \text{unresponsive} \\ 1 \ \text{foreleg movement}  0 \text{ vs } 2: 0.4 \\ 1 \ \text{foreleg movement}  0 \text{ vs } 3: 0.65 \\ 2 \ \text{foreleg movement}  0 \text{ vs } 3: 0.65 \\ 2 \ \text{foreleg movement}  0 \text{ vs } 2: 0.52 \\ 1 \ \text{vs } 1 \text{ vs } 2: 0.52 \\ 1 \ \text{vs } 2: 0.28 \\ 1 \ \text{vs } 2: 0.21 \\ 2 \ \text{unclear} \\ 1 \ \text{vs } 2: 0.07 \\ 2 \ \text{unclear} \\ 1 \ \text{vs } 2: 0.07 \\ 1 \ \text{vs } 1: 0.21 \\ 2 \ \text{unclear} \\ 1 \ \text{vs } 2: 0.07 \\ 2 \ \text{unclear} \\ 1 \ \text{vs } 2: 0.07 \\ 1 \ \text{vs } 1: 0.34 \\ 2 \ \text{unclear} \\ 1 \ \text{unclear} \\ 1 \ \text{vs } 2: 0.02 \\ 1 \ \text{unclear} \\ 2 \ \text{vs } 1: 0.21 \\ 2 \ \text{unclear} \\ 1 \ \text{vs } 2: 0.02 \\ 1 \ \text{unclear} \\ 2 \ \text{vs } 1: 0.43 \\ 2 \ \text{unclear} \\ 1 \ \text{unclear} \\ 2 \ \text{vs } 1: 0.43 \\ 2 \ \text{unclear} \\ 2 \ \text{vs } 1: 0.43 \\ 2 \ \text{unclear} \\ 2 \ \text{vs } 1: 0.43 \\ 2 \ \text{unclear} \\ 2 \ \text{vs } 1: 0.43 \\ 2 \ \text{unclear} \\ 2 \ \text{vs } 1: 0.43 \\ 2 \ \text{unclear} \\ 2 \ \text{vs } 1: 0.43 \\ 2 \ \text{unclear} \\ 2 \ \text{vs } 1: 0.43 \\ 2 \ \text{unclear} \\ 2 \ \text{vs } 1: 0.43 \\ 2 \ \text{unclear} \\ 2 \ \text{vs } 1: 0.43 \\ 2 \ \text{unclear} \\ 2 \ \text{vs } 1: 0.43 \\ 2 \ \text{unclear} \\ 2 \ \text{vs } 1: 0.43 \\ 2 \ \text{unclear} \\ 2 \ \text{vs } 1: 0.43 \\ 2 \ \text{unclear} \\ 2 \ \text{vs } 1: 0.43 \\ 2 \ \text{vs } 1: 0.74 \\ 2 \ \text{vs } 1: 0.74 \\ 3 \ \text{unclear} \\ 2 \ \text{vs } 1: 0.75 \\ 3 \ \text{unclear} \\ 2 \ \text{vs } 1: 0.75 \\ 3 \ \text{vs } 1: 0.75 \\ 3 \ \text{vs } 1: 0.75 \\ 3 \ \text{vs } 1: 0.75 \\ 4 \ \text{puff} \\ 5 \ \text{rest} \\ 4 \ \text{puff} \\ 5 \ \text{rest} \\ 4 \ \text{vs } 1: 0.74 \\ 4 \ \text{vs } $	40	SS25451	strong	strong	7		*			43
$ \begin{array}{cccccccccccccccccccccccccccccccccccc$							*		5550505	
$\begin{array}{c ccccccccccccccccccccccccccccccccccc$							•			
$\begin{array}{cccccccccccccccccccccccccccccccccccc$								0 vs 2: 0.4		
$\begin{array}{cccccccccccccccccccccccccccccccccccc$										
$\begin{array}{cccccccccccccccccccccccccccccccccccc$							0			
	41	SS28596	strong	strong	6				R86H08	44
$\begin{array}{c ccccccccccccccccccccccccccccccccccc$										
$\begin{array}{cccccccccccccccccccccccccccccccccccc$										
$\begin{array}{cccccccccccccccccccccccccccccccccccc$						0	unclear			
$\begin{array}{cccccccccccccccccccccccccccccccccccc$	42	SS40134	strong	medium	2			0 0.0	-	45
$\begin{array}{cccccccccccccccccccccccccccccccccccc$	43	SS29621	strong	strong	2			0 vs 1: 0.74	-	46
$\begin{array}{cccccccccccccccccccccccccccccccccccc$								$0 \text{ vs} 1 \cdot 0.21$		
$\begin{array}{cccccccccccccccccccccccccccccccccccc$	44	R69H10	strong	strong	3				-	47
$\begin{array}{cccccccccccccccccccccccccccccccccccc$				<u> </u>		2	unclear	1 vs 2: 0.02		
$ \begin{array}{c ccccccccccccccccccccccccccccccccccc$										
$\begin{array}{c ccccccccccccccccccccccccccccccccccc$	45	SS51038	strong	strong	5				_	48
$\begin{array}{cccccccccccccccccccccccccccccccccccc$						3				
$\begin{array}{cccccccccccccccccccccccccccccccccccc$								0 0 - 0 70		
$ \begin{array}{cccccccccccccccccccccccccccccccccccc$								0 vs 2: 0.53		
$\begin{array}{c ccccccccccccccccccccccccccccccccccc$	46	SS42008	strong	strong	4				SS42007	
$\begin{array}{c ccccccccccccccccccccccccccccccccccc$						3	unclear			
$\begin{array}{cccccccccccccccccccccccccccccccccccc$										
$\begin{array}{cccccccccccccccccccccccccccccccccccc$		aace								
4         puff           5         rest           48 \$\$540619         medium           48 \$\$540619         walk           0         walk           0         vs 1: 0.74	47	SS36118	strong	strong	6				-	50
48 SS40619 medium strong 2 0 walk 0 vs 1: 0.74							puff			
								$0 \ge 1 \cdot 0.74$		
	48	SS40619	medium	strong	2			0 v8 1. 0.74	-	51

No.         Gala         Control with and all all and all all all all all all all all all al							from previous pa	Level		
9         S845363         strong         4         1         puff unclear puff         1 vs 3: 0.85 unclear         .           5         S552147         medium         medium         10         - </th <th>ю.</th> <th>Gal4</th> <th></th> <th></th> <th>Numbe ROIs</th> <th><sup>r</sup>ROI#</th> <th>Encoding</th> <th>synchronous activity (ROI# vs ROI#:</th> <th></th> <th>; Supp. Video≢</th>	ю.	Gal4			Numbe ROIs	<sup>r</sup> ROI#	Encoding	synchronous activity (ROI# vs ROI#:		; Supp. Video≢
39         Second         atrong atrong         atrong atrong										
U         U         J         pulf         0 vs 1: 0.32         0.32           1         1         pulf         0 vs 1: 0.32         -           1         1         1         1         1         1         1           1         1         1         1         1         1         1         1           3         SS2470         strong         3         -         1	19	SS45363	strong	strong	4				-	52
90       8532147       medium       2       0       pulf       0 vs 1: 0.32       -         10       R38709       -       strong       10       -       muresponsive       -       -         20       Statog       strong       10       -       muresponsive       -       -       -         20       Statog       strong       0       -       muresponsive       -       -       -         20       Statog       strong       0       -       muresponsive       -       -       -         20       Statog       strong       10       -       muresponsive       -       -       -         20       Statog       strong       strong       -       muresponsive       -       -       -       -         20       Statog       medium       attog       -       muresponsive       -								2 13 0. 0.11		
10         10         1         muresponsive unresponsive         -           25         SS4-200         strong         strong         -         -           25         SS4-200         strong         -         -         -           26         SS3-200         strong         strong         -         -         -           25         SS4-200         strong         strong         -         -         -           25         SS4-200         strong         strong         -	50	8852147	modium	modium	2		*	$0 \ge 1 \cdot 0.32$		53
25       Stricken       strong       strong       5       -       unresponsive       -       St84400         55       SS25473       strong       strong       5       -       unresponsive       -       -         56       SS25474       strong       strong       strong       -       -       -       -         56       SS25492       strong       strong       strong       - <t< td=""><td></td><td></td><td>medium</td><td>medium</td><td></td><td>1</td><td>puff</td><td>0 VS 1: 0.32</td><td>-</td><td>55</td></t<>			medium	medium		1	puff	0 VS 1: 0.32	-	55
53       S52470       strong       strong       5       -       unresponsive       -       -         55       S52372       strong       strong       1       -       -       -         56       S52374       strong       strong       strong       2       -       unresponsive       -       -         57       S52382       strong       strong       strong       strong       -       -         58       S53333       strong       strong       attrong       -       -       -         68       S53363       strong       strong       attrong       -       -       -         68       S53364       strong       strong       attrong       -       -       -         68       S53004       strong       strong       - <td< td=""><td></td><td></td><td>-</td><td></td><td></td><td></td><td></td><td>-</td><td>-</td><td>-</td></td<>			-					-	-	-
54       S124/78       strong       strong       image: strong <td></td> <td></td> <td></td> <td></td> <td></td> <td></td> <td>-</td> <td></td> <td>-</td> <td>-</td>							-		-	-
55       SS2852       strong			0				* ·			-
57       SS11890       strong       strong       7       -       -         58       SS1333       strong       strong       7       -       -         58       SS1333       strong       strong       6       -       -       -         58       SS1333       strong       strong       6       -       urresponsive       -       -         58       SS1340       strong       strong       -       urresponsive       -       -         61       SS146100       strong       strong       2       -       urresponsive       -       -         66       SS145400       strong       strong       2       -       urresponsive       -       -       -         66       SS14500       strong       medium       1       -       urresponsive       -						-	*	-	-	-
58       S3330       strong       strong       2       -       -       -         60       S33343       strong       strong       3       -       uuresponsive       -       -         60       S33430       strong       strong       3       -       uuresponsive       -       -         61       S33480       modium       medium       - </td <td>56</td> <td>SS29574</td> <td>strong</td> <td>strong</td> <td></td> <td>-</td> <td>unresponsive</td> <td>-</td> <td>-</td> <td>-</td>	56	SS29574	strong	strong		-	unresponsive	-	-	-
90       SS3433       strong       strong       0       -       -       -         00       SS38012       strong       strong       3       -       uuresponsive       -       -         01       SS3805       medium       strong       3       -       uuresponsive       -       -         02       SS3805       strong       strong       3       -       uuresponsive       -       -         03       SS40200       medium       medium       2       -       uuresponsive       -       SS2470         04       SS4300       strong       atoma       -       uuresponsive       -       SS2470         05       SS0004       strong       atoma       -       uuresponsive       -       -       SS3613         71       SS36133       strong       -       -       not imaged       -       SS3613         72       SS4180       strong       -       -       not imaged       -       SS3613         73       SS4180       strong       -       -       not imaged       -       SS41820         75       SS41800       strong       -       -       not imaged <td></td> <td></td> <td></td> <td></td> <td></td> <td></td> <td></td> <td>-</td> <td></td> <td>-</td>								-		-
60       SS383012       strong       strong       3       -       unresponsive       -       -         62       SS38430       medium       medium       2       -       unresponsive       -       -         63       SS48420       medium       2       -       unresponsive       -       -         64       SS48400       strong       medium       2       -       unresponsive       -       -         65       SS48400       strong       medium       4       -       unresponsive       -       -       -         65       SS4004       strong       medium       3       -       unresponsive       -       -       -       -       SS4632       -							*			-
61       SS38386       medium       strong       3       -       unresponsive       -       -         62       SS3867       strong       strong       3       -       unresponsive       -       -         63       SS46020       medium       2       -       unresponsive       -       SS3667         65       SS48400       strong       strong       2       -       unresponsive       -       SS3667         65       SS45400       strong       strong       2       -       unresponsive       -       -         65       SS500013       medium       4       -       unresponsive       -										-
63       Stackagen       medium       2       -       uuresponsive       -       -         65       Stakatoo       strong       strong       5       -       uuresponsive       -       Stakatoo         65       Stakatoo       strong       g       -       uuresponsive       -       Stakatoo         66       Stakatoo       strong       g       -       uuresponsive       -       -         66       Stakatoo       strong       medium       4       -       uuresponsive       -       -         68       Statouto       strong       medium       3       -       uuresponsive       -				<u>v</u>				-	-	-
64       Statistic medium       2       -       unresponsive       -       -       -         65       Statistic minimum       1       -       unresponsive       -       SStatistic minimum       -       SStatistic minimum       -       -       SStatistic minimum       -       -       SStatistic minimum       - </td <td></td> <td></td> <td>strong</td> <td></td> <td></td> <td>-</td> <td>unresponsive</td> <td>-</td> <td>-</td> <td>-</td>			strong			-	unresponsive	-	-	-
65       SS48406       strong       strong       2       -       SS2470         66       SS49092       strong       medium       4       -       uuresponsive       -       -         67       SS30013       strong       medium       1       -       uuresponsive       -       -         68       SS50013       medium       nedium       1       -       uuresponsive       -       -         70       SS3052       strong       medium       1       -       uuresponsive       - <td></td> <td></td> <td></td> <td></td> <td></td> <td></td> <td></td> <td>-</td> <td>-</td> <td>-</td>								-	-	-
66       S14400       strong       medium       4       urresponsive       -       -         68       S50004       strong       nedium       1       urresponsive       -       -         68       S50013       medium       a       urresponsive       -       <			0				*			-
67       S49982       strong			0							-
68       S53004       strong       strong       2       -       unresponsive       -       -         70       S53052       strong       medium       3       -       unresponsive       -       -         71       S53052       strong       medium       3       -       unresponsive       -       -       -         71       S53052       strong       -       -       -       unresponsive       -<				<u>v</u>		-	*	-	-	-
70       SS0652       strong       medium       3       -       utresponsive       -       -         71       SS06132       strong       -       -       -       0 timaged       -       SS36131         72       SS36133       strong       -       -       -       -       0 tot imaged       -       SS36133         73       SS36598       strong       -       -       -       -       0 tot imaged       -       SS36137         74       SS41808       strong       -       -       -       not imaged       -       SS41820         75       SS41809       strong       -       -       -       not imaged       -       SS41820         76       SS41820       strong       -       -       -       not imaged       -       SS41820         76       SS41820       strong       -       -       not imaged       -       SS41820         78       SS42007       strong       -       -       not imaged       -       SS41820         78       SS42007       strong       -       -       not imaged       -       SS4200         78       SS42007 <td< td=""><td></td><td></td><td></td><td></td><td></td><td>-</td><td></td><td>-</td><td>-</td><td>-</td></td<>						-		-	-	-
71       SS36132       strong       -       -       redundant)       -       SS36133         72       SS36133       strong       -       -       redundant)       -       SS36133         73       SS38598       strong       -       -       redundant)       -       SS36132         74       SS41809       strong       -       -       not imaged       SS41820         75       SS41809       strong       -       -       not imaged       SS41820         76       SS41820       strong       -       -       not imaged       SS41820         76       SS41820       strong       -       -       not imaged       SS41820         77       SS41820       strong       -       -       not imaged       SS41820         77       SS41820       strong       -       -       not imaged       SS41820         78       SS42007       strong       -       -       not imaged       SS41820         79       SS42707       medium       -       -       not imaged       SS4200         79       SS42007       strong       -       -       incedundant)       SS42080			medium	medium		-	unresponsive	-	-	-
11       S30132       strong       -       -       (redundant)       -       S330133         21       S30133       strong       -       -       -       not imaged       -       S330131         73       S33508       strong       -       -       -       mot imaged       -       S330132         74       S541808       strong       -       -       -       not imaged       -       S33132         74       S541809       strong       -       -       -       not imaged       -       S41809         75       S541809       strong       -       -       -       not imaged       -       S41820       S41820         76       S541820       strong       -       -       -       not imaged       -       S41820       S418	70	SS50652	strong	medium	3	-	*	-	-	-
72       SS36133       strong       -       -       not imaged (redundant)       -       SS36132         73       SS38598       strong       -       -       0       not imaged (redundant)       -       SS36592         74       SS41808       strong       -       -       not imaged (redundant)       -       SS41820 SS41820         75       SS41809       strong       -       -       -       not imaged (redundant)       -       SS41820 SS41820         76       SS41820       strong       -       -       -       not imaged (redundant)       -       SS41820 SS41820         77       SS41821       strong       -       -       -       not imaged (redundant)       -       SS41820 SS41820         78       SS42007       strong       -       -       -       not imaged (redundant)       -       SS42700 SS41820         78       SS42007       strong       -       -       -       not imaged (redundant)       -       SS42700 SS41820         80       SS43528       strong       weak       -       -       (undetectable in 2P; (redundant)       -       SS42002         81       S48632       medium       -       -	71	SS36132	strong	-	-	-		-		-
12       SS30133       strong       -       -       (redundant)       -       SS30132         73       SS3598       strong       -       -       not imaged (redundant)       -       SS36592         74       SS41808       strong       -       -       not imaged (redundant)       -       SS36592         74       SS41809       strong       -       -       not imaged (redundant)       -       SS41820         75       SS41820       strong       -       -       not imaged (redundant)       -       SS41820         76       SS41820       strong       -       -       not imaged (redundant)       -       SS41820         78       SS41820       strong       -       -       not imaged (redundant)       -       SS41820         78       SS41821       strong       -       -       not imaged (redundant)       -       SS41820         78       SS41820       strong       -       -       not imaged (redundant)       -       SS41820         78       SS42070       strong       -       -       not imaged (redundant)       -       SS42008         79       SS42004       strong       -       -										
73       SS38598       strong       -       -       not imaged (redundant)       SS38592         74       SS41808       strong       -       -       -       not imaged (redundant)       -       SS41820 SS41820         75       SS41809       strong       -       -       -       not imaged (redundant)       -       SS41820 SS41820         76       SS41820       strong       -       -       -       not imaged (redundant)       -       SS41820 SS41821         77       SS41821       strong       -       -       -       not imaged (redundant)       -       SS41820 SS41821         78       SS42007       strong       -       -       -       not imaged (redundant)       -       SS41820 SS41820         78       SS42007       strong       -       -       -       not imaged (redundant)       -       SS42008         78       SS42007       medium       -       -       -       -       0       S42740         80       SS42767       medium       -       -       -       -       S54208         81       SS42007       medium       -       -       -       -       S54204 <t< td=""><td>72</td><td>SS36133</td><td>strong</td><td>-</td><td>-</td><td>-</td><td></td><td>-</td><td></td><td>-</td></t<>	72	SS36133	strong	-	-	-		-		-
74       SS41808       strong       -       -       -       (redundant)       SS41820         75       SS41809       strong       -       -       -       not imaged (redundant)       SS41820         75       SS41820       strong       -       -       -       not imaged (redundant)       SS41821         76       SS41820       strong       -       -       -       not imaged (redundant)       SS41821         76       SS41820       strong       -       -       -       not imaged (redundant)       SS41821         76       SS41820       strong       -       -       -       not imaged (redundant)       SS41820         78       SS41821       strong       -       -       -       not imaged (redundant)       SS41820         78       SS42007       strong       -       -       -       not imaged (redundant)       SS41800         78       SS42007       strong       -       -       -       not imaged (redundant)       SS41802         80       SS43528       strong       weak       -       -       (redundant)       SS42008         81       SS46802       medium       -       -	79	9930500	atuana							
74       S \$41808       strong       -       -       -       not imaged (redundant)       S \$41800       S \$41800         75       \$ \$511809       strong       -       -       not imaged (redundant)       S \$41820       S \$41820         76       \$ \$541820       strong       -       -       not imaged (redundant)       S \$41820       S \$41820         77       \$ \$541820       strong       -       -       not imaged (redundant)       S \$41820       S \$41820         78       \$ \$541820       strong       -       -       not imaged (redundant)       S \$41820       S \$41820         78       \$ \$541821       strong       -       -       not imaged (redundant)       S \$41820       S \$41820         78       \$ \$54207       strong       -       -       not imaged (redundant)       S \$41800       S \$41800         79       \$ \$54207       medium       -       -       not imaged (redundant)       S \$41800       S \$41800         81       \$ \$54207       medium       -       -       0.01 imaged (redundant)       S \$42740         81       \$ \$54208       strong       weak       -       -       1001 imaged (redundant)       S \$52106       S \$5210	3	2230930	strong	-	-	-	(redundant)	-		-
14       SS41808       strong       -       -       -       (redundant)       -       SS41820         75       SS41809       strong       -       -       -       not imaged (redundant)       -       SS41821         76       SS41820       strong       -       -       -       not imaged (redundant)       -       SS41820         76       SS41820       strong       -       -       -       not imaged (redundant)       -       SS41820         77       SS41820       strong       -       -       -       not imaged (redundant)       -       SS41820         78       SS42007       strong       -       -       -       not imaged (redundant)       -       SS42008         78       SS42007       strong       -       -       -       not imaged (redundant)       -       SS42008         79       SS42007       medium       -       -       -       not imaged (redundant)       -       SS42008         80       SS43528       strong       weak       -       -       (undetectable in 2P; redundant)       -       SS428409         81       SS5102       medium       -       -       not imaged (redun										
Set 1820 Set 1820 Set 1000 Set 1820Set 1820 Set 1820 Set 1000 Set 1820 Set 1820Set 1820 Set 1820 Set 1820 Set 1820 Set 1820Set 1820 Set 1820 Set 1820 Set 182077SS41821 SS41821 SS4107strongnot imaged (redundant)-SS41820 SS41821 SS4182078SS41821 SS42007 SS42007 Strongnot imaged (redundant)-SS41820 SS4182078SS42007 SS42007 SS42007 SS42007 SS42007 SS42007 SS42007Not imaged (redundant)-SS42004 SS4200778SS42007 SS42007 SS42007 SS42007 SS42007 SS42007Not imaged (redundant)-SS42004 SS4200479SS42007 SS42007 SS42007 SS42007 SS42007 SS42007Not imaged (redundant)-SS42007 SS4200480SS43528 Strong SS52108 SS52108 SS52108 SS52108 SS52108 SS52106Not imaged (redundant)-SS52109 SS52108 SS52108 SS52108 SS52108 SS52108 SS52108 SS52107Not imaged (redundant)-SS52107 SS52108 SS5210886SS52106 SS52106 SS52106 SS52108 SS52108 SS52108 SS52108 SS52108 SS52108 SS52108 SS52108 SS52108 SS52108 SS52108 SS52108 SS52108 SS52108 SS52108 SS52108 SS52109Not imaged (	74	SS41808	strong	-	-	-		-		-
75SS41809strongnot imaged (redundant)SS41820 SS4182176SS41820strongnot imaged (redundant)SS41821 SS4182177SS41821strongnot imaged (redundant)SS41821 SS4182178SS42007strongnot imaged (redundant)SS41820 SS4182178SS42007strongnot imaged (redundant)SS41820 SS4182078SS42007strongnot imaged (redundant)SS42008 SS4182079SS42707mediumnot imaged (redundant)SS4200879SS42707mediumnot imaged (redundant)SS4200880SS43528strongweak(undetectable in 2P; redundant)-SS4840981SS48632mediumnot imaged (redundant)SS5210282SS5104strongweaknot imaged (redundant)SS5210283SS52108strongweaknot imaged (redundant)SS5210884SS52106mediumnot imaged (redundant)SS5210885SS52107mediumnot imaged (redundant)SS5210886SS6108mediumnot imaged (redundant)SS521088							(redundant)			
15       SS41809       strong       -       -       -       (redundant)       -       SS41820 SS41821         76       SS41820       strong       -       -       -       not imaged (redundant)       -       SS41821 SS41829         77       SS41821       strong       -       -       not imaged (redundant)       -       SS41820 SS41829         78       SS42007       strong       -       -       not imaged (redundant)       -       SS42008         78       SS42007       strong       -       -       not imaged (redundant)       -       SS42008         78       SS42007       strong       -       -       not imaged (redundant)       -       SS42008         79       SS42007       medium       -       -       -       not imaged not imaged       -       SS42008         80       SS43528       strong       weak       -       -       (medundant)       -       SS4809         81       SS48632       medium       -       -       (redundant)       -       SS51029         82       SS51024       strong       -       -       not imaged (redundant)       -       SS52109         84       <										
reductionStatisticStatistic76SS41820strongnot imaged (redundant)Statistic77SS41821strongnot imaged (redundant)Statistic78SS42007strongnot imaged (redundant)Statistic79SS42007strongnot imaged (redundant)Statistic79SS42007mediumnot imaged (redundant)Statistic79SS42707mediumnot imaged (redundant)Statistic80SS43528strongweak(undetectable in 2P; (redundant))-Statistic81SS46632mediumnot imaged (redundant)-Statistic82SS51024strongweaknot imaged (redundant)-Statistic83SS52108strongweaknot imaged (redundant)-Statistic84SS52106mediumnot imaged (redundant)-Statistic85SS52107mediumnot imaged (redundant)-Statistic86Rs6H08mediumweaknot imaged (redundant)-Statistic87S2529890indistinguishable brain neurons)not image	75	55/1800	strong				not imaged		SS41808	
76SS41820strongnot imaged (redundant)SS41820 SS41803 SS41809 SS4182177SS41821strongnot imaged (redundant)SS41820 SS4182078SS42007strongnot imaged (redundant)SS42000 SS4182078SS42007strongnot imaged (redundant)SS42000 SS4182079SS42707mediumnot imaged (redundant)SS42740 ROHMER79SS42528strongweak(mediumated) (redundant)SS42740 ROHMER80SS43528strongweak0SS42740 (redundant)ROHMER81SS48632medium0SS42740 (redundant)ROHMER82SS51024strong0SS52102 (redundant)SS52102 SS5210683SS52108strongweak0SS52102 (redundant)SS52106 SS5210684SS52106mediumnot imaged (redundant)SS52108 	5	5541609	strong	-	-	-	(redundant)	-		-
76SS 41820strongnot imaged (redundant)SS 41809 SS 41809 SS 4182077SS 41821strongnot imaged (redundant)SS 41808 SS 41809 SS 4180978SS 42007strongnot imaged (redundant)SS 42008 SS 4180979SS 42007mediumnot imaged (redundant)SS 42008 SS 4180979SS 42007mediumnot imaged (redundant)SS 42008 SS 4180980SS 43528strongweaknot imaged (redundant)SS 480981SS 48632mediummot imaged (redundant)SS 4840982SS 51024strongnot imaged (redundant)SS 52102983SS 52108strongweaknot imaged (redundant)SS 52106 SS 5210784SS 52106mediumnot imaged (redundant)SS 52108 SS 5210685SS 52107mediumnot imaged (redundant)SS 52108 SS 5210886R86H08mediumweaknot imaged (redundant)SS 52108 SS 5210887SS 529890 (indistinguishable brain neurons)not imaged (redundant)SS 52108 SS 5210888SS 529890 (indistinguishable brain neurons)not imaged <br< td=""><td></td><td></td><td></td><td></td><td></td><td></td><td></td><td></td><td></td><td></td></br<>										
76       SS41820       strong       -       -       -       (redundant)       -       SS41809         77       SS41821       strong       -       -       not imaged (redundant)       -       SS41809         78       SS42007       strong       -       -       not imaged (redundant)       -       SS42008         78       SS42007       strong       -       -       not imaged (redundant)       -       SS42000         80       SS43528       strong       weak       -       -       not imaged (redundant)       -       SS42009         81       SS48632       medium       -       -       (undetectable in 2P; redundant)       -       SS48409         82       SS51024       strong       -       -       not imaged (redundant)       -       SS52109         83       SS52108       strong       weak       -       -       not imaged (redundant)       -       SS52109         84       SS52106       medium       -       -       -       not imaged (redundant)       -       SS52106         85       SS52107       medium       -       -       -       not imaged (redundant)       -       SS52106      <							not imaged			
S41821 S41821strongnot imaged (redundant)S541821 S54182078S542007strongnot imaged (redundant)-S54200879S542707mediumnot imaged (redundant)-S54274079S542707mediumnot imaged (redundant)-S54274080S543528strongweak(undetectable in 2P; redundant)-S53801281S548632medium(undetectable in 2P; redundant)-S53801282S551024strongweaknot imaged (redundant)-S55210983S552108strongweaknot imaged (redundant)-S55210784S552106mediumnot imaged (redundant)S55210785S552107mediumnot imaged (redundant)S55210886R86H08mediumweaknot imaged (redundant)S52546987S529889 (indistinguishable brain neurons)not imaged (redundant)S52989088S529890 (indistinguishable brain neurons)not imaged (redundant)-S52988988S529890 (indistinguishable brain neurons)not imaged (redundant)-S529889	76	SS41820	strong	-	-	-	0	-		-
77SS41821strongnot imaged (redundant)-SS41808 SS41809 SS4182078SS42007strongnot imaged (redundant)-SS4200879SS42707mediumMot imaged (redundant)-SS4200880SS43528strongweakImaged (redundant)-SS3801281SS48632mediumImaged (redundant)-SS4840982SS51024strongSS120983SS52108strongweakSS2546984SS52106mediumSS2546985SS52107mediumSS2546986R86H08mediumweakSS2546987SS252107mediumSS2546988SS29890 (indistinguishable brain neurons)SS2546988SS29890 (indistinguishable brain neurons)SS2546988SS29890 (indistinguishable brain neurons)SS2546988SS29890 (indistinguishable brain neuro							()			
77       SS41821       strong       -       -       -       (redundant)       -       SS41809         78       SS42007       strong       -       -       -       not imaged (redundant)       -       SS42008         79       SS42707       medium       -       -       -       not imaged (redundant)       -       SS42008         80       SS43528       strong       weak       -       -       (undetectable in 2P); redundant)       -       SS48012         81       SS48632       medium       -       -       -       not imaged not imaged       -       SS48409         82       SS51024       strong       -       -       -       not imaged (redundant)       -       SS51029         83       SS52108       strong       weak       -       -       not imaged (redundant)       -       SS25102         84       SS52106       medium       -       -       -       not imaged (redundant)       -       SS25102         84       SS52106       medium       -       -       -       not imaged (redundant)       -       SS25108         85       SS52107       medium       -       -       - <t< td=""><td></td><td></td><td></td><td></td><td></td><td></td><td></td><td></td><td></td><td></td></t<>										
redundant)       SS41809         78       SS42007       strong       -       -       not imaged (redundant)       -       SS42700         79       SS42707       medium       -       -       -       not imaged (redundant)       -       SS42740         80       SS43528       strong       weak       -       -       redundant)       -       R70H06         80       SS43528       strong       weak       -       -       (undetectable in 2P; redundant)       -       SS48409         81       SS48632       medium       -       -       -       not imaged (redundant)       -       SS42502         81       SS48632       medium       -       -       -       not imaged (redundant)       -       SS48409         82       SS51024       strong       -       -       -       not imaged (redundant)       -       SS51029         83       SS52108       strong       weak       -       -       not imaged (redundant)       -       SS52106         84       SS52106       medium       -       -       not imaged (redundant)       -       SS25469         85       SS52107       medium       weak	77	SS41821	strong	-	-	_		-		_
78SS42007strongnot imaged (redundant)-SS4200879SS42707mediumnot imaged (redundant)-SS4274080SS43528strongweaknot imaged (redundant)-SS3801281SS48632mediumnot imaged (redundant)-SS3801282SS51024strongnot imaged (redundant)-SS5102983SS52108strongweaknot imaged (redundant)-SS5210984SS52106mediumnot imaged (redundant)-SS5210684SS52106mediumnot imaged (redundant)-SS5210784SS52107mediumnot imaged (redundant)SS5210885SS52107mediumnot imaged (redundant)SS5210886R86H08mediumweaknot imaged (redundant)SS2859687SS29899indistinguishable brain neurons)not imaged (redundant)SS2989888SS29890not imaged (redundant)-SS2988988SS29890not imaged (redundant)-SS2988989strong b			8				(redundant)			
18       SS42007       strong       -       -       -       (redundant)       -       SS42008         79       SS42707       medium       -       -       not imaged       SS42707       R70H06         80       SS43528       strong       weak       -       -       (redundant)       -       R70H06         81       SS4632       medium       -       -       (undetectable in 2P; redundant)       -       SS48409         82       SS51024       strong       -       -       not imaged       -       SS51029         83       SS52108       strong       weak       -       -       not imaged       -       SS52107         84       SS52106       medium       -       -       -       not imaged       SS52107         84       SS52106       medium       -       -       -       not imaged       SS52107         85       SS52107       medium       -       -       -       not imaged       SS52108         86       R86H08       medium       weak       -       -       not imaged       SS52108         87       SS52989 (indistinguishable brain neurons)       -       -       -							not imaged		5541820	
79SS42707mediumnot imaged (redundant)SS42740 (redundant)80SS43528strongweak(undetectable in 2P; redundant)-SS38012 redundant)81SS48632medium(undetectable in 2P; (redundant)-SS4840982SS51024strongnot imaged (redundant)-SS5102983SS52108strongweaknot imaged (redundant)-SS2546984SS52106mediumnot imaged (redundant)-SS2546984SS52106mediumnot imaged (redundant)-SS2546985SS52107mediumnot imaged (redundant)-SS25469 SS2510686R86H08mediumweaknot imaged (redundant)SS252108 SS2510887SS29889 (indistinguishable brain neurons)not imaged (redundant)SS2989988SS29889 (indistinguishable brain neurons)not imaged (redundant)-SS2989888SS29889 (indistinguishable brain neurons)not imaged (redundant)-SS29889	78	SS42007	strong	-	-	-		-	SS42008	-
193542101intertunit111 </td <td>70</td> <td>9949707</td> <td></td> <td></td> <td></td> <td></td> <td></td> <td></td> <td>SS42740</td> <td></td>	70	9949707							SS42740	
80       SS43528       strong       weak       -       -       (undetectable in 2P; redundant)       -       SS38012         81       SS48632       medium       -       -       not imaged (redundant)       -       SS48409         82       SS51024       strong       -       -       -       not imaged (redundant)       -       SS51029         83       SS52108       strong       weak       -       -       not imaged (redundant)       -       SS52106         84       SS52106       medium       -       -       -       not imaged (redundant)       -       SS52107         84       SS52106       medium       -       -       -       not imaged (redundant)       -       SS52107         85       SS52106       medium       -       -       -       not imaged (redundant)       -       SS52107         85       SS52107       medium       -       -       -       not imaged (redundant)       -       SS52108         86       R86H08       medium       weak       -       -       not imaged (redundant)       SS28596         87       SS29889 (indistinguishable brain neurons)       -       -       not imaged (redundant) </td <td>9</td> <td>5542707</td> <td>medium</td> <td>-</td> <td>-</td> <td>-</td> <td></td> <td>-</td> <td>R70H06</td> <td>-</td>	9	5542707	medium	-	-	-		-	R70H06	-
redundant)81SS48632mediumnot imaged (redundant)-SS4840982SS51024strongnot imaged (redundant)-SS5102983SS52108strongweaknot imaged (redundant)-SS2546984SS52106mediumnot imaged (redundant)SS25107SS2510784SS52107mediumnot imaged (redundant)SS2510885SS52107mediumnot imaged (redundant)SS2510886R86H08mediumweaknot imaged (redundant)SS2510887SS29889 (indistinguishable brain neurons)not imaged (redundant)SS2889088SS29890 (indistinguishable brain neurons)not imaged (redundant)SS29889weaknot imaged (redundant)SS2108SS210888SS29890 (indistinguishable brain neurons)SS2989089SS29890 (indistinguishable brain neurons)SS2989089SS29890 (indistinguishable brain neurons)SS2988980SS2989081 <t< td=""><td></td><td>~~.~~~</td><td></td><td></td><td></td><td></td><td>0</td><td></td><td></td><td></td></t<>		~~.~~~					0			
81       SS48632 medium       -       -       not imaged (redundant)       -       SS48409         82       SS51024 strong       -       -       not imaged (redundant)       -       SS51029         83       SS52108 strong       weak       -       -       not imaged (redundant)       -       SS25469         84       SS52108 medium       -       -       not imaged (redundant)       -       SS25469         84       SS52106 medium       -       -       not imaged (redundant)       -       SS25469         85       SS52107 medium       -       -       -       not imaged (redundant)       SS25469         86       R86H08 medium       weak       -       -       not imaged (redundant)       SS25469         87       SS52107 medium       -       -       -       not imaged (redundant)       SS25469         86       R86H08 medium weak       -       -       not imaged (redundant)       SS28596       SS29890         87       SS29889 (indistinguishable brain neurons)       -       -       -       not imaged (redundant)       SS29890         88       SS29890 (indistinguishable brain neurons)       -       -       -       not imaged (redundant)       -<	30	SS43528	strong	weak	-	-		; -	SS38012	-
81       S548632       medium       -       -       -       (redundant)       -       S548409         82       S551024       strong       -       -       -       not imaged (redundant)       -       S551029         83       S552108       strong       weak       -       -       not imaged (redundant)       -       S552106         84       S552106       medium       -       -       -       not imaged (redundant)       -       S525106         84       S552106       medium       -       -       -       not imaged (redundant)       -       S525107         84       S552107       medium       -       -       -       not imaged (redundant)       -       S525106         85       S552107       medium       weak       -       -       not imaged (redundant)       -       S52108         86       R86H08       medium       weak       -       -       not imaged (redundant)       -       S529890         87       S529889 (indistinguishable brain neurons)       -       -       -       not imaged (redundant)       -       S529889         88       S529890 (indistinguishable brain neurons)       -       - <td< td=""><td></td><td></td><td></td><td></td><td></td><td></td><td></td><td></td><td></td><td></td></td<>										
82       SS51024       strong       -       -       not imaged (redundant)       -       SS51029         83       SS52108       strong       weak       -       not imaged (redundant)       -       SS25469         84       SS52106       medium       -       -       not imaged (redundant)       -       SS25469         84       SS52106       medium       -       -       -       not imaged (redundant)       -       SS25469         85       SS52107       medium       -       -       -       not imaged (redundant)       -       SS25469         85       SS52107       medium       -       -       -       not imaged (redundant)       -       SS25469         86       R86H08       medium       weak       -       -       not imaged (redundant)       -       SS25106         87       SS29890 (indistinguishable brain neurons)       -       -       -       not imaged (redundant)       -       SS29890         88       SS29890 (indistinguishable brain neurons)       -       -       -       not imaged (redundant)       -       SS29889	31	SS48632	medium	-	-	-		-	SS48409	-
83       SS52108       strong       weak       -       not imaged (redundant)       -       SS25469 SS52107         84       SS52106       medium       -       -       not imaged (redundant)       -       SS25469 SS25469         85       SS52107       medium       -       -       -       not imaged (redundant)       -       SS25469         85       SS52107       medium       -       -       -       not imaged (redundant)       -       SS25469         86       R86H08       medium       weak       -       -       not imaged (redundant)       SS28596         87       SS29889 (indistinguishable brain neurons)       -       -       -       not imaged (redundant)       -       SS29890         88       SS29890 (indistinguishable brain neurons)       -       -       -       not imaged (redundant)       -       SS29890         88       SS29890 (indistinguishable brain neurons)       -       -       -       not imaged (redundant)       -       SS29889	20	9951094	atuana						5551000	
83       SS52108       strong       weak       -       -       not imaged (redundant)       -       SS52106         84       SS52106       medium       -       -       not imaged (redundant)       -       SS52107         85       SS52107       medium       -       -       -       not imaged (redundant)       -       SS52108         85       SS52107       medium       -       -       -       not imaged (redundant)       -       SS52108         86       R86H08       medium       weak       -       -       not imaged (redundant)       SS28596         87       SS29889 (indistinguishable brain neurons)       -       -       -       not imaged (redundant)       -       SS29890         88       SS29890 (indistinguishable brain neurons)       -       -       -       not imaged (redundant)       -       SS29890         88       SS29890 (indistinguishable brain neurons)       -       -       -       not imaged (redundant)       -       SS29889	52	5501024	strong	-	-	-	(redundant)	-		-
83       S552108       strong       weak       -       -       (redundant)       -       S552107         84       S552106       medium       -       -       -       not imaged (redundant)       -       S552107         85       S552107       medium       -       -       -       not imaged (redundant)       -       S552108         86       R86H08       medium       weak       -       -       not imaged (redundant)       -       S552108         87       S529889 (indistinguishable brain neurons)       -       -       -       not imaged (redundant)       -       S5228596         88       S529890 (indistinguishable brain neurons)       -       -       -       not imaged (redundant)       -       S529899         88       S529890 (indistinguishable brain neurons)       -       -       -       not imaged (redundant)       -       S529899	20	0050100		. 1			not imaged			
84       SS52106       medium       -       -       not imaged (redundant)       -       SS52107 SS52108         85       SS52107       medium       -       -       -       not imaged (redundant)       -       SS52108         86       R86H08       medium       weak       -       -       not imaged (redundant)       -       SS52108         87       SS529899 (indistinguishable brain neurons)       -       -       -       not imaged (redundant)       -       SS29890         88       SS29890 (indistinguishable brain neurons)       -       -       -       not imaged (redundant)       -       SS29890         98       SS29890 (indistinguishable brain neurons)       -       -       -       not imaged (redundant)       -       SS29890	33	\$\$52108	strong	weak	-	-		-		-
84       SS52106       medium       -       -       not imaged (redundant)       -       SS52107 SS52108         85       SS52107       medium       -       -       not imaged (redundant)       -       SS52107 SS52108         86       R86H08       medium       weak       -       -       not imaged (redundant)       -       SS28596         87       SS29889 (indistinguishable brain neurons)       -       -       -       not imaged (redundant)       -       SS29890         88       SS29890 (indistinguishable brain neurons)       -       -       -       not imaged (redundant)       -       SS29890         90       strong brain neurons)       -       -       -       not imaged (redundant)       -       SS29890										
85       SS52107       medium       -       -       not imaged (redundant)       -       SS25409 SS52108         86       R86H08       medium       weak       -       -       not imaged (redundant)       SS258596         87       SS29889 (indistinguishable brain neurons)       -       -       -       not imaged (redundant)       -       SS29890         88       SS29890 (indistinguishable brain neurons)       -       -       -       not imaged (redundant)       -       SS29890         88       SS29890 (indistinguishable brain neurons)       -       -       -       not imaged (redundant)       -       SS29890	34	SS52106	medium	-	-	-		-		-
85       SS52107       medium       -       -       -       not imaged (redundant)       -       SS52106 SS52108         86       R86H08       medium       weak       -       -       not imaged (redundant)       SS28596         87       SS29889 (indistinguishable brain neurons)       -       -       -       not imaged (redundant)       -       SS29890         88       SS29890 (indistinguishable brain neurons)       -       -       -       not imaged (redundant)       -       SS29889         98       SS29890 (indistinguishable brain neurons)       -       -       -       0       SS29889         90       indistinguishable brain neurons)       -       -       -       not imaged (redundant)       -       SS29889							(redundant)		SS52108	
85       S552107       medium       -       -       (redundant)       S552106         86       R86H08       medium       weak       -       -       not imaged (redundant)       SS28596         87       SS29889 (indistinguishable brain neurons)       -       -       -       not imaged (redundant)       -       SS29890         88       SS29890 (indistinguishable brain neurons)       -       -       -       not imaged (redundant)       -       SS29889         98       SS29890 (indistinguishable brain neurons)       -       -       -       not imaged (redundant)       -       SS29889							not imaged			
86       R86H08       medium       weak       -       not imaged (redundant)       SS28596         87       SS29889 (indistinguishable brain neurons)       -       -       not imaged (redundant)       -       SS29890         88       SS29890 (indistinguishable brain neurons)       -       -       -       not imaged (redundant)       -       SS29890         88       SS29890 (indistinguishable brain neurons)       -       -       -       not imaged (redundant)       -       SS29889	55	SS52107	medium	-	-	-		-		-
86     R86H08     medium     weak     -     -     (redundant)     SS28596       87     SS29889 (indistinguishable brain neurons)     -     -     -     not imaged (redundant)     -     SS29890       88     SS29890 (indistinguishable brain neurons)     -     -     -     not imaged (redundant)     -     SS29889							. , ,			
strong     not imaged       87     SS29889 (indistinguishable (redundant))       strong     strong       88     SS29890 (indistinguishable not imaged (redundant))       wurreliable     SS29890	36	R86H08	medium	weak	-	-			SS28596	-
87 S529889 (indistinguishable (redundant) - S529890       brain neurons)       88 S529890 (indistinguishable not imaged brain neurons)       unreliable   not imaged			strong				· · · · ·			
strong 88 SS29890 (indistinguishable not imaged brain neurons) unreliable not imaged	37	SS29889	(indistinguishable	e -	-	-		-	SS29890	-
88 SS29890 (indistinguishable (redundant) SS29889 brain neurons)							(redundant)			
88 S529890 (indistinguishable (redundant)     - S529889       brain neurons)     not imaged	00	2200000					not imaged		6690666	
unreliable not imaged	0ð	5529890		-	-	-		-	5529889	-
			stan neurons)	1. 1. 1.1			not imaged			
of 5525000 - (unreliable	39	SS29605	-		-	-	(unreliable	-	-	-
expression expression)				expression			expression)			

	Table 1 continued from previous page								
No.	Gal4	Confocal SNR of smFP	2P SNR of OpGCaMP6f and tdTomato		ROI#	Encoding	Level synchronous activity H (ROI# vs ROI#: Corr. coef.)	Redundaı Gal4	nt Supp. Video#
90	SS31246	unreliable expression	unreliable expression	-	-	$\begin{array}{c} { m not\ imaged} \\ { m (unreliable} \\ { m expression)} \end{array}$	-	-	-
91	SS46696	unreliable expression	unreliable expression	-	-	$\begin{array}{c} { m not\ imaged} \\ { m (unreliable} \\ { m expression)} \end{array}$	-	-	-
92	R75E01	strong but with glia	-	-	-	not imaged (glia included)	-	-	-
93	SS37652	medium	weak	-	-	not imaged $(undetectable)$	-	-	-
94	SS41602	strong	weak	-	-	not imaged (undetectable)	-	-	-
95	SS43651	strong	weak	-	-	not imaged (undetectable)	-	-	-
96	SS44305	strong	weak	-	-	not imaged (undetectable)	-	-	-
97	SS46255	strong	weak	-	-	not imaged (undetectable) not imaged	-	-	-
98	SS41824	strong	weak	-	-	(undetectable)	-	-	-
99	SS25488	-	weak	-	-	not imaged (undetectable) not imaged	-	-	-
100	R81G07	weak	weak	•	•	(undetectable) not imaged	-	•	-
101	SS45635	weak	weak	-	-	(undetectable) not imaged	-	-	-
-	SS45648	weak	weak	-	-	(undetectable) not imaged	-	-	-
	SS46290	weak	weak	-	-	(undetectable) not imaged	-	-	-
	SS46847	weak	weak	-	-	(undetectable) not imaged	-	-	-
	SS47868	weak	weak	-	-	(undetectable) not imaged	-	-	-
	SS50282	weak	weak	-	-	(undetectable) not imaged	-	-	-
	SS50829	weak	weak	-	-	(undetectable) not imaged	-	-	-
108	R88C08	weak	weak	-	-	(undetectable)	-	-	-

34

			,
	Driver line	AD	DBD
1 2	$SS36131 \\ SS38592$	R70D06 VT016458	VT033054 VT012410
3	SS27485	R75E01	R18B05
4	SS41822	VT033054	VT026646
5	SS38624	VT002081	R85H01
$\frac{6}{7}$	SS45605 SS43652	R15E01 VT026477	R41E03 R38E07
8	SS36112	VT026646	VT028606
9	SS41806	VT060737	VT028606
10	SS38631	R72A10	VT038208
11 12	SS51029 R85A11	VT034810	VT004985
13	SS40489	R36B06	VT007767
14	SS31480	R68C10	VT008150
15	SS51021	VT027767	VT027005
16 17	SS51017 SS31456	VT005404 VT013500	VT027767 VT012768
18	SS46233	VT029814	VT028464
19	SS42749	R66A06	VT056770
20	SS41815	VT043377	VT014669
21 22	SS29633 R87H02	R33F06	R76E11
23	MAN	VT50660	VT14014
24	SS49172	VT049120	VT008188
25	R36G04	-	-
26 27	R39G01 SS31219	- VT045153	- VT019074
27	R30A08	-	-
29	SS44270	VT058560	VT033054
30	SS41605	R80A11	VT038205
31 32	$\frac{SS29579}{SS51046}$	VT023828 VT007177	VT059224 VT057280
33	SS29893	R67F03	VT050658
34	SS34574	VT008537	VT050658
35	R70H06	-	-
36 37	SS42740 SS25469	VT037865 VT027704	VT061717 VT044958
38	SS31232	VT063643	VT059781
39	SS30303	VT063643	VT018278
40	SS25451	VT063643	VT059224
41 42	$SS28596 \\ SS40134$	R94B04 VT028320	R86H08 R49A01
43	SS29621	R22E07	R30E10
44	R69H10	-	-
45	SS51038	VT030558	VT001497
$\frac{46}{47}$	SS42008 SS36118	VT033469 VT060737	VT043682 VT026477
48	SS40619	VT021853	VT050234
49	SS45363	VT062587	VT043920
50	SS52147 R38F09	VT044164	VT040034
51 52	SS46269	- VT023490	- VT016254
53	SS25470	VT063643	VT048352
54	SS25478	VT025966	VT013121
55	SS28382	R18G02	R49C03
$\frac{56}{57}$	SS29574 SS31899	VT008660 R26H04	VT043400 R46A10
58	SS33380	R19F01	R60A06
59	SS33433	R94D12	VT060731
60 61	SS38012 SS38386	R48E02 VT016966	R93B07 VT046334
61	SS38687	R30A02	V1046334 VT015159
63	SS46290	VT029750	VT043288
64	SS46300	VT043146	VT000254
65 66	SS48406	VT048352 VT036302	VT039769 VT049125
66 67	SS48409 SS49982	R77D08	VT049125 VT029514
68	SS50004	VT017645	VT049348
69	SS50013	VT008992	VT039485
70	SS50652 SS36132	R60C01 R70D06	R80B01
71 72	SS36132 SS36133	R70D06 R70D06	VT025996 VT026646
73	SS38598	VT024634	VT016458
74	SS41808	VT060737	VT033054
75 76	SS41809 SS41820	R20E05 VT060737	VT033054 VT025996
76 77	SS41820 SS41821	R20E05	VT025996
78	SS42007	VT033469	VT026646
79	SS42707	VT061717	VT045101
80 81	SS43528 SS48632	VT025966 VT036302	R93B07 R93B07
81	SS51024	V 1036302 VT004985	VT034810

Table 2: Activation (AD) and DNA-binding Domains (DBD) of split-Gal4 lines

$\mathbf{Tab}$	Table 2 continued from previous page							
	Driver line	AD	DBD					
83	SS52108	VT063231	R69H06					
84	SS52106	VT063231	VT063626					
85	SS52107	VT063231	VT021731					
86	R86H08	-	-					
87	SS29889	R64G04	VT008537					
88	SS29890	R64G04	VT050658					
89	SS29605	VT019902	VT048942					
90	SS31246	VT038171	VT021780					
91	SS22721	R92D09	R92A07					
92	R75E01	-	-					
93	SS37652	VT040698	VT023490					
94	SS41602	R75E01	R74C01					
95	SS43651	VT026477	VT039361					
96	SS44305	R21E09	VT016966					
97	SS46255	R24H02	VT037862					
98	SS41824	R20E05	VT026646					
99	SS25488	VT029593	VT020527					
100	R81G07	-	-					
101	SS45635	VT008882	VT014208					
102	SS45648	VT008808	VT029814					
103	SS46290	VT029750	VT043288					
104	SS46847	VT023490	VT039485					
105	SS47868	R24H02	VT002064					
106	SS50282	VT037554	VT012768					
107	SS50829	VT033290	VT027767					
108	R88C08	-	-					

# <sup>939</sup> 7 Supplementary Figures

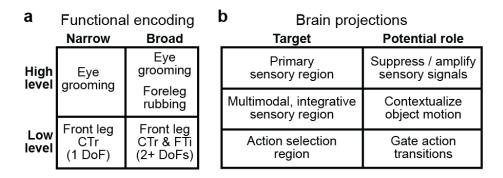


Figure S1: Hypothetical ascending neuron functional encoding and brain targeting. (a) ANs might encode high-level behaviors, or low-level limb kinematics. This encoding may be either narrow (e.g., one behavior, or joint degree-of-freedom), or broad (e.g., several behaviors, or joint DoFs). (b) ANs might target the brain's (i) primary sensory regions (e.g., optic lobe, or antennal lobe) to perform sensory gain control, (ii) multimodal and integrative sensory regions (e.g., anterior ventrolateral protocerebrum, or mushroom body) to contextualize time-varying sensory cues, or (iii) action selection centers (e.g., gnathal ganglion, or central complex) to gate action transitions. Individual ANs may project broadly to multiple brain regions, or narrowly to one region.

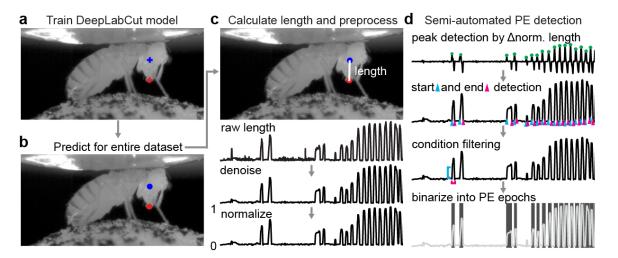


Figure S2: Semi-automated tracking of proboscis extensions. We detected proboscis extensions using side-view camera images. (a) First, we trained a deep neural network model with manual annotations of landmarks on the ventral eye (blue cross) and distal proboscis tip (red cross). (b) Then we applied the trained model to estimate these locations throughout the entire dataset. (c) Proboscis extension length was calculated as the denoised and normalized distance between landmarks. (d) Using these data, we performed semi-automated detection of PE epochs by first identifying peaks from normalized proboscis extension lengths. Then we detected the start (cyan triangle) and end (magenta triangle) of these events. We removed false-positive detections by thresholding the amplitude (cyan line) and duration (magenta line) of events. Finally, we generated a binary trace of PE epochs (shaded area).

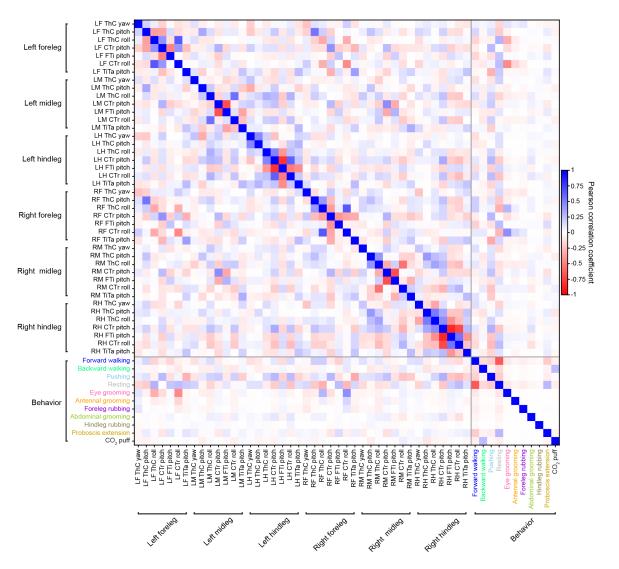


Figure S3: Correlations among and between low-level joint angles and high-level behaviors. Pearson correlation coefficients (color-coded) for joint angles, high-level behavioral states, proboscis extensions, and puffs.

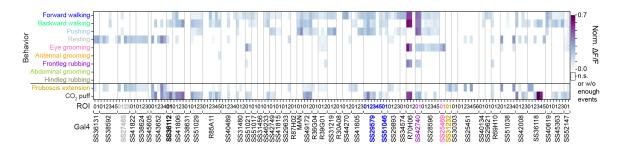


Figure S4: Normalized mean activity ( $\Delta F/F$ ) of ascending neurons during high-level behaviors. Normalized mean  $\Delta F/F$  for a given AN across all epochs of a specific high-level behavior. Analyses were performed for 157 ANs recorded from 50 driver lines. Lines selected for more in-depth analysis are color-coded by the behavioral state best explaining their neural activity: SS27485 (resting), SS36112 (puff responses), SS29579 (walking), SS51046 (turning), SS42740 (foreleg-dependent behaviors), SS25469 (eye grooming), and SS31232 (proboscis extensions). Note that fluorescence for non-orthogonal behaviors/events may overlap (e.g., for backward walking and puff, or resting and proboscis extensions). To minimize contamination due to signals from preceding behaviors (resulting from the long decay kinetics of calcium indicators), conditions with less than ten epochs longer than 0.7 s are masked (white).  $\Delta F/F$  signals are normalized between 0 and 1 to minimize the influence of differences in calcium indicator expression levels on data interpretation. ANOVA and posthoc Tukey tests to correct for multiple comparisons were performed to test if values are significantly different from baseline. Non-significant samples are also masked (white).

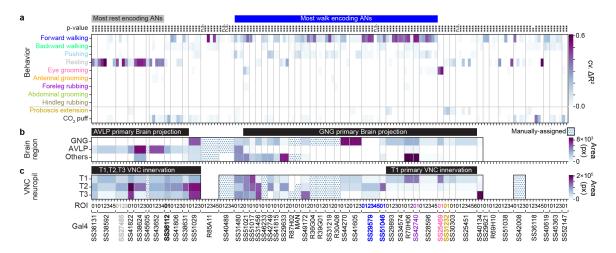


Figure S5: Relationship between ascending neuron behavioral encoding, brain targeting, and VNC patterning. (a) Variance in AN activity that can be uniquely explained by a regressor (cross-validated  $\Delta R^2$ ) for high-level behaviors. Regression analyses were performed for 157 ANs recorded from 50 driver lines. Lines (and their corresponding ANs) selected for more in-depth analysis are color-coded by the behavioral class that best explains their neural activity: SS27485 (resting), SS36112 (puff responses), SS29579 (walking), SS51046 (turning), SS42740 (foreleg-dependent behaviors), SS25469 (eye grooming), and SS31232 (proboscis extensions). Non-orthogonal regressors (PE and CO<sub>2</sub> puffs) are separated from the others. *P*-values report the F-statistic of overall significance of the complete regression model with no regressors shuffled (\*p<0.05, \*\*p<0.01, and \*\*\*p<0.001). The most substantial AN (b) targeting of brain regions, or (c) patterning of VNC regions, as quantified by pixel-based analysis of MCFO labelling. Driver lines that were manually quantified are indicated (dotted cells). Projections that could not be unambiguously identified are left blank. Notable encoding and innervation patterns are indicated by bars above each matrix.

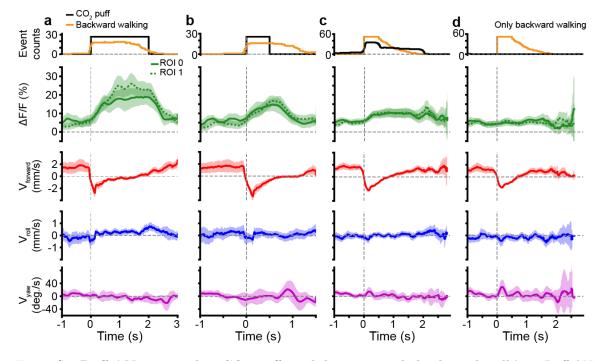


Figure S6: **Puff-ANs respond to CO<sub>2</sub> puffs and do not encode backward walking.** Puff-ANs (SS36112) activity (green) and corresponding spherical treadmill rotational velocities (red, blue, and purple) during (a) long, 2 s CO<sub>2</sub>-puff stimulation (black) and associated backward walking (orange), (b) short, 0.5 s CO<sub>2</sub>-puff stimulation, (c) periods with backward walking, and (d) the same backward walking events as in c but only during periods without coincident puff stimulation. Shown are the mean (solid and dashed lines) and 95% confidence interval (shaded areas) of multiple  $\Delta F/F$  and ball rotation time-series.

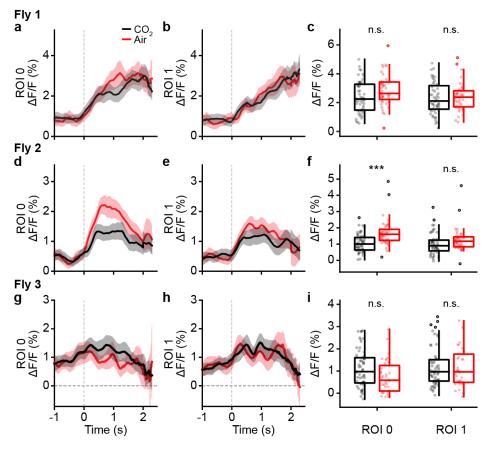


Figure S7: **Puff-ANs respond similarly to puffs of air, or CO<sub>2</sub>.** Activity of puff-ANs (SS36112) from three flies (**a-c**, **d-f**, and **g-i**, respectively) in response to puffs of air (red), or CO<sub>2</sub> (black). (**a-b**, **d-e**, **g-h**) Shown are mean (solid and dashed lines) and 95% confidence interval (shaded areas)  $\Delta F/F$  for ROIs (**a**, **d**, **g**) 0 and (**b**, **e**, **h**) 1. (**c**, **f**, **i**) Mean fluorescence (circles) of traces for ROIs 0 (left) or 1 (right) from 0.7 s after puff onset until the end of stimulation. Overlaid are box plots representing the median, interquartile range (IQR), and 1.5 IQR. Outliers beyond 1.5 IQR are indicated (opaque circles). A Mann-Whitney test (\*\*\* p<0.001, \*\* p<0.01, \* p<0.05) was used to compare responses to puffs of CO<sub>2</sub> (red), or air (black).

а

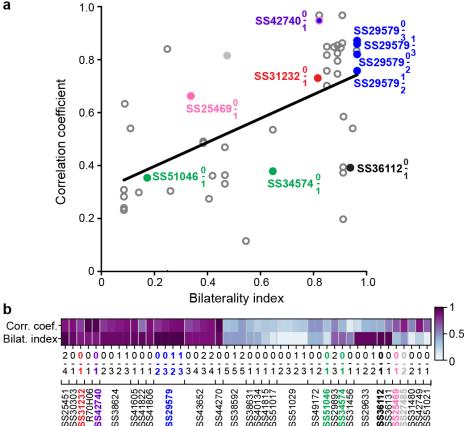


Figure S8: The bilaterality of an ascending neuron pair's VNC patterning correlates with the degree of synchronous activity. (a) A bilaterality index, quantifying the differential innervation of left and right VNC (without distinguishing between axons and dendrites) is compared with the Pearson correlation coefficient for activity of left and right ANs within a pair ( $R^2 = 0.31$ and p < 0.001 using an F-test). (b) Bilaterality index and Pearson correlation coefficient values for each AN pair examined.

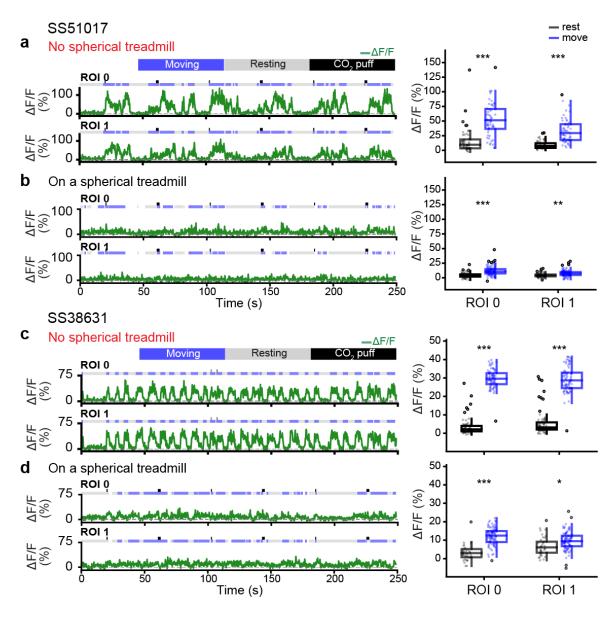


Figure S9: Ascending neurons that become active only in the absence of the spherical treadmill. Representative AN recordings from ROIs 0 and 1 for (**a**, **b**) one SS51017-spGal4 animal, or (**c**, **d**) one SS38631-spGal4 animal measured when it is (**a**, **c**) suspended without a spherical treadmill, or (**b**, **d**) in contact with the spherical treadmill. Moving, resting, and puff stimulation epochs are indicated. Shown are (left) representative neural activity traces and (right) summary data including the median, interquartile range (IQR), and 1.5 IQR of AN  $\Delta F/F$  values when the animal are resting (black), or moving (blue). Outliers (values beyond 1.5 IQR) are indicated (black circles). Statistical comparisons were performed using a Mann-Whitney test (\*\*\* p<0.001, \*\* p<0.01, \* p<0.05).

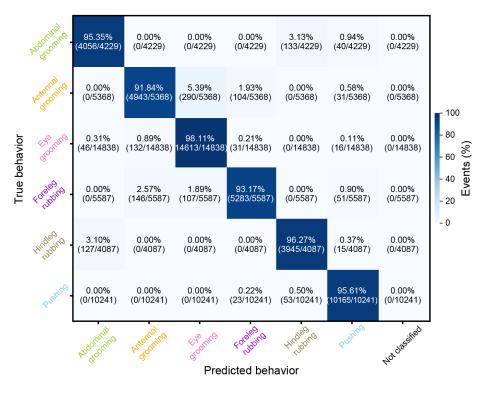


Figure S10: **Behavior classifier accuracy.** A confusion matrix quantifies the accuracy of predictions using 10-fold, stratified cross-validation of a histogram gradient boosting classifier. Walking and resting are not included in this evaluation because they are predicted using spherical treadmill rotation data. The percentage of events in each category ('predicted' behavior versus ground-truth, manually-labelled 'true' behavior) is color-coded.

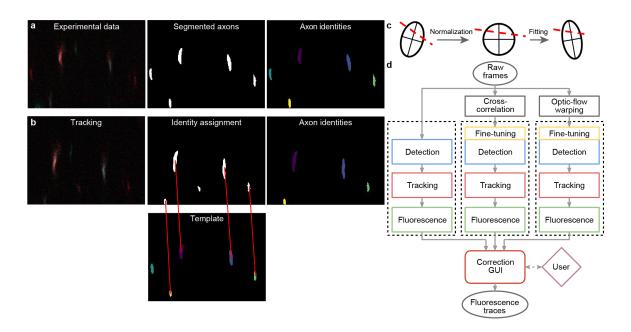


Figure S11: AxoID, a deep learning-based algorithm tracks axonal cross-sections in twophoton microscopy images. (a) Pipeline overview: a single image frame (left) is segmented (middle) during the detection stage with potential axons shown (white). Tracking identities (right) are then assigned to these ROIs. (b) To track ROIs across time, ROIs in a tracker template (bottommiddle) are matched (red lines) to ROIs in the current segmented frame (top-middle). An undetected axon in the tracker template (cyan) is left unmatched. (c) ROI separation is performed for fused axons. An ellipse is first fit to the ROI's contour and a line is fit to the separation (dashed red line). For normalization, the ellipse is transformed into an axis-aligned circle and the linear separation is transformed accordingly. For another frame, a transformation of the circle into a newly fit ellipse is computed and applied to the line. The ellipse's main axes are shown for clarity. (d) The AxoID workflow. Raw experimental data is first registered via cross-correlation and optic flow warping. Then, raw and registered data are separately processed by the fluorescence extraction pipeline (dashed rectangles). Finally, a GUI is used to select and correct the results.

#### Supplementary Videos 8 940

Video 1: High-level behaviors, their associated 3D poses, and spherical treadmill rota-941

tional velocities. Behaviors were captured from six camera views. Illuminated text (top) indicates 942 the regressor being illustrated. Also shown are corresponding 3D poses (bottom-left) and spher-943 ical treadmill rotational velocities, proboscis extension (PE) lengths, and puff stimulation periods 944 945 (bottom-right).

https://www.dropbox.com/s/xed6jfgyqf7ubft/Video1.mov?dl=0 946

Video 2: Representative data for 50 comprehensively analyzed, AN-targeting sparse 947 driver lines. Shown are: (a) spFP staining, (b) a representative two-photon microscope image, 948 (c) outline of the associated cervical connective after filling the surrounding bath with fluorescent 949 dve, (d) and PE length, puff stimuli, spherical treadmill rotational velocities, and AN (ROI)  $\Delta F/F$ 950 traces. Indicated above are regressors for forward walking ('F.W.'), backward walking ('B.W.'), 951 resting ('Rest'), eye grooming ('Eye groom'), antennal grooming ('Ant. groom'), foreleg rubbing ('Fl. 952 rub'), abdominal grooming ('Abd. groom'), hindleg rubbing ('Hl. rub'), and proboscis extension 953 ('PE'). For each driver line, the title indicates 'date-Gal4-reporters-fly-trial'. 954

https://www.dropbox.com/s/73aymyw3quiw142/Video2.mov?dl=0 955

Videos 3 - 52: Representative behavioral videos and AN two-photon imaging data for 956 50 comprehensively analyzed, AN-targeting sparse driver lines.

957 https://drive.switch.ch/index.php/s/Q9K5BvugJc190rV

958

#### Data and code availability 9 959

```
Data are available at:
960
```

```
https://dataverse.harvard.edu/dataverse/AN
961
```

```
963
```

```
Analysis code is available at:
963
```

```
https://github.com/NeLy-EPFL/Ascending_neuron_screen_analysis_pipeline
964
```

AxoID code is available at: 966

```
https://github.com/NeLy-EPFL/AxoID
967
```

```
968
```

965

### Funding 10969

PR acknowledges support from an SNSF Project grant (175667) and an SNSF Eccellenza grant 970 (181239). FA acknowledges support from a Boehringer Ingelheim Fonds PhD stipend. 971

### 11Acknowledgments 972

We thank the Janelia Research Campus FlyLight project for generating Ascending Neuron split-Gal4 973 driver lines. 974

### Author Contributions 12975

C-L.C. - Conceptualization, Methodology, Software, Validation, Formal Analysis, Investigation, Data 976

Curation, Validation, Writing – Original Draft Preparation, Writing – Review & Editing, Visualiza-977 tion. 978

F.A. - Methodology, Software, Formal Analysis, Investigation, Data Curation, Validation, Data Cu-979

- ration, Writing Original Draft Preparation, Writing Review & Editing. 980
- R.M. Methodology, Investigation, Data Curation, Validation. Writing Review & Editing 981
- V.M. Investigation, Data Curation, Visualization. Writing Review & Editing 982
- N.T. Methodology, Software, Formal Analysis, Data Curation Visualization. Writing Review & 983

- 984 Editing
- S.G. Methodology, Software, Formal Analysis, Data Curation, Visualization. Writing Review &
   Editing
- <sup>987</sup> B.D. Resources, Writing Review & Editing, Supervision, Project Administration, Funding Acqui-
- <sup>988</sup> sition. Writing Review & Editing
- 989 P.R. Conceptualization, Methodology, Resources, Writing Original Draft Preparation, Writing –
- <sup>990</sup> Review & Editing, Supervision, Project Administration, Funding Acquisition.
- 991

# <sup>992</sup> 13 Competing interests

<sup>993</sup> The authors declare that no competing interests exist.

## 994 **References**

- [1] Crapse, T. B. & Sommer, M. A. Corollary discharge across the animal kingdom. Nature Reviews
   Neuroscience 9, 587–600 (2008).
- Brooks, R. A. A robust layered control system for a mobile robot. *IEEE Journal on Robotics* and Automation 2, 14–23 (1986).
- [3] Niell, C. M. & Stryker, M. P. Modulation of visual responses by behavioral state in mouse visual cortex. *Neuron* 65, 472–479 (2010).
- [4] Musall, S., Kaufman, M. T., Juavinett, A. L., Gluf, S. & Churchland, A. K. Single-trial neural dynamics are dominated by richly varied movements. *Nature Neuroscience* **22**, 1677–1686 (2019).
- [5] Stringer, C. *et al.* Spontaneous behaviors drive multidimensional, brainwide activity. *Science* **364**, eaav7893 (2019).
- [6] Maimon, G., Straw, A. D. & Dickinson, M. H. Active flight increases the gain of visual motion processing in *Drosophila*. *Nature Neuroscience* 13, 393–399 (2010).
- [7] Chiappe, M. E., Seelig, J. D., Reiser, M. B. & Jayaraman, V. Walking modulates speed sensitivity
   in *Drosophila* motion vision. *Current Biology* 20, 1470–1475 (2010).
- [8] Fujiwara, T., Cruz, T. L., Bohnslav, J. P. & Chiappe, M. E. A faithful internal representation of walking movements in the *Drosophila* visual system. *Nature Neuroscience* **20**, 72–81 (2016).
- [9] Aimon, S. *et al.* Fast near-whole-brain imaging in adult *Drosophila* during responses to stimuli and behavior. *PLOS Biology* **17**, e2006732 (2019).
- [10] Kim, A. J., Fitzgerald, J. K. & Maimon, G. Cellular evidence for efference copy in *Drosophila* visuomotor processing. *Nature Neuroscience* 18, 1247–1255 (2015).
- [11] Zacarias, R., Namiki, S., Card, G. M., Vasconcelos, M. L. & Moita, M. A. Speed dependent descending control of freezing behavior in *Drosophila melanogaster*. *Nature Communications* 9, 3697 (2018).
- [12] Tuthill, J. C. & Wilson, R. I. Parallel transformation of tactile signals in central circuits of Drosophila. Cell 164, 1046–1059 (2016).
- [13] Patestas, M. & Gartner, L. P. Ascending Sensory Pathways. In A Textbook of Neuroanatomy,
   chap. 10, 137–170 (Wiley, 2006), 1 edn.
- [14] Poulet, J. F. & Hedwig, B. New insights into corollary discharges mediated by identified neural pathways. *Trends in Neurosciences* **30**, 14–21 (2007).
- [15] Buchanan, J. T. & Einum, J. F. The spinobulbar system in lamprey. Brain Research Reviews
   57, 37–45 (2008).

- <sup>1026</sup> [16] Stecina, K., Fedirchuk, B. & Hultborn, H. Information to cerebellum on spinal motor networks <sup>1027</sup> mediated by the dorsal spinocerebellar tract. *The Journal of Physiology* **591**, 5433–5443 (2013).
- <sup>1028</sup> [17] Homberg, U. Flight-correlated activity changes in neurons of the lateral accessory lobes in the <sup>1029</sup> brain of the locust *Schistocerca gregaria*. *Journal of Comparative Physiology A* **175**, 597–610 <sup>1030</sup> (1994).
- <sup>1031</sup> [18] Burrows, M. Sensory effect on flying. In *The Neurobiology of An Insect Brain*, chap. 11, 541–544 <sup>1032</sup> (Oxford University Press, Oxford, 1996), 1 edn.
- <sup>1033</sup> [19] Chen, C. *et al.* Functional architecture of neural circuits for leg proprioception in *Drosophila*. <sup>1034</sup> *Current Biology* **31**, 1–13 (2021).
- <sup>1035</sup> [20] Agrawal, S. et al. Central processing of leg proprioception in Drosophila. eLife 9, e60299 (2020).
- <sup>1036</sup> [21] Tsubouchi, A. *et al.* Topological and modality-specific representation of somatosensory informa-<sup>1037</sup> tion in the fly brain. *Science* **358**, 615–623 (2017).
- <sup>1038</sup> [22] Fujiwara, T., Brotas, M. & Chiappe, M. E. Walking strides direct rapid and flexible recruitment <sup>1039</sup> of visual circuits for course control in *Drosophila*. *bioRxiv* (2021).
- <sup>1040</sup> [23] Mann, K., Gordon, M. & Scott, K. A pair of interneurons influences the choice between feeding <sup>1041</sup> and locomotion in *Drosophila*. *Neuron* **79**, 754–765 (2013).
- [24] Bidaye, S. S., Machacek, C., Wu, Y. & Dickson, B. J. Neuronal control of *Drosophila* walking direction. *Science* 344, 97–101 (2014).
- <sup>1044</sup> [25] Jenett, A. *et al.* A GAL4-driver line resource for *Drosophila* neurobiology. *Cell Reports* **2**, <sup>1045</sup> 991–1001 (2012).
- [26] Nern, A., Pfeiffer, B. D. & Rubin, G. M. Optimized tools for multicolor stochastic labeling
   reveal diverse stereotyped cell arrangements in the fly visual system. *Proceedings of the National Academy of Sciences of the United States of America* 112, E2967 LP E2976 (2015).
- [27] Chen, C.-L. *et al.* Imaging neural activity in the ventral nerve cord of behaving adult *Drosophila*.
   *Nature Communications* 9, 4390 (2018).
- <sup>1051</sup> [28] Günel, S. *et al.* DeepFly3D, a deep learning-based approach for 3D limb and appendage tracking <sup>1052</sup> in tethered, adult *Drosophila. eLife* **8**, e48571 (2019).
- [29] Seelig, J. D. *et al.* Two-photon calcium imaging from head-fixed *Drosophila* during optomotor
   walking behavior. *Nature Methods* 7, 535–540 (2010).
- <sup>1055</sup> [30] Panser, K. *et al.* Automatic segmentation of *Drosophila* neural compartments using GAL4 <sup>1056</sup> expression data reveals novel visual pathways. *Current Biology* **26**, 1943–1954 (2016).
- [31] Mohamed, A. A. M., Hansson, B. S. & Sachse, S. Third-order neurons in the lateral horn Enhance
   bilateral contrast of odor inputs through contralateral inhibition in *Drosophila*. Frontiers in
   *Physiology* 10, 851 (2019).
- [32] Matsuo, E. *et al.* Organization of projection neurons and local neurons of the primary auditory
   center in the fruit fly *Drosophila melanogaster*. Journal of Comparative Neurology 524, 1099–
   1164 (2016).
- [33] Lai, J. S.-Y., Lo, S.-J., Dickson, B. J. & Chiang, A.-S. Auditory circuit in the Drosophila brain.
   Proceedings of the National Academy of Sciences of the United States of America 109, 2607–2612
   (2012).
- [34] Kamikouchi, A., Shimada, T. & Ito, K. Comprehensive classification of the auditory sensory projections in the brain of the fruit fly *Drosophila melanogaster*. Journal of Comparative Neurology 499, 317–356 (2006).
- [35] Miyamoto, T. & Amrein, H. Suppression of male courtship by a *Drosophila* pheromone receptor.
   *Nature Neuroscience* 11, 874–876 (2008).

- [36] Tastekin, I. et al. Role of the subesophageal zone in sensorimotor control of orientation in
   Drosophila larva. Current Biology 25, 1448–1460 (2015).
- <sup>1073</sup> [37] Namiki, S., Dickinson, M. H., Wong, A. M., Korff, W. & Card, G. M. The functional organization <sup>1074</sup> of descending sensory-motor pathways in *Drosophila*. *eLife* (2018).
- [38] Mathis, A. *et al.* DeepLabCut: markerless pose estimation of user-defined body parts with deep
   learning. *Nature Neuroscience* 21, 1281–1289 (2018).
- [39] Rayshubskiy, A. et al. Neural circuit mechanisms for steering control in walking Drosophila.
   bioRxiv 2020.04.04.024703 (2020).
- <sup>1079</sup> [40] Trueta, C. & De-Miguel, F. Extrasynaptic exocytosis and its mechanisms: a source of molecules <sup>1080</sup> mediating volume transmission in the nervous system. *Frontiers in Physiology* **3**, 319 (2012).
- <sup>1081</sup> [41] Edwards, C. J., Leary, C. J. & Rose, G. J. Counting on inhibition and rate-dependent excitation <sup>1082</sup> in the auditory system. *Journal of Neuroscience* **27**, 13384–13392 (2007).
- [42] Naud, R., Houtman, D., Rose, G. J. & Longtin, A. Counting on dis-inhibition: a circuit motif
   for interval counting and selectivity in the anuran auditory system. *Journal of Neurophysiology* 114, 2804–2815 (2015).
- [43] Barak, O., Sussillo, D., Romo, R., Tsodyks, M. & Abbott, L. From fixed points to chaos: three models of delayed discrimination. *Progress in Neurobiology* **103**, 214–222 (2013).
- <sup>1088</sup> [44] Miller, P. Dynamical systems, attractors, and neural circuits. *F1000Research* 5 (2016).
- <sup>1089</sup> [45] van Alphen, B., Semenza, E. R., Yap, M., van Swinderen, B. & Allada, R. A deep sleep stage in <sup>1090</sup> Drosophila with a functional role in waste clearance. Science Advances 7, eabc2999 (2021).
- [46] Bosco, G. & Poppele, R. Proprioception from a spinocerebellar perspective. *Physiological Reviews* 81, 539–568 (2001).
- <sup>1093</sup> [47] Mamiya, A., Gurung, P. & Tuthill, J. C. Neural coding of leg proprioception in *Drosophila*. <sup>1094</sup> Neuron **100**, 636–650.e6 (2018).
- <sup>1095</sup> [48] Cande, J. *et al.* Optogenetic dissection of descending behavioral control in *Drosophila*. *Elife* **7**, <sup>1096</sup> e34275 (2018).
- [49] Bidaye, S. S. *et al.* Two brain pathways initiate distinct forward walking programs in *Drosophila*.
   *Neuron* 108, 469–485.e8 (2020).
- <sup>1099</sup> [50] Hampel, S., Franconville, R., Simpson, J. H. & Seeds, A. M. A neural command circuit for <sup>1100</sup> grooming movement control. *eLife* **4**, e08758 (2015).
- <sup>1101</sup> [51] Phelps, J. S. *et al.* Reconstruction of motor control circuits in adult *Drosophila* using automated <sup>1102</sup> transmission electron microscopy. *Cell* **184**, 759–774 (2021).
- [52] Marder, E. & Bucher, D. Central pattern generators and the control of rhythmic movements.
   *Current Biology* 11, R986–R996 (2001).
- <sup>1105</sup> [53] Isakov, A. *et al.* Recovery of locomotion after injury in *Drosophila melanogaster* depends on <sup>1106</sup> proprioception. *The Journal of Experimental Biology* **219**, 1760–1771 (2016).
- <sup>1107</sup> [54] Hermans, L. *et al.* Long-term imaging of the ventral nerve cord in behaving adult *Drosophila*. <sup>1108</sup> *bioRxiv* 2021.10.15.463778 (2021).
- <sup>1109</sup> [55] Dubuc, R. & Grillner, S. The role of spinal cord inputs in modulating the activity of reticulospinal <sup>1110</sup> neurons during fictive locomotion in the lamprey. *Brain Research* **483**, 196–200 (1989).
- <sup>1111</sup> [56] Rothwell, J. Ascending and descending pathways of the spinal cord. In *Control of Human* <sup>1112</sup> *Voluntary Movement*, 217–251 (Springer, 1994).
- <sup>1113</sup> [57] Choi, S. *et al.* Parallel ascending spinal pathways for affective touch and pain. *Nature* **587**, <sup>1114</sup> 258–263 (2020).

- [58] Schindelin, J. et al. Fiji: an open-source platform for biological-image analysis. Nature Methods
   9, 676–682 (2012).
- <sup>1117</sup> [59] Mendes, C. S., Bartos, I., Akay, T., Márka, S. & Mann, R. S. Quantification of gait parameters in <sup>1118</sup> freely walking wild type and sensory deprived *Drosophila* melanogaster. *eLife* **2**, e00231 (2013).
- <sup>1119</sup> [60] Ríos, V. L. *et al.* NeuroMechFly a neuromechanical model of adult *Drosophila melanogaster*. <sup>1120</sup> *bioRxiv* 2021.04.17.440214.
- <sup>1121</sup> [61] Berman, G. J., Choi, D. M., Bialek, W. & Shaevitz, J. W. Mapping the stereotyped behaviour <sup>1122</sup> of freely moving fruit flies. *Journal of The Royal Society Interface* **11**, 20140672 (2014).
- <sup>1123</sup> [62] Graving, J. M. behavelet: a wavelet transform for mapping behavior (2019).
- [63] Ke, G. *et al.* LightGBM: a highly efficient gradient boosting decision tree. In Guyon, I. *et al.* (eds.) Advances in Neural Information Processing Systems, vol. 30 (Curran Associates, Inc., 2017).
- <sup>1127</sup> [64] Chawla, N. V., Bowyer, K. W., Hall, L. O. & Kegelmeyer, W. P. SMOTE: Synthetic minority <sup>1128</sup> over-sampling technique. *Journal of Artificial Intelligence Research* **16**, 321–357 (2002).
- <sup>1129</sup> [65] Chen, T.-W. *et al.* Ultrasensitive fluorescent proteins for imaging neuronal activity. *Nature* **499**, <sup>1130</sup> 295–300 (2013).
- <sup>1131</sup> [66] Friedman, J., Hastie, T. & Tibshirani, R. Regularization paths for generalized linear models via <sup>1132</sup> coordinate descent. *Journal of Statistical Software* **33**, 1–22 (2010).
- <sup>1133</sup> [67] Razali, N. M. & Wah, Y. B. Power comparisons of Shapiro-Wilk, Kolmogorov-Smirnov, Lilliefors <sup>1134</sup> and Anderson-Darling tests. *Journal of Statistical Modeling and Analytics* **2**, 21–23 (2011).
- <sup>1135</sup> [68] Jefferis, G. S. *et al.* Comprehensive maps of *Drosophila* higher olfactory centers: spatially <sup>1136</sup> segregated fruit and pheromone representation. *Cell* **128**, 1187–1203 (2007).
- <sup>1137</sup> [69] Bogovic, J. A. *et al.* An unbiased template of the *Drosophila* brain and ventral nerve cord. *PLOS* <sup>1138</sup> *ONE* **15**, e0236495 (2021).
- <sup>1139</sup> [70] Court, R. *et al.* A systematic nomenclature for the *Drosophila* ventral nerve cord. *Neuron* **107**, 1071–1079.e2 (2020).
- [71] Ronneberger, O., P.Fischer & Brox, T. U-Net: convolutional networks for biomedical image segmentation. In *Medical Image Computing and Computer-Assisted Intervention (MICCAI)*, vol. 9351 of *LNCS*, 234–241 (Springer, 2015).
- Payer, C., Štern, D., Neff, T., Bischof, H. & Urschler, M. Instance segmentation and tracking
  with cosine embeddings and recurrent hourglass networks. In Frangi, A. F., Schnabel, J. A.,
  Davatzikos, C., Alberola-López, C. & Fichtinger, G. (eds.) *Medical Image Computing and Com- puter Assisted Intervention MICCAI 2018*, 3-11 (Springer International Publishing, Cham,
  2018).
- <sup>1149</sup> [73] Çiçek, Abdulkadir, A., Lienkamp, S., Brox, T. & Ronneberger, O. 3D U-Net: learning dense <sup>1150</sup> volumetric segmentation from sparse annotation (2016).
- [74] Wang, P., Cuccolo, N. G., Tyagi, R., Hacihaliloglu, I. & Patel, V. M. Automatic real-time CNN based neonatal brain ventricles segmentation. In 2018 IEEE 15th International Symposium on
   Biomedical Imaging (ISBI 2018), 716–719 (2018).
- [75] Ioffe, S. & Szegedy, C. Batch normalization: accelerating deep network training by reducing
  internal covariate shift. vol. 37 of *Proceedings of Machine Learning Research*, 448–456 (PMLR,
  Lille, France, 2015).
- [76] Kingma, D. & Ba, J. Adam: a method for stochastic pptimization. International Conference on Learning Representations (2014).

- <sup>1159</sup> [77] Sørensen, T. J. A method of establishing groups of equal amplitude in plant sociology based on <sup>1160</sup> similarity of species content and its application to analyses of the vegetation on danish commons.
- 1161 Biol. Skar. 5, 1-34 (1948).
- <sup>1162</sup> [78] Dice, L. R. Measures of the amount of ecologic association between species. *Ecology* **26**, 297–302 (1945).
- [79] Buades, A., Coll, B. & Morel, J. M. Denoising image sequences does not require motion estimation. In *IEEE Conference on Advanced Video and Signal Based Surveillance*, 2005., 70–74 (2005).
- <sup>1167</sup> [80] Bradski, G. The OpenCV library. Dr. Dobb's Journal of Software Tools (2000).
- <sup>1168</sup> [81] Otsu, N. A threshold selection method from gray-level histograms. *IEEE Transactions on* <sup>1169</sup> Systems, Man, and Cybernetics **9**, 62–66 (1979).
- [82] Ankerst, M., Breunig, M. M., Kriegel, H.-P. & Sander, J. OPTICS: ordering points to identify
   the clustering structure. In *Proceedings of the 1999 ACM SIGMOD International Conference on Management of Data*, SIGMOD '99, 49–60 (Association for Computing Machinery, New York, NY, USA, 1999).
- [83] Kuhn, H. W. The Hungarian method for the assignment problem. Naval Research Logistics Quarterly 2, 83–97 (1955).
- <sup>1176</sup> [84] van der Walt, S. et al. scikit-image: image processing in Python. PeerJ **2**, e453 (2014).
- [85] Weir, P. T. & Dickinson, M. H. Functional divisions for visual processing in the central brain
   of flying Drosophila. Proceedings of the National Academy of Sciences of the United States of
   America 112, E5523-5532 (2015).
- [86] Guizar-Sicairos, M., Thurman, S. T. & Fienup, J. R. Efficient subpixel image registration
   algorithms. Opt. Lett. 33, 156–158 (2008).
- [87] Guizar, M. Efficient subpixel image registration by cross-correlation (2020).
  (https://www.mathworks.com/matlabcentral/fileexchange/18401-efficient-subpixel-imageregistration-by-cross-correlation), MATLAB Central File Exchange. Retrieved November 9, 2020.